Ultrashort Pulse Generation with a Solid State Cr^{4+}:YAG Laser

by

Hanfei M. Shen

B.S.E., Nuclear Engineering and Radiological Sciences
University of Michigan, 2000

Submitted to the Department of Electrical Engineering and Computer Sciences in partial fulfillment of the requirements for the degree of

Master of Science

at the

MASSACHUSETTS INSTITUTE OF TECHNOLOGY

November 2002

Signature of Author .....
Department of Electrical Engineering and Computer Science
November 8, 2002

Certified by .....
Erich P. Ippen
Elihu Thompson Professor of Electrical Engineering
Professor of Physics

Accepted by .....

Chairman, Department Committee on Graduate Students
Department of Electrical Engineering and Computer Science

Ultrashort Pulse Generation from a Solid State Cr^{4+}:YAG Laser

by

Hanfei M. Shen

Submitted to the Department of Electrical Engineering and Computer Science
on November 8, 2002 in partial fulfillment of the requirements for
the degree of Master of Science

Abstract

A prismless ultrafast Cr^{4+}:YAG laser has been designed and constructed. Intracavity dispersion in this laser is compensated through the use of double-chirped mirrors, in contrast to previous work, which used fused silica prisms. The resonator design for Kerr lens modelocking has been optimized through the use of numerical simulation programs, based on the *ABCD* transfer matrix formalism. Pulses as short as 20 fs were generated directly from the laser. The modelocked spectrum had a FWHM of 190 nm, from 1310 to 1500 nm, with a peak intensity at 1450 nm. Significant spectrum is observable from 1140 nm to >1700 nm. In addition, a novel broadband saturable Bragg reflector was designed and used to self-start modelocking in the Cr^{4+}:YAG laser. The SBR consists of a 7-pair GaAs/Al_xO_y quarter-wave mirror and an InGaAs/InP quantum well saturable absorber. The high-index-contrast of the mirror structure allows for broadband reflection, heretofore unattained, and is able to support ultrashort Cr^{4+}:YAG pulses. Modelocked pulses of 35 fs duration were generated directly from the self-starting laser. The spectrum had a maximum at 1490 nm and a FWHM of 68 nm. Two-photon absorption is believed to be the limiting factor in achieving shorter pulse durations in this laser. With the SBR in the resonator, the Cr^{4+}:YAG laser was also able to generate self-starting picosecond pulses, with center wavelengths tunable from 1400 to 1525 nm.

Thesis Supervisor: Erich P. Ippen
Title: Elihu Thompson Professor of Electrical Engineering, Professor of Physics

ACKNOWLEDGEMENTS

The writing of this thesis took a surprisingly considerable amount of time, some of it due to most unfortunate mishaps, such as the untimely demise of my hard drive, and others due to my own procrastination. Initially, I had a very grandiose outline that planned to cover all aspects of ultrafast lasers, *ad nauseam*. However, as soon as the real work began, I realized just how ridiculous that would have been. Still, I have written a fairly long, and perhaps, tedious review. However, this was certainly more for my own benefit than anything else. In many respects, this SM thesis serves as a collection of my own scattered notes on the subject and will be a useful reminder in the future, hopefully, for my fading memory. To put it succinctly, thesis writing was a lot of work. This was something I really did not appreciate when I first began; it was certainly more than I had bargained for, initially, especially for an SM thesis. But now I'm finished and very happy for it. And grateful that the next thesis is still a few years away. It is certainly a pleasure now to have the opportunity to say a few words of thanks.

First and foremost, I would like to thank my advisor Professor Erich Ippen for giving me the opportunity to work in the one of the world's premier ultrafast laser laboratories. It was only this research group that really sparked an interest in coming to MIT and thank goodness Professor Ippen took me in. Working in his research group has been a privilege and a joy. His patience with me during the writing of this thesis and insightful comments were greatly valued and appreciated. I also thank Professor Franz Kärtner and Professor Hermann Haus for their guidance and clarifying discussions about difficult concepts.

To Dan Ripin, I owe a great debt of gratitude for all that he has taught me about the practical experimental aspects of ultrafast lasers and, of course, the capricious nature of our most wonderful gain medium Cr^{4+}:YAG. Jesting aside, I am very thankful for all his help. His endless patience and determination in the laboratory serve as a role model for all experimenters. Thanks go to Juliet Gopinath for all of her help with the characterization of

the SBR structures described in this thesis. I have enjoyed our colorful discussions in the lab and her friendship. I look forward to finally doing the long-awaited pump probe experiments together.

I thank all the members of the Optics group, past and present, for their acceptance and camaraderie. I single out Poh-Boon Phua and Mike Watts for being great officemates who are engaging as well as entertaining; John Fini for introducing me to New Hampshire state liquor stores, as well as being one of the sharpest people I've ever met; Pat Chou for warmly accepting me into the group and all of his advice; Leaf Jiang for lending me software on numerous occasions; and Sam Wong for all our 'immature' conversations that ripped on 'MIT culture' and the like. And finally, in Thomas Schibli, I believe I have found a kindred spirit, albeit an old one. Sorry, I just can't help but keep jabbing at the poor guy. Professionally, his experimental and theoretical acumen is something all of us should strive for. Personally, he could use some more dance lessons and a perhaps develop a higher tolerance at open bars. I will always look back fondly at our adventures, especially after this latest incident, and our dinners in Chinatown. I will miss his companionship when he leaves in March.

I am grateful for the financial support of a National Defense Science and Engineering Graduate Fellowship.

I am grateful for all the fantastic teachers I've had the luck and benefit of meeting. Mr. Armstrong and Mr. Hanson of Novi High, thank you for all the support and encouragement in those Olympiads. That experience will be something I will always cherish and be proud of. From the University of Michigan, I thank Professor Don Umstadter for introducing me to the world of ultrafast optics – those figure 8 radiation patterns remain to this day the coolest data I've seen; Professor Emmett Leith for his colorful optics lectures and patience in answering my question lists; and Professor Zhong He and Professor Ron Gilgenbach for giving me the opportunity to work in their respective labs.

Well, I'm almost done; at least, no one can accuse me of being curt.

Stephanie Krinksy and Amy Shantz, I thank these two horribly bad influences, from the bottom of my heart, for exposing me to all the distractions and amusements that can be found in the wonderful city of Boston. Without these two, I think I would have lost my sanity my first semester here. Hail to Harvard and Emerson. Of course, after convincing me that I would really not enjoy sunny weather year-round, Steph goes to California herself and abandons me. I'll give both of you a copy of this since you asked for it, but I seriously doubt either of you will get past the Table of Contents. Thanks for trying though. I especially thank Amy since she lent me her laptop when my own computer died. The first draft of Chapter 3

was written on it; ironically, Chapter 3 ended up needing the most revisions... I don't blame you though. However, I do miss my dining buddy.

I thank my parents for all of their support and love. Of all the great teachers I've had, my dad remains the best. You've always had high expectations of me. And I truly resented that when I was younger; but I understand now. I have opportunities you were never afforded. Thank you for giving me these opportunities and making me better.

On a final note, on a lighter note, has anyone noticed the acronym LASER? It stands for Light Amplification by the Stimulated Emission of Radiation. However, in most cases, a laser device is not so much an amplifier but an oscillator. So it should be Light *Oscillation* by the Stimulated Emission of Radiation. But, mercifully, it is not. So, I thank the inventors of said device for giving me the opportunity to work in the field of lasers, not losers.

TABLE OF CONTENTS

LIST OF FIGURES

LIST OF TABLES

Chapter 1

INTRODUCTION

1.1 BACKGROUND

The invention of the ruby laser in the 1960s heralded the beginning of a new and exciting era of science [1]. The basic properties of a laser source – its high degree of monochromaticity, coherence, directionality, and brightness – have led to the wide use of continuous wave (cw) lasers in the fields of spectroscopy, communications, manufacturing, and medicine. Soon after the invention of cw lasers, it was found that a further property of lasers was their ability to generate pulses of extremely short duration. The generation of short pulse duration is important for a variety of applications since the pulse duration ultimately determines the highest temporal resolution at which ultrafast measurements can be made. Mechanical shutters allow for resolution in the millisecond range, and flash photography for the microsecond range. Modern electronic sampling oscilloscopes eventually reach down to the picosecond range. Today, however, ultrafast lasers have set the standard by pushing the limit into the femtosecond regime. The output of a laser can be so well controlled in time, probing of physical process taking place in a few millionths of a billionth of a second has become routine. Research in ultrafast solid state lasers has flourished in the past decade, due to a combination of novel material systems and pulse generation techniques, such as Kerr lens modelocking. In addition, new methods of dispersion compensation and the development of broadband optics have paved the way to record-setting time resolutions in many laser systems. Recently, pulses as short as 5 fs have been generated directly from a Ti:sapphire laser. These pulses are shorter than two optical cycles at their center wavelengths of 840 nm [2]. The evolution of ultrafast lasers has paved the way for promising new applications such as ultrahigh-resolution time domain spectroscopy, optical coherence tomography, and femtochemistry, which won the 1999 Nobel Prize in Chemistry for Zewail [3]. Figure 1 illustrates the rapid advance of ultrashort pulse generation.

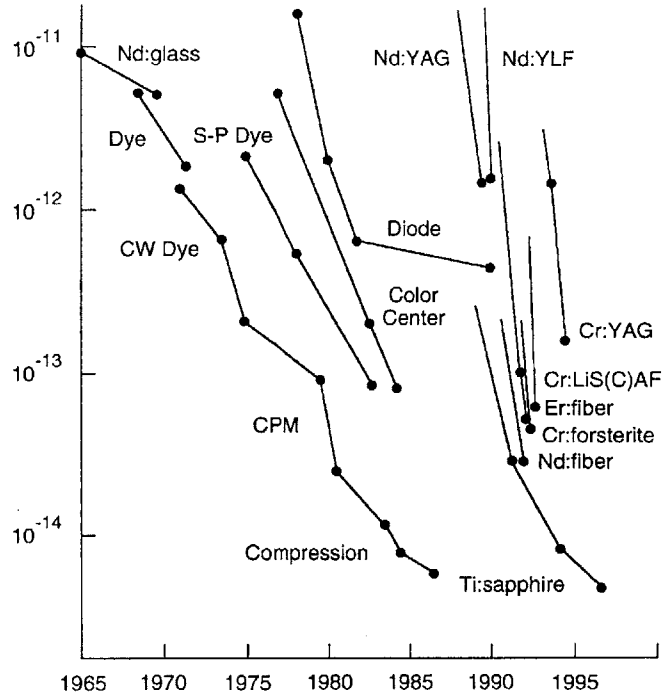

Figure 1.1 Progress in the generation of ultrashort laser pulses. From Ref. [3].

In this thesis, we discuss the development of a solid state Cr^{4+}:YAG laser for ultrashort pulse generation. Cr^{4+}:YAG is chosen as the gain medium because of its broadband emission spectrum and material properties that are favorable for modelocking. The gain bandwidth is in the near-infrared and extends from 1.3 to 1.6 μm. This wavelength range is particularly interesting for optical communication applications since it contains the low-loss wavelength of 1.55 μm. Both the short temporal resolution and the broad spectral bandwidth of Cr^{4+}:YAG pulses can be exploited in applications. For instance, short pulses, because they produce high peak powers with very little energy (average power), can be used to study many nonlinear optical effects, such as optical frequency conversion. Likewise, they facilitate the study of interaction of matter with very intense fields. Perhaps the most classic use of these ultrahigh temporal resolutions is to capture high-speed events, in which case, the laser effectively acts as an ultrafast camera. Using Cr^{4+}:YAG, these applications can be developed in the near-infrared wavelength regime. The broad spectrum of ultrashort Cr^{4+}:YAG pulses can also provide many simultaneous wavelength channels for optical communication systems using multi-channel wavelength division multiplexing (WDM) [5]. In addition, there are

many other potential applications, such as optical metrology and medical imaging.

1.2 THESIS OUTLINE

This thesis presents the development of few-cycle pulse generation from a solid state Cr^{4+}:YAG laser.

In Chapter 2, we examine some of the fundamental principles of ultrafast lasers. The effects of dispersion and self-phase modulation are discussed as pulse-shaping mechanisms, and autocorrelation is reviewed as a pulse measurement technique. In addition, we also talk about the material properties of Cr^{4+}:YAG.

In Chapter 3, we review the techniques of modelocking. We begin with a general perspective on what modelocking is and how it works. Then we proceed to examine the two different regimes of operation – active modelocking and passive modelocking. We briefly discuss soliton modelocking. Finally, we look at two specific examples of saturable absorber mechanisms – one real, a saturable Bragg reflector, and one artificial, Kerr lens modelocking.

The laser resonator design and experimental results are presented in Chapter 4. We review three important aspects of the Cr^{4+}:YAG laser resonator design – dispersion compensation, astigmatism compensation, and removal of water impurities. Then, we present the results of a prismless Kerr lens modelocked Cr^{4+}:YAG laser. This laser, however, does not self-start modelocking. As a solution, we introduce a novel broadband saturable Bragg reflector into the cavity. We discuss the properties of this structure and present its results as well.

And finally, in Chapter 5, we summarize our experimental findings and propose future directions in the development and application of the Cr^{4+}:YAG laser source.

Chapter 2

FUNDAMENTALS OF ULTRAFAST LASERS

In this chapter, we discuss some of the important basic principles of ultrafast lasers. We first consider the material properties that make Cr^{4+}:YAG a favorable gain medium. Then we look at the various effects that an optical pulse experiences during propagation through the laser resonator. One of these effects – dispersion – plays a critical role in ultrashort pulse generation, and methods of compensating intracavity dispersion are presented. Finally, autocorrelation is reviewed as a technique for measuring ultrashort pulse durations.

2.1 MATERIAL PROPERTIES OF Cr^{4+}:YAG

In the past decade, the rapid development of tunable solid state laser materials has revolutionized the field of ultrafast optics. Combined with novel ultrashort pulse generation techniques, solid state lasers have supplanted dye lasers as the source of the shortest optical pulses ever produced. The Ti:sapphire laser, a common solid state laser and a workhorse in ultrafast optics, has been shown to generate pulses as short as 5 fs, with a correspondingly broad spectrum from 580 to 1160 nm [2]. Like dye lasers, solid state lasers offer tunable output wavelength and the broad bandwidth needed to generate ultrashort pulses. Lasers using solid state gain media have other significant advantages including chemical and mechanical stability and robustness, long upper state lifetimes allowing for considerable energy storage and high intensity damage thresholds. Furthermore, the nonlinearity of the solid state gain crystal can be exploited for passive Kerr lens modelocking, discussed in the next chapter.

Tunable solid state lasers, such as Ti:sapphire and Cr^{4+}:YAG, belong to a family of materials that operate on vibronic transitions in which the active ions change both the vibrational states of the host crystal and the electronic states. The active ions in these lasers are transition metals whose valence electrons occupy the radially-extended *d*-orbitals. When

incorporated into a host, the outer-lying electrons of these ions are exposed to local potentials strongly coupling them with the phonons of the host. The vibrational sublevels spread some electronic energy levels into bands, so transitions can take place over a range of energies. This coupling causes considerable inhomogeneous broadening of both absorption and emission transitions [6]. In contrast, rare earth ions have valence electrons that reside in lower radius orbitals, where they are effectively shielded from vibrations of the lattice by the filled, larger-radii orbitals. Therefore, the result of doping with transition metal ions is positive gain at a broad range of wavelengths in these vibronic lasers. A broad gain bandwidth makes possible the broad spectral bandwidths of ultrashort light pulses in such laser systems. For the purposes of modelocking and the generation of ultrashort pulses, these phonon-broadened solid state gain media are quite attractive.

In the Cr^{4+}:YAG laser crystal, a chromium ion is added to the cubic garnet YAG ($Y_3Al_5O_{12}$) host as a substitutional impurity, replacing an aluminum ion. The incorporation of chromium into a solid state host has historical significance as a Cr-doped sapphire, or ruby (Cr^{3+}:Al_2O_3), was used by Maiman as the gain medium of the first optical laser [1]. The Cr ion has since been used as the active emission center in several crystalline hosts including alexandrite, emerald, Cr:LiCAF, and Cr:LiSAF, where the Cr ion is trivalent and emission tends to be in the near-infrared (<1000 nm) [7,8,9,10]. A second class of Cr-based lasers, of which Cr^{4+}:YAG is one and where the Cr ion is tetravalent, operates in the 1000 to 1600 nm wavelength range. This spectral range is particularly interesting for telecommunication applications since it includes the lowest-loss wavelength of 1.55 μm in optical fiber. Both color-center lasers and Er-doped glass lasers have been used to generate short pulses in this wavelength region. However, both of these laser systems have severe disadvantages to the Cr^{4+}:YAG. Color-center lasers must be kept under vacuum and chilled to liquid nitrogen temperatures during operation; and Er-doped glass has a limited gain bandwidth. In contrast, Cr^{4+}:YAG can be operated at room temperature in air, is easily cooled with flowing water, and has a substantially larger gain bandwidth than Er-doped glass. Finally, Cr^{4+}:YAG has broad absorption bands at 0.48 μm, 0.64 μm, and 1.0 μm. The latter band spans from 0.85 μm to 1.2 μm, making the system ideal for pumping with commercially-available Nd:YAG and Nd:YVO_4 lasers operating at 1.06 μm. Table 2.1 at the end of this section summarizes thee material properties of Cr^{4+}:YAG.

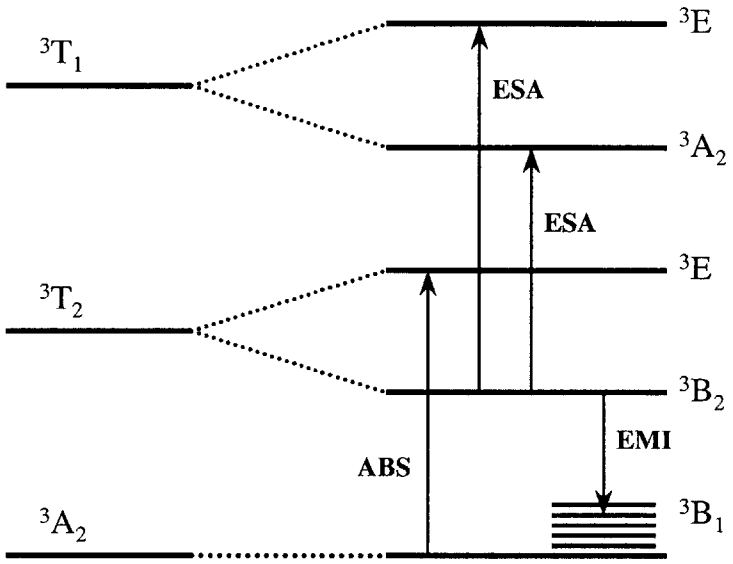

Figure 2.1 Schematic of the active electronic energy levels in a Cr^{4+}:YAG material system. Pump light is absorbed through the transition ABS, and laser light is emitted in the transition EMI. Excited state absorption transitions ESA reduce the overall gain of the laser by siphoning light from both the ABS and EMI transitions.

Figure 2.1 shows the electronic energy level diagram of a tetrahedrally-coordinated Cr^{4+} ion with a $3d^2$ electron configuration. Spectroscopic studies have shown it is indeed the tetravalent chromium ions that are responsible for emission [11,12,13,14,15]. The vibrationally-broadened emission transition is between the $^3B_2$ and $^3B_1$ states. A sample photoluminescence spectrum measured from the 2 cm Cr^{4+}:YAG crystal used in our experiments is shown in Figure 2.2. The crystal exhibits broadband emission from 1220 to 1650 nm, with a maximum at 1365 nm. The transition from the $^3A_2$ state to the ^3E state corresponds to pump absorption around 1060 nm. Additional transitions from the $^3B_2$ state to the $^3T_1$ state correspond to excited state absorption (ESA) transitions. The presence of ESA absorption at 1060 nm from $^3T_2$ ($^3B_2$) to $^3T_1$ (^3E) significantly degrades the pumping efficiency of the upper lasing transition level. ESA within the laser emission band from $^3T_2$ ($^3B_2$) to $^3T_1$ ($^3A_2$) reduces the effective stimulated emission cross section of Cr^{4+}:YAG and increases the lasing threshold.

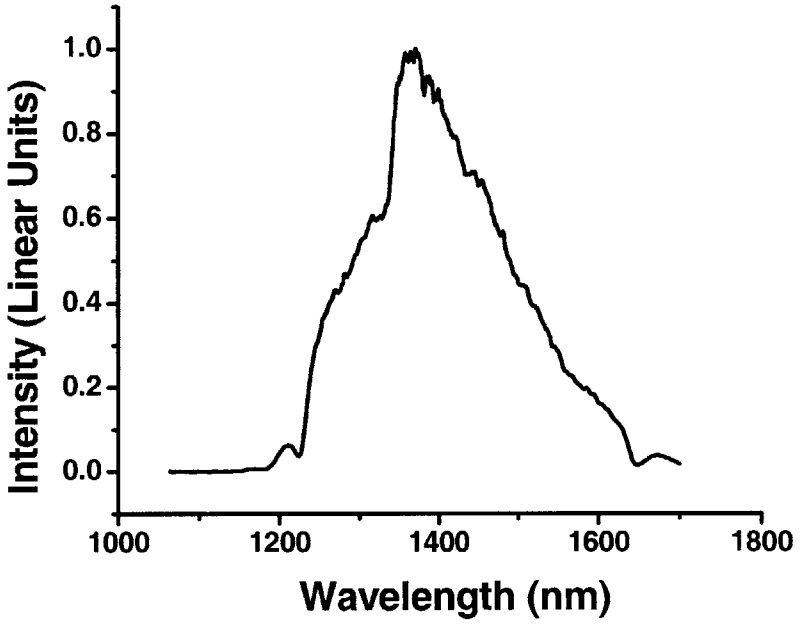

Figure 2.2 Measured photoluminescence of the 2 cm Cr^{4+}:YAG laser crystal used in this work [16].

Despite its many attractive properties, there are several disadvantages to using Cr^{4+}:YAG in a modelocked laser system. Excited state absorption depletes both the pump and laser light, effectively reducing the overall gain of Cr^{4+}:YAG. As a result, the net gain of Cr^{4+}:YAG is less than that of many other ultrafast laser gain media. This requires a relatively longer crystal length to provide the necessary gain in this laser system, hence posing the problem of additional material dispersion to compensate. Other unfavorable properties include a large thermo-optic coefficient and low thermal conductivity, which together create significant thermal lensing effects in the laser cavity. Thermal lensing changes the laser resonator mode and is difficult to model. Finally, the Cr^{4+}:YAG gain spectrum is plagued by several resonant water absorption lines. Water vapor in the air causes abrupt variations in the cavity dispersion, thereby inhibiting modelocking. In addition, these absorption lines introduce costly intracavity loss.

On a final note, it is worth mentioning that the fluorescence lifetime of the Cr^{4+} ion decreases as the overall chromium dopant concentration (Cr^{3+} and Cr^{4+} ions) increases [17]. This implies that ion-ion interaction becomes important with high dopant concentration.

Lower fluorescence lifetimes inhibit population inversion, which in turn prevent lasing. Due to this concentration quenching effect, the performance of a short and highly-doped crystal is restricted; and, in order to obtain moderate powers necessary for modelocking, a laser crystal with low dopant concentration must be relatively long, prohibiting the development of a compact Cr^{4+}:YAG microchip laser system.

Parameter	Value
Gain Bandwidth	1200 - 1600 nm
Absorption Bandwidth	850 - 1200 nm
Effective Gain Cross-Section	3×10^{-19} cm^2
Effective Absorption Cross-Section	3×10^{-18} cm^2
Saturation Intensity of Pump at 1064 nm	1.7×10^4 W/cm^2
Index of Refraction n	1.81
Nonlinear Index of Refraction n_2	6.9×10^{-16}cm^2/W
Upper-State Lifetime at 300 K	3.6 μs
Thermal Conductivity	0.12 W/K cm

Table 2.1 Material properties of Cr^{4+}:YAG. Adapted from Ref. [11-15].

2.2 Optical Pulse Propagation

Femtosecond laser realization relies on the precise control and optimization of a variety of effects. Dispersion, in particular group velocity dispersion (GVD), and self-phase modulation (SPM) are two of the most important. The balancing and interplay of GVD and SPM play a crucial role in ultrafast lasers. In this section, we discuss GVD and SPM, as well as a third effect encountered in an ultrafast laser cavity – gain dispersion.

2.2.1 Group Velocity Dispersion

Dispersion is a critical pulse shaping mechanism in ultrafast lasers. Dispersion can be introduced via pulse propagation through media with a frequency-dependent index of refraction $n(\omega)$ or with geometric constructions, such as prism pairs, which we will explain in

more detail later. In such a medium, the phase velocity for different frequencies of light is

$$v_{phase} = \frac{c}{n(\omega)} \tag{2.1}$$

However, we are interested in the behavior of a pulse of light, or a wave packet. Except in vacuum, the phase and the envelope of a wave packet usually travel with different speeds; and it is the speed of the envelope, or the group velocity, with which we are concerned. Any pulse can be interpreted as a superposition of narrowband wave packets that travel at different group velocities. By positioning dispersive materials in the beam path, the resulting time delay in the arrival of different spectral components leads to temporal pulse broadening. This effect is termed group velocity dispersion, or GVD.

Now we consider this problem analytically. After propagation through a medium of length L, the temporal field of a wave packet can be written as

$$E(z = L, t) = \int E(0, \omega)\exp[i(\omega t - \varphi(L, \omega))]d\omega \tag{2.2}$$

where $E(z = 0, \omega)$ is Fourier transform of the initial field entering the medium

$$E(z = 0, \omega) = \frac{1}{2\pi}\int E(0, t)\exp(-i\omega t)dt \tag{2.3}$$

and φ is the phase shift.

$$\varphi(L, \omega) = \frac{\omega n(\omega)}{c}L \tag{2.4}$$

The temporal intensity profile of the pulse is related to the square modulus of the field.

$$I \sim |E(L, t)|^2 \tag{2.5}$$

For a signal with a narrow spectrum centered about the carrier frequency ω_c, upon passing through a dispersive medium, the Taylor expansion about ω_c of the frequency-dependent phase shift gives

$$\varphi(\omega) = \varphi(\omega_c) + \left.\frac{d\varphi}{d\omega}\right|_{\omega_c}(\omega - \omega_c) + \frac{1}{2}\frac{d^2\varphi}{d\omega^2}(\omega - \omega_c)^2 + \frac{1}{6}\frac{d^3\varphi}{d\omega^3}(\omega - \omega_c)^3 + \ldots \tag{2.6}$$

Substituting this into Equation (2.2), we get

$$E(L,t) \sim \exp i(\omega_c t - \varphi_c) \int E(0, \omega' + \omega_c) \exp i\left[\omega'(t - T_g) - \frac{1}{2}\omega'^2 GDD - \frac{1}{6}\omega'^3 TOD\right] d\omega' \quad (2.7)$$

Here, we have used the dummy variable $\omega' = \omega - \omega_c$. The variables T_g, GDD, and TOD are discussed below.

The first term in Equation (2.6) is only the constant phase shift experienced by the carrier frequency ω_c. The coefficient of the second term in Equation (2.6) is the group delay T_g, which is the time required for a pulse to pass through an optical element of length L.

$$T_g(\omega_c) = \left.\frac{d\varphi}{d\omega}\right|_{\omega_c} = \frac{L}{v_g} \quad (2.8)$$

Here, v_g is the group velocity. From Equation (2.7), one can easily see that the exponential pre-factor represents the rapidly-varying carrier wave propagating at the phase velocity v_p, while the integral describes the slowly-varying pulse envelope which propagates at the group velocity v_g. Without dispersion, that is if GDD and TOD vanishes, the intensity envelope $|E|^2$ does not change after propagation, except for a time shift of T_g. One can observe this simply by comparing Equation (2.7) with Equation (2.2).

The coefficient of the third term in Equation (2.6), generally in units of fs^2, is the group delay dispersion (GDD).

$$GDD(\omega_c) = \left.\frac{d^2\varphi}{d\omega^2}\right|_{\omega_c} = L\frac{d}{d\omega}\left(\frac{1}{v_g}\right) \quad (2.9)$$

The group velocity dispersion (GVD), in units of fs^2/mm, is related to the GDD by

$$GVD(\omega_c) = \frac{GDD(\omega_c)}{L} = \frac{d}{d\omega}\left(\frac{1}{v_g}\right) \quad (2.10)$$

Dispersion is determined by the variation of the group velocity v_g with frequency ω. In the normal dispersion regime, where GVD is positive, longer wavelengths, or red components, travel faster than shorter wavelengths, or blue components. While in the anomalous dispersion regime, where GVD is negative, blue spectral components travel faster than red components. Upon passing through a dispersive medium, pulses become "chirped". The terms down-chirped, up-chirped, and unchirped (transform-limited) are used for a pulse whose instantaneous frequency decreases, increases, or remains constant with time, respectively. The effect of dispersion is such that a transform-limited input pulse will become

temporally dispersed during propagation and will become up-chirped or down-chirped, depending on the medium. In a normal dispersion material, an initially unchirped pulse develops an up-chirp, since red components arrive in the leading edge of the pulse and blue components in the trailing edge; hence the instantaneous frequency increases with time. Conversely, traveling through a medium with anomalous dispersion creates a down-chirp. An initially unchirped pulse is always broadened after traveling through a dispersive medium, but initially chirped pulses may be compressed or broadened depending on the relative signs of the dispersion and the pulse chirp. This effect will be discussed more in the self-phase modulation section later. For the simple case of pure GDD, the FWHM duration τ_p of an initially unchirped Gaussian pulse, after traversing a dispersive medium, is

$$\tau_p = \tau_0\left[1 + \left(4\ln 2 \frac{|GDD|}{\tau_0^2}\right)^2\right]^{1/2} \tag{2.11}$$

where τ_0 is the initial pulse duration [18].

Going back to Equation (2.6), the coefficient of the fourth term gives the third-order dispersion, or TOD, in units of fs^3.

$$TOD(\omega_c) = \left.\frac{d^3\varphi}{d\omega^3}\right|_{\omega_c} \tag{2.12}$$

Generally, the effect of TOD and additional higher-order terms can be neglected and GDD (second-order dispersion) is the only term we need to consider. However, for pulses of extremely short duration and correspondingly broad bandwidths, TOD becomes significant and imposes a limit on the minimum achievable pulse width.

2.2.2 Material Dispersion

Material or chromatic dispersion within dielectric media is a result of the interaction between an electromagnetic wave and the bound electrons of said medium. The medium response, in general, depends on the optical wavelength λ. Hence, material dispersion manifests itself through the wavelength dependence of the index of refraction $n(\lambda)$. On a fundamental level, the origin of material dispersion is related to the characteristic resonant frequencies at which the dielectric medium absorbs electromagnetic radiation through oscillations of its bound electrons. The Lorentz model treats the interaction between light and matter by considering the motion of electrons in a material to be a classical harmonic oscillator with forcing and damping terms. The electrons are forced by the oscillating electric field of the light and

damped by electron-lattice interactions. From this model, one can derive the Sellmeier equation, which approximates the index of refraction far from medium resonances.

$$n(\lambda) = \sqrt{1 + \sum_j \frac{A_j \lambda^2}{\lambda^2 - \lambda_j^2}} \tag{2.13}$$

Here, λ_j is the resonant wavelength and A_j is the strength of the j-th resonance. For Cr^{4+}:YAG, the Sellmeier equation yields

$$n(\lambda) = \sqrt{1 + \frac{2.293\lambda^2}{\lambda^2 - (0.1095)^2} + \frac{3.705\lambda^2}{\lambda^2 - (17.825)^2}} \tag{2.14}$$

where λ is in units of μm. From the wavelength dependence of the index of refraction, the group velocity dispersion of Cr^{4+}:YAG can be calculated from

$$GVD(\lambda) = \frac{\lambda^3}{2\pi c^2} \frac{d^2}{d\lambda^2} n(\lambda) \tag{2.15}$$

The index of refraction $n(\lambda)$ and the GVD of Cr^{4+}:YAG are plotted in Figure 2.3.

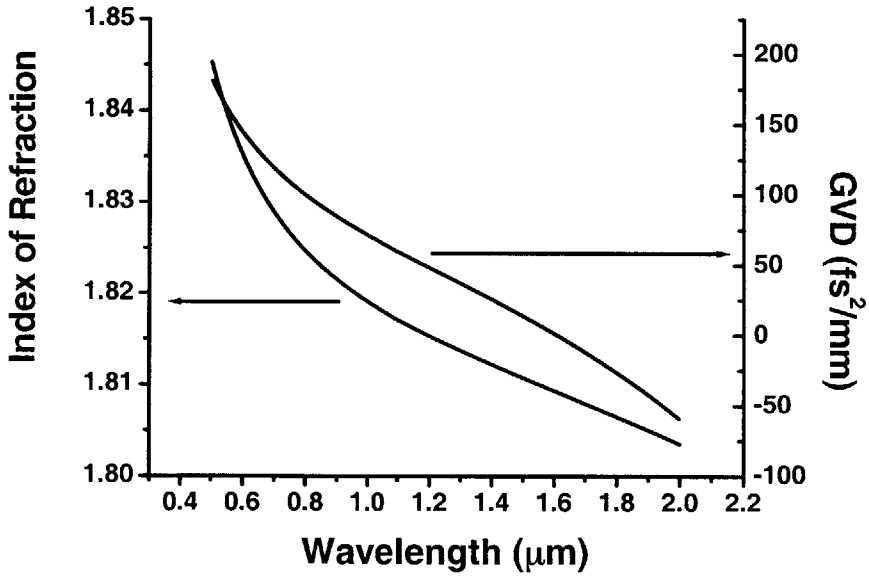

Figure 2.3 Index of refraction and group velocity dispersion for YAG material.

2.2.3 *Gain Dispersion*

Another form of dispersion is so-called gain dispersion, or gain filtering. All other parameters held constant, lasers with broadband gain can support shorter pulses than lasers with narrowband gain. Gain dispersion is a fundamental concept arising from the line shapes of atomic transitions involved in laser action [19]. Line shapes account for the fact that atomic energy levels involved in laser action are not infinitely sharp but rather have finite bandwidths arising from a variety of physical phenomena. The exact mathematical formulation of the line shape is dependent on the specific broadening processes involved. Gain media are classified into those that are homogeneously broadened and those that are inhomogeneously broadened.

Homogeneous broadening occurs when every atom involved in laser action possesses the same atomic line shape and frequency response. Consequently, every atom in the laser gain medium is indistinguishable and responds identically to an applied electric field. The resulting Lorentzian frequency dependence of the line shape is

$$g(\omega) \sim \frac{1}{(\omega - \omega_c)^2 + \Omega_h^2} \tag{2.16}$$

where ω_c is the center frequency and Ω_h is the homogeneous line width of the transition. Effects leading to homogeneous broadening include dephasing collisions between radiating atoms or molecules with other atoms or molecules, collisions with phonons, and spontaneous radiative transitions to other levels.

Inhomogeneous broadening arises when the atoms are distinguishable, and the broadening reflects a spread in the individual resonant transition energies of the atoms. As a result, the individual responses to applied signals cannot be treated identically. This kind of broadening gives a Gaussian line shape.

$$g(\omega) \sim \exp\left[-\frac{(\omega - \omega_c)^2}{\Omega_i^2}\right] \tag{2.17}$$

where Ω_i is the inhomogeneous line width, which is larger than the homogeneous line width Ω_h. Two main examples of this type of broadening are those of strain broadening caused by impurity ions in a host crystal and of Doppler broadening in gas lasers.

In either case, the gain can be approximated near the center of the line shape by replacing it with an inverted parabola. In this parabolic approximation, the frequency-dependent gain is

$$g(\omega) = g\left[1 - \frac{(\omega - \omega_c)^2}{\Omega_g^2}\right] \tag{2.18}$$

where g is the maximum gain, ω_c is the center frequency, and Ω_g describes the gain bandwidth. Using the properties of the Fourier transform, we can write Equation (2.18) in the time domain as

$$g(t) = g\left(1 + \frac{1}{\Omega_g^2}\frac{d^2}{dt^2}\right) \tag{2.19}$$

Gain dispersion effectively acts as a bandwidth-limiting spectral filter that tends to broaden pulses during amplification. Indeed, as will be discussed shortly, it is an important parameter in determining the ultimate pulse duration achievable in a modelocked laser.

2.2.4 Self-Phase Modulation

The nonlinear Kerr effect gives rise to self-phase modulation, as well as the fast saturable absorber modelocking mechanism discussed in the next chapter. The Kerr effect arises from the nonlinear polarization induced in media under the influence of a strong electric field. In general, the polarization in a medium can be expressed as [20]:

$$P = \varepsilon_0(\chi_1 E + \chi_2 E^2 + \chi_3 E^3 + \ldots) \tag{2.20}$$

where χ_2 and χ_3 are the second- and third-order optical susceptibilities, respectively. For simplicity, the fields P and E have been written as scalar quantities in Equation (2.20). In general, however, these are vector quantities, and χ_1 becomes a second-rank tensor, χ_2 becomes a third-rank tensor, etc. Second-order nonlinear optical interactions can occur only in non-centrosymmetric crystals, that is, in crystals that do not display inversion symmetry. Since liquids, gases, amorphous solids and even many crystals do display inversion symmetry, χ_2 vanishes for such media, and consequently they cannot produce second-order nonlinear optical interactions. On the other hand, the third-order nonlinear optical susceptibility χ_3 exists in both centrosymmetric and non-centrosymmetric media. It is χ_3 that is the origin of the Kerr effect. If we include the χ_3 term, the electric displacement D is given by

$$D = \varepsilon_0 E + P = \varepsilon_0(1 + \chi_1 + \chi_3 E^2)E \tag{2.21}$$

Since $D = \varepsilon E$, the complete nonlinear dielectric constant is

$$\varepsilon = \varepsilon_0(1 + \chi_1 + \chi_3 E^2) \tag{2.22}$$

Consequently, the index of refraction $n = (\varepsilon/\varepsilon_0)^{1/2}$ is given by

$$n = n_0 + n_2 I \tag{2.23}$$

where n_0 and n_2 are defined as

$$n_0 = \sqrt{1 + \chi_1} \tag{2.24}$$

$$n_2 = \frac{\chi_3 \eta}{n_0} \tag{2.25}$$

where η is the impedance of the material.

The Kerr effect becomes important in modelocked lasers at intensities where the change in optical length brought about by the nonlinear refractive index n_2 becomes comparable to a wavelength. Using typical values for the Cr^{4+}:YAG gain medium – $n_2 = 6.9 \times 10^{-16}$ cm^2/W, λ = 1450 nm, L = 2 cm, this translates to intensities on the order of 100 GW/cm^2. Peak intensities in typical femtosecond lasers usually reach several tens of GW/cm^2 and are therefore sufficient to render Kerr nonlinearities significant.

Self-phase modulation (SPM) is a spectral and temporal nonlinear effect originating from the Kerr nonlinearity. As discussed previously, a medium with a Kerr effect displays an intensity-dependent index of refraction. After propagating a distance L in such medium, a pulse initially defined by

$$E(z, t) = A(t)e^{j(\omega_0 t - kz)} \tag{2.26}$$

acquires a time-varying phase shift $\varphi(t)$ which can be expressed as

$$\varphi(t) = -\frac{2\pi}{\lambda} L[n_0 + n_2 I(t)] \tag{2.27}$$

where λ is the wavelength in free space. The time rate of change of phase, or the frequency shift as a function of time, termed chirp, is

$$\delta\omega = \frac{d}{dt}\varphi(t) = -\frac{2\pi}{\lambda} L n_2 \frac{dI}{dt} \tag{2.28}$$

Therefore, we see that the chirp, which is the variation in instantaneous frequency across the

pulse, is a function of intensity. Since n_2 is positive, the leading edge of the pulse, where $dI/dt > 0$, will experience a down-shift in frequency (red shift) and the trailing edge of the pulse, where $dI/dt < 0$, will experience an up-shift in frequency (blue shift). Since the frequency then varies from low to high with time, the pulse is up-chirped. Figure 2.4 illustrates this schematically. The initial temporal electric field is shown in the top panel. Note that time increases from right to left in this figure, as its sign is opposite that of the propagation length z. After traversing a Kerr medium, the field acquires a frequency chirp $\delta\omega(t)$, as shown in the center panel. The leading edge of the pulse is up-chirped and the trailing edge down-chirped. The effect of this chirp on the temporal electric field is shown in the last panel.

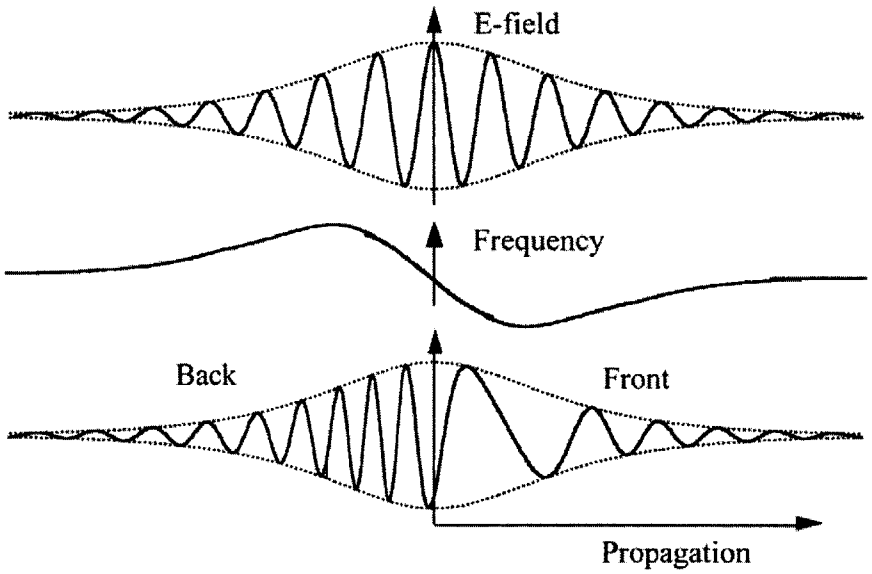

Figure 2.4 Broadening due to self-phase modulation. The initial electric field, shown in the top panel, acquires a frequency chirp, shown in the middle panel, after propagation through a nonlinear medium. The last panel demonstrates the effect of chirp on the temporal electric field.

Let us consider the effect of SPM on an initially unchirped Gaussian pulse analytically [19]. The electric field and the intensity, respectively, are

$$E(t) = A_0 e^{-at^2} e^{j\omega_0 t} \tag{2.29}$$

$$I(t) = I_0 e^{-2at^2} \tag{2.30}$$

Assuming, for simplicity, that the pulse shape remains constant after propagation through a length L, the instantaneous frequency ω_i across the pulse is given by

$$\omega_i(t) = \omega_0 + \delta\omega \tag{2.31}$$
$$= \omega_0 - \frac{2\pi}{\lambda} L n_2 \frac{dI}{dt}$$
$$= \omega_0 + \frac{8\pi a n_2 L I_0}{\lambda} t e^{-2at^2}$$

$$\omega_i(t) \sim \omega_0 + \frac{8\pi a n_2 L I_0}{\lambda} t \tag{2.32}$$

Consequently, to first order, SPM adds a linear frequency chirp (up chirp) across the central region of the pulse.

SPM can be considered a spectral-broadening mechanism. From Equation (2.28), the frequency chirp introduced by SPM increases in magnitude with propagated distance *L*. In other words, as the pulse propagates through a Kerr medium, SPM generates new frequency components, which are red-shifted near the leading edge and blue-shifted near the trailing edge. These SPM-generated frequency components broaden the spectrum over its initial width. This, in turn, affects the evolution of the pulse shape, and hence the pulse duration. Keep in mind that the finite gain bandwidth of the laser crystal provides a limit to the potential spectral width of an ultrashort pulse; however, SPM can significantly increase that limit due to its spectral broadening effects.

In the absence of GVD, SPM alone does not alter the temporal pulse profile, as only a phase factor is added. Under most practical conditions, however, GVD is present and the pulse duration is affected as a result. Consider first a pulse propagating in the normal (positive) dispersion regime of a Kerr medium. Frequency components in the leading edge of the pulse, which are already red in comparison to those in the trailing edge, are red-shifted even more by SPM; and the blue frequency components of the trailing edge are blue-shifted even more. Since the red components travel faster than the blue components in the normal dispersion regime, SPM leads to an enhanced rate of pulse broadening compared with that expected from GVD alone.

The situation is different for pulses propagating in the anomalous, or negative, dispersion regime. Here, the blue frequency components in the leading edge of the pulse are red-shifted, and the red frequency components of the trailing edge are blue-shifted. The leading edge slows down and the trailing edge speeds up, resulting in pulse compression. Note that the SPM-induced chirp is positive, while the dispersion-induced chirp is negative in the anomalous dispersion regime. When both SPM and GVD act on a pulse simultaneously, the two chirp contributions nearly cancel each other in the pulse. The pulse shape adjusts itself

during propagation to make this cancellation as complete as possible. As SPM changes the spectrum of the pulse by creating new frequencies at various locations within the pulse, GVD simultaneously repositions those new frequencies back to the proper part of the pulse. Thus, GVD and SPM cooperate with each other to maintain a chirp-free pulse. Under such conditions, the pulse can propagate over long distances without changing its shape. This unchanged propagating pulse is called an optical soliton. Based on the same mechanism, by compensating SPM with negative GVD, intracavity pulse compression can be achieved in a bulk laser as a result of soliton-like pulse shaping (although SPM and GVD do not entirely act on the pulse simultaneously). The application of this phenomenon to modelocking will be discussed more in the next chapter.

2.3 DISPERSION COMPENSATION

Dispersion compensation plays a critical role in generating ultrashort pulses. Because these pulses have broad frequency spectra, the varying propagation speed for the different spectral components causes the pulse to change its shape during propagation. Therefore, in an ultrafast laser, the net intracavity dispersion imposes a limit on the minimum pulse duration achievable. The highest peak intensity and the largest curvature of the intensity envelope will be reached in an experiment only if all spectral components arrive at the same time. In most ultrafast lasers, the dispersion is mainly a result of the intracavity dielectric media. A method of compensating this intracavity dispersion such that it is minimized is therefore necessary.

For most solid state lasers, the group velocity dispersion of the gain medium host is normally positive over its operating wavelength range. Also the intracavity pulse is always up-chirped after passing through the tightly focused gain medium, due to self-phase modulation. For these reasons, the addition of negative GVD such that the intracavity dispersion is slightly negative is often required. The importance of the slightly negative overall dispersion will become more apparent in the modelocking chapter. In addition, after compensating for GVD, higher-order dispersion, such as TOD, must be kept to a minimum.

2.3.1 Insertion of Anomalous Dispersion Material

There are several methods that can introduce negative dispersion into the cavity. The simplest would be to insert a Brewster-cut optical glass material with negative dispersion into the laser cavity. However, this is only applicable for lasers operating at wavelength longer than 1.3 μm. This is because most glass materials have dispersion that is positive in the visible spectrum and changes its sign only in the near-infrared. For instance, the Cr^{4+}:YAG laser

could use a piece of fused silica for intracavity dispersion compensation. Cr^{4+}:YAG has a GVD of 11 fs^2/mm at 1500 nm, while fused silica has a GVD of -32 fs^2/mm at 1500 nm. In order to compensate the normal dispersion from 4 cm of Cr^{4+}:YAG at 1500 nm, an insertion of 14 mm of fused silica is required. A plot of the overall GDD for combinations of Cr^{4+}:YAG and five different thicknesses of fused silica prism material is shown in Figure 2.5 .

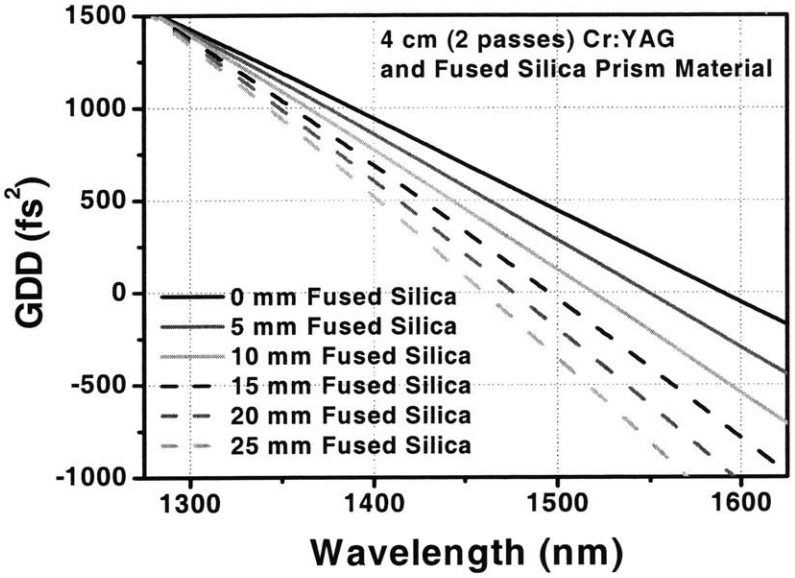

Figure 2.5 Group delay dispersion of Cr^{4+}:YAG and fused silica glass of different thicknesses [16].

However, from this plot, it is evident that third-order dispersion remains when GDD is compensated. Recall that TOD is the derivative of the GDD with respect to frequency.

2.3.2 Prisms

The most commonly used technique to supply intracavity negative dispersion employs a pair of Brewster-cut prisms [21]. The schematic of a common prism pair configuration is illustrated in Figure 2.6. Typically, the prism pair is placed in one arm of the laser cavity before an end mirror (M). Hence, over the course of a roundtrip in the laser cavity, the pulse effectively passes through a four-prism sequence. The action of the first two prisms is repeated in the second pair. The geometric dispersion of a prism pair is based on angular dispersion. Take note that a prism pair also provides material dispersion, as described previously, be it normal or anomalous, in addition to geometric dispersion. The two prisms are placed in series. The first element in the pair (I) diffracts each wavelength at a different

angle, providing the GVD. The second element (II), which is parallel to the first, recollimates the spatially dispersed spectral components and gives rise to a wavelength-dependent optical path delay.

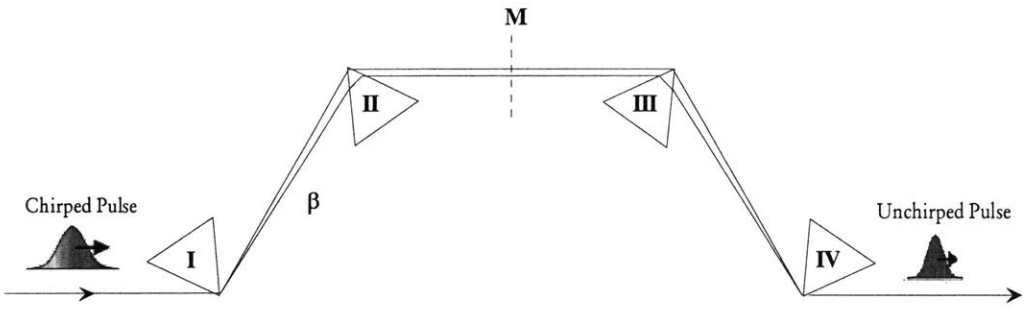

Figure 2.6 Four-prism sequence used for dispersion compensation.

Each prism is designed with a Brewster-cut apex angle, such that the incident pulse enters and exits the medium at Brewster's angle. The apex angle is

$$\theta_{apex} = 2\theta_B' = 2\arctan\left(\frac{1}{n}\right) \tag{2.33}$$

where θ_B' is Brewster's angle inside the prism and n is the index of refraction of the prism material. Because the prisms are designed so, the insertion loss of the prism pair is minimized. The geometric dispersion of a prism pair is always anomalous. The group delay dispersion of the prism sequence shown in Figure 2.6 is

$$GDD(\lambda_c) = \frac{\lambda_c^3}{2\pi c^3}\frac{d^2P}{d\lambda^2} \tag{2.34}$$
$$= \frac{\lambda_c^3}{2\pi c^3} 4L\left\{\left[\frac{d^2n}{d\lambda^2} + \left(2n - \frac{1}{n^3}\right)\left(\frac{dn}{d\lambda}\right)^2\right]\sin\beta - 2\left(\frac{dn}{d\lambda}\right)^2\cos\beta\right\}$$

where c is the speed of light, P is the optical path length, L is the apex-to-apex prism separation, and β is the angular deviation of the dispersed pulse. The entire expression is evaluated at the carrier wavelength λ_c. By properly adjusting the prism spacing, the correct amount of dispersion can be provided. In this manner, prism pairs make variable dispersion compensation possible.

In addition to anomalous GDD, prism pairs also generate third-order dispersion. TOD

becomes important when the intracavity GDD is minimized. The TOD of a four-prism sequence is

$$TOD(\lambda_c) = -\frac{\lambda_c^4}{4\pi^2 c^3}\left(3\frac{d^2P}{d\lambda^2} + \lambda\frac{d^3P}{d\lambda^3}\right) \tag{2.35}$$

$$= -\frac{\lambda_c^4}{4\pi^2 c^3} 4L\left(\frac{d^3n}{d\lambda^3}\sin\beta - 6\frac{dn}{d\lambda}\frac{d^2n}{d\lambda^2}\cos\beta\right)$$

This TOD, however, is not a welcome artifact. In an optimized ultrafast laser, both the GDD and TOD need to be simultaneously compensated. Consequently, TOD is a significant disadvantage to using prism pairs.

Another disadvantage to prism pairs is their inherent water content. The water impurities in many glasses commonly used for prisms give rise to costly intracavity insertion loss, as well as disruptive spikes in the intracavity dispersion. Strong water absorption lines in the spectral range of 1300 to 1500 nm coincide with the Cr^{4+}:YAG gain profile. This effect will be discussed in more detail when we consider the experimental cavity configuration in Chapter 4. Some bulk materials with low water content are commercially available. Among these are crystalline materials, such as CaF_2 and BaF_2, which naturally exclude water impurities from their regular lattice structures. The GVDs of a few such materials are plotted in Figure 2.7.

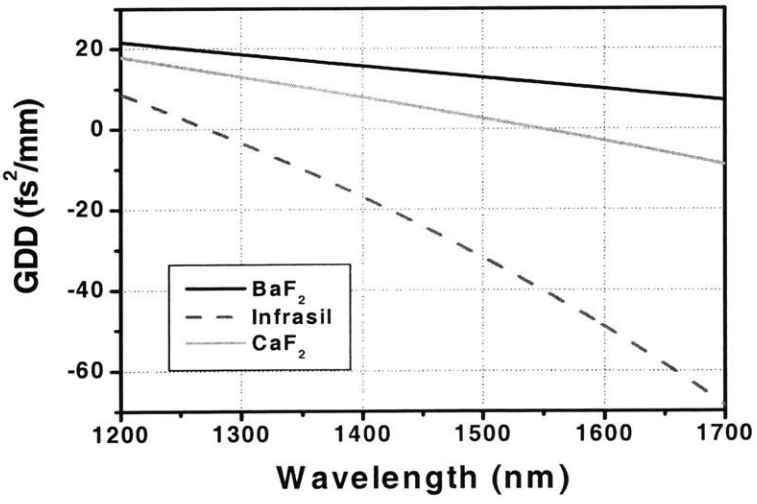

Figure 2.7 Group delay dispersion of bulk prism materials with low water content [16].

2.3.3 *Chirped Mirrors*

A relatively novel technique for intracavity dispersion compensation is the use of chirped mirrors. Chirped mirrors are custom-tailored multilayer coatings, off which the incident light is reflected with a wavelength-dependent group delay.

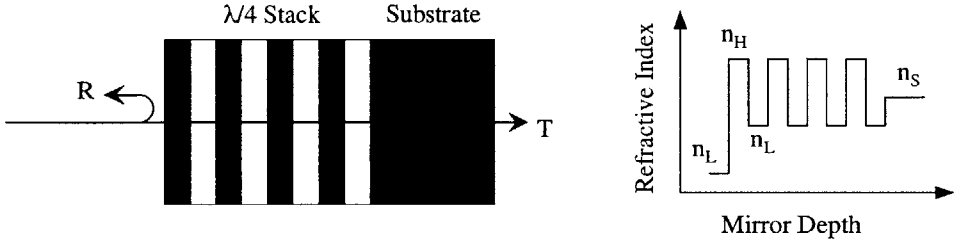

Figure 2.8 Schematic of a quarter-wave Bragg mirror.

Standard high-reflectance Bragg mirrors consist of quarter-wave stacks, as shown in Figure 2.8. The bandwidth of these mirrors increases with the index contrast of the dielectric materials and the number of layers (up to a certain point). However, phase properties in such mirrors, pertaining to dispersion compensation, are not a design criterion; hence regions of extreme phase variations can be present, and their use in femtosecond lasers is limited.

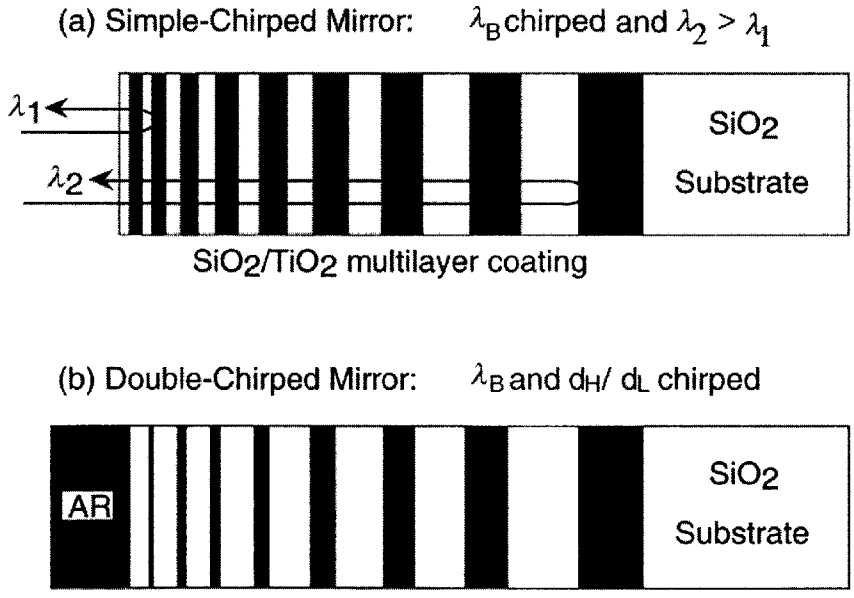

Figure 2.9 Schematic comparison of a simple-chirped and double-chirped mirror. In (a), the Bragg wavelength gradually increases with depth into the mirror. In (b), the duty cycle of the low-index SiO_2 layer is additionally increased, in conjunction with the Bragg wavelength.

The invention of the "chirped mirror" by Szipocs et al. started a new era in ultrashort pulse generation [22]. A schematic of the simple-chirped mirror is shown in Figure 2.9 (a). The high- and low-index materials are typically TiO_2 and SiO_2. Absorption is almost negligible for these ion-beam-sputtered structures, which is one advantage over prisms with water impurities. In simple-chirped mirrors, the periodicity of the quarter-wave stack, and hence the Bragg wavelength, is gradually decreased during deposition. As a result, each wavelength of a pulse travels a different optical path length in the mirror, with longer wavelengths penetrating deeper into the structure. This gives rise to anomalous dispersion, since longer wavelengths have a greater group delay T_g than shorter ones. In addition, the high-reflectance range of the mirror is broadened in comparison to standard Bragg mirrors. The reflectance R and the group delay T_g of a sample simple-chirped mirror are plotted as functions of wavenumber and wavelength in Figure 2.10.

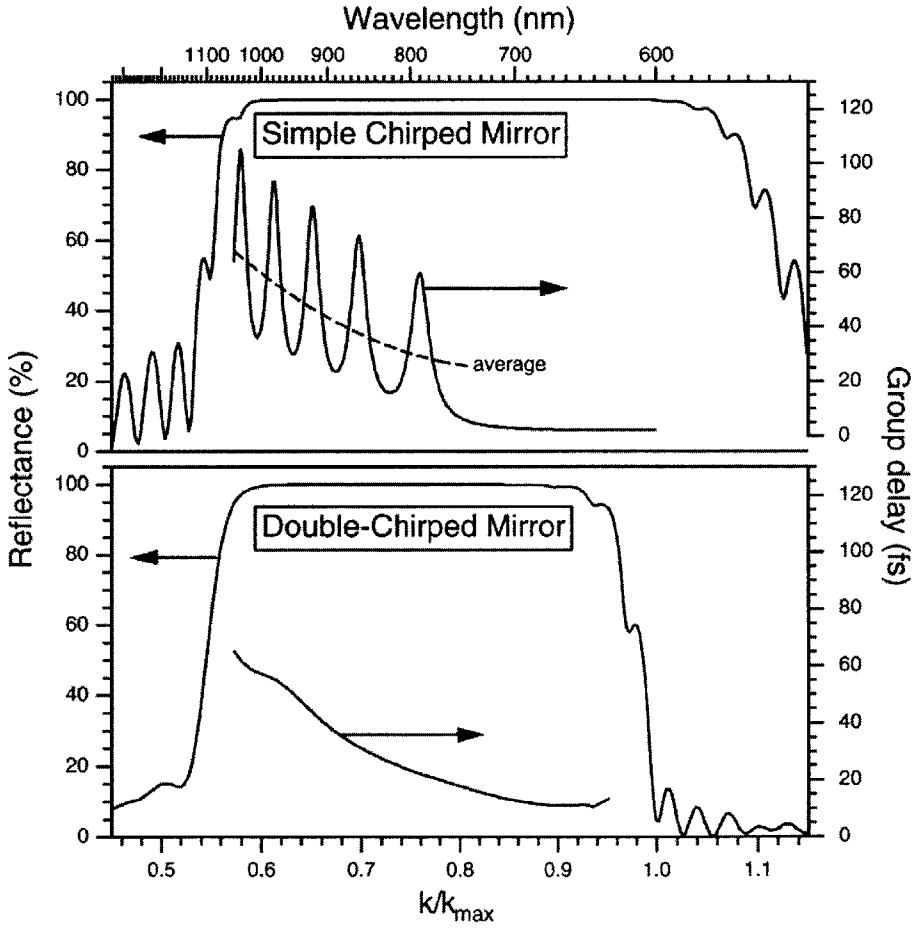

Figure 2.10 Comparison of the reflectance and group delay properties of simple-chirped and double-chirped mirrors [23].

Note that GDD is the derivative of T_g with respect to frequency. Therefore, the GDD is negative, as it was intended; and its magnitude increases with wavelength. However, strong spectral oscillations in the dispersion can be seen in Figure 2.10. These dramatic shifts can distort a modelocked pulse, thus limiting the use of such mirrors in ultrashort pulse generation. The oscillations arise from imperfect anti-reflection off the front surface of the chirped mirror. Long wavelengths that penetrate deep into the mirror are also weakly reflected on their way through the front sections of the mirror. The interference of these two components is what creates the observed spectral oscillations.

Using the concept of impedance matching, double-chirped mirrors (DCMs) were designed to reduce the detrimental effects of residual reflection off the front surface of the mirror [23]. In contrast to simple-chirped mirrors, DCMs have an additional gradual increase in the duty cycle of the low-index SiO_2 layers. Both the Bragg wavelength λ_B and the duty cycle are chirped in these mirrors, hence the name double-chirped. Here, the duty cycle refers to the portion of the low-index material that contributes to the Bragg wavelength. According to the coupled mode theory presented in Ref. [23], the backward and forward propagating modes in the mirror structures shown in Figure 2.9 are connected via a coupling coefficient κ, which, in turn, is a function of the duty cycle. It was found that a sufficiently slow increase in the coupling coefficient in the front section of the mirror could phase-match the forward and backward propagating modes at each mirror interface [24]. Therefore, by chirping both the Bragg wavelength and the coupling coefficient, via the duty cycle, DCMs greatly reduce the large spectral oscillations in the group delay dispersion seen in simple-chirped mirrors. Hence, double-chirped mirrors effectively combine a broadband anti-reflection coating with the broadband reflection and anomalous dispersion control of simple-chirped mirrors. Plots of the reflectance and group delay of a sample double-chirped mirror are shown in Figure 2.10, in addition to those of a simple-chirped mirror. There are two characteristics one should take notice of in the plot. First, and most important, we see that the impedance matching suppresses the undesired spectral oscillations, therefore GDD is smooth, as well as negative. Using DCMs, the intracavity group delay dispersion is compensated and relatively flat over a large spectral range, and consequently, the third-order dispersion is also compensated. In this manner, DCMs better prisms by allowing precise control of second- as well as third-order dispersion, essential for short pulse generation. In addition, DCMs have less insertion loss than prisms. Second, we notice from the plot that the bandwidth of the high-reflectivity region of the double-chirped mirror is less than that of the simple-chirped mirror. Of course, this is expected, due to the reduced coupling coefficient at the beginning of the DCM structure, from which shorter wavelengths reflect. Hence, as seen in the plot, bandwidth is reduced only on the low-wavelength side of the high-reflectivity range. Therefore, a smooth GDD comes at the expense of some bandwidth.

2.4 AUTOCORRELATION MEASUREMENT

The precise characterization of few cycle pulses is a challenging subject on its own and its development has paralleled the progress in ultrashort pulse generation. The advent of femtosecond lasers brought a new problem of measurement. The direct combination of a photodiode and an oscilloscope were no longer adequate to temporally resolve the ultrashort pulses generated. The fastest optical detectors have response times on the order of picoseconds; and, hence, they are unable to measure pulses of femtosecond duration. The duration of femtosecond pulses is so short that only self-referencing techniques can be used to measure them. That is, the only thing fast enough to measure the pulse is the pulse itself. One such technique is autocorrelation.

The relatively high peak powers of ultrafast lasers make nonlinear correlation techniques suitable for pulse duration measurements. Instead of measuring the pulse shape directly, nonlinear optical techniques measure the correlation function of its temporal intensity profile. In general, for an autocorrelation measurement, two identical replicas of a pulse are generated. These replicas are then delayed with respect to each other, and then recombined, via some nonlinear optical effect, to form a product whose magnitude depends on their overlap. The overlap of the two intensity envelopes is mapped as a function of time delay by spatial variation of the optical path difference between the replicas. In this way, the difficult task of measuring time scales on the order of femtoseconds is converted into the much easier task of measuring lengths on the order of microns. For instance, 100 fs has an equivalent optical path length of 30 μm.

2.4.1 SHG Autocorrelator

Due to its relative simplicity and good temporal resolution, the most common form of autocorrelation is by second harmonic generation (SHG). Nanojoule pulse energies make it impractical to use higher-order nonlinearities, due to bandwidth limitations. The basic scheme of an autocorrelator is a Michelson interferometer. The schematic of a typical second harmonic generation autocorrelator is shown below in Figure 2.11.

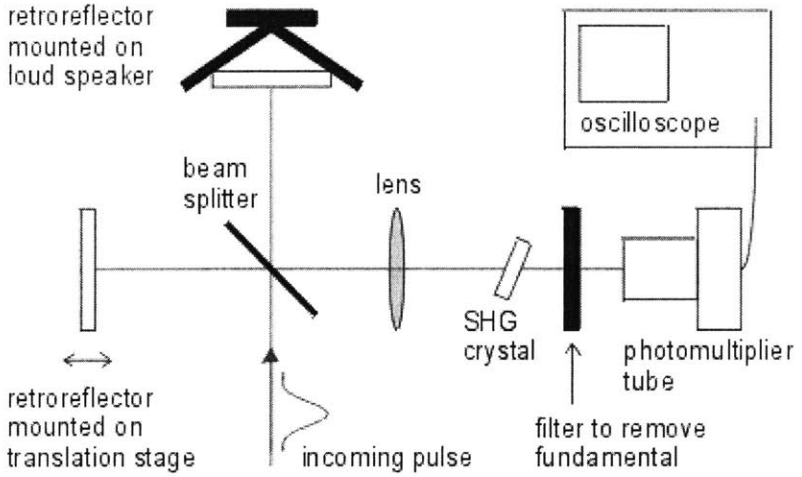

Figure 2.11 Schematic of an autocorrelator based on second harmonic generation.

The input pulse from a modelocked laser is equally split by a 50:50 beam splitter. After passing through a fixed and variable delay line, the replicas are then spatially and temporally overlapped in an SHG crystal.

In order to align the interferometer, the length of each arm must first be adjusted to be equal, in order to find zero delay. Then, the variable delay line is constructed by mounting one of the mirrors on an audio loud speaker. Real-time monitoring of the autocorrelation function is made possible by scanning the loud speaker at 1 kHz. As the speaker moves in and out, the path length of one arm of the interferometer changes, so a delay is introduced between the pulses upon arrival at the SHG crystal. When the path lengths for the two pulses are equal, the pulses will exactly coincide at the crystal and the amount of second harmonic light generated will be a maximum. As the speaker changes the delay, the second harmonic signal will decrease. Because the speaker frequency is much less than the pulse repetition rate, the autocorrelation trace is generated by the second harmonic signal produced from many pulses, each subject to a different time delay τ.

Now that a physical picture of the measurement has been established, we develop an analytical expression for the SHG signal. Pulses in one arm of the interferometer have a temporal delay τ relative to the other arm. Hence, upon arrival at the nonlinear crystal, the electric field envelope can be written as

$$A(t,\tau) = A_1(t) + A_1(t+\tau)e^{-i\omega\tau} \tag{2.36}$$

where A_1 is the envelope of the fundamental harmonic field. The factor $exp(-i\omega\tau)$ accounts for the phase difference between the two pulses produced by the variable delay τ. After the nonlinear interaction in the SHG crystal, the electric field envelope becomes

$$A_2(t,\tau) = cA(t,\tau)^2 \tag{2.37}$$

where c is an arbitrary constant that factors out later in the calculation and A_2 is the second harmonic field. The intensity of this second harmonic signal is

$$I_2(t,\tau) = \frac{1}{2}\frac{n}{\eta_0}\left|A_2(t,\tau)\right|^2 \tag{2.38}$$

where n is the index of refraction and $\eta_0 = (\mu_0/\varepsilon_0)^{1/2}$ is the free space impedance.

The photomultiplier tube detects the second harmonic light generated in the nonlinear crystal and the resultant electrical signal is integrated over a period that is long compared to the pulse duration. Therefore, the signal becomes

$$\begin{aligned}\int_{-\infty}^{\infty} I_2(t,\tau)dt = \frac{1}{2}\frac{n}{\eta}C^2\Big\{&\Big[\int_{-\infty}^{\infty}\left(\left|A_1(t)\right|^4 + \left|A_1(t+\tau)\right|^4 + 4\left|A_1(t)\right|^2\left|A_1(t+\tau)\right|^2\right)dt\Big] + \ldots \\ &4\cos\omega\tau\Big[\int_{-\infty}^{\infty}\left(A_1(t)^3A_1(t+\tau) + A_1(t)A_1(t+\tau)^3\right)dt\Big] + \ldots \\ &2\cos 2\omega\tau\Big[\int_{-\infty}^{\infty}A_1(t)^2A_1(t+\tau)^2dt\Big]\Big\}\end{aligned} \tag{2.39}$$

The average power of the second harmonic light of the recombined beam is then recorded as a function of delay. The autocorrelation produced has a background level due to the signals from each arm, and a peak corresponding to the second harmonic generation when the pulses perfectly overlap. The ratio of the peak to the background is well defined for a modelocked pulse; hence, the autocorrelation can be used to adjust the laser system for optimum performance. The second-order correlation function $g_2(\tau)$ is Equation (2.39) normalized to its background level of $2\int I_1^2(t)dt$.

$$g_2(\tau) = \frac{\int_{-\infty}^{\infty} I_2(t,\tau)dt}{2\int_{-\infty}^{\infty} I_1(t)dt} \tag{2.40}$$

In the equation above, we have assumed a symmetric splitting by the beam splitter so that $A_1(t) = A_1(t + \tau)$. The more familiar form of $g_2(\tau)$, often found in the literature, is

$$g_2(\tau) = 1 + \frac{[2\int_{-\infty}^{\infty} E_1(t)^3 E_1(t+\tau)dt + 2\int_{-\infty}^{\infty} E_1(t)E_1(t+\tau)^3 dt + 3\int_{-\infty}^{\infty} E_1(t)^2 E_1(t+\tau)^2 dt]}{\int_{-\infty}^{\infty} E_1(t)^4 dt} \quad (2.41)$$

Here, the full electric field $E(t)$ is used instead of the field envelope $A(t)$. The full electric field $E(t)$ incorporates the envelope function $A(t)$, the rapidly-varying carrier frequency component and the phase delay $exp(-i\omega\tau)$. By substituting Equation (2.36) with $E = E_1(t) + E_1(t + \tau)$, one can readily arrive at Equation (2.41). The reason for developing Equation (2.40), however, will become apparent soon.

There are two types of autocorrelation – intensity and interferometric autocorrelations, sometimes called slow and fast, respectively.

The function $g_2(\tau)$, from either Equation (2.40) or (2.41), measures the interferometric, or fringe-resolved, autocorrelation. In contrast to intensity autocorrelations, interferometric autocorrelations contain knowledge about the variation of phase with time, or chirp, within the pulse. The first two integrals in Equation (2.41) carry this phase information and give rise to the interference fringes in the autocorrelation. The dependence of the interferometric autocorrelation on pulse parameters, such as chirp, is discussed in more detail in other sources [25,26]. At zero delay ($\tau = 0$), the pulses from each arm have perfect overlap in the nonlinear crystal and constructively interfere. This generates the peak SHG signal. At the next delay of a half wavelength, the SHG signal is a minimum as a result of destructive interference. As the delay increases, the envelopes formed by the constructive maxima and destructive minima gradually merge into the background level. From Equation (2.41), one can readily see a peak-to-background contrast ratio $g_2(0)$ / $g_2(\infty)$ of 8:1. An example of an interferometric autocorrelation is shown in Figure 2.12.

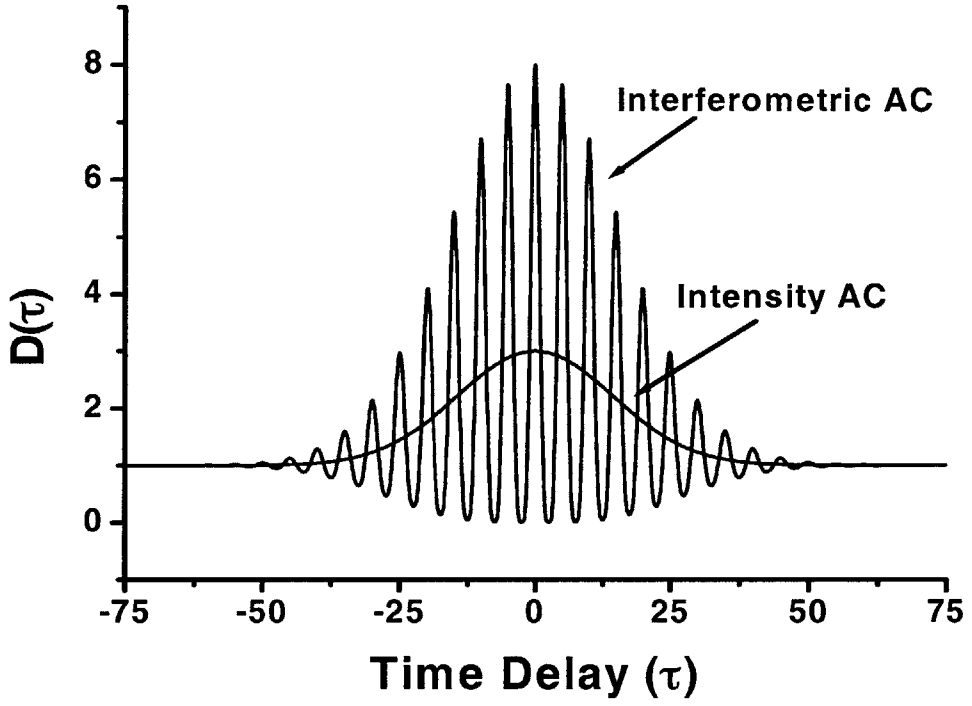

Figure 2.12 Calculated interferometric and intensity autocorrelation functions for a 20 fs Gaussian pulse at 1500 nm.

If the response of the SHG signal detection system is slow compared to the rate of variation of the optical delay, the interference fringes in the autocorrelation trace cannot be resolved. In this case, an intensity autocorrelation is measured and the fringes are averaged over. The reason for this is because the detector takes a single data point over a range of time delays, instead of a single distinct τ value, as is the case for an interferometric autocorrelation. Due to this 'smearing' effect, the SHG signal is averaged over the time delay τ. Referring to Equation (2.40), the two cosinusoidal terms vanish as a result of this averaging, leaving

$$G_2(\tau) = 1 + \frac{2\int_{-\infty}^{\infty} A_1(t)^2 A_1(t+\tau)^2 dt}{\int_{-\infty}^{\infty} A_1(t)^4 dt} \tag{2.42}$$

$$= 1 + \frac{2\int_{-\infty}^{\infty} E_1(t)^2 E_1(t+\tau)^2 dt}{\int_{-\infty}^{\infty} E_1(t)^4 dt}$$

$G_2(\tau)$ is the intensity autocorrelation function. This result is much less apparent from Equation (2.41), hence the motivation for developing Equation (2.40). It can readily be seen that the intensity autocorrelation has a peak-to-background contrast ratio $g_2(0) / g_2(\infty)$ of 3:1. As mentioned earlier, this contrast ratio can be used as a quality check of the laser modelocking. However, it has been shown that this ratio is close to 3:1 even when only 30% of the modes are phase-locked, therefore caution must be exercised in regarding this ratio too seriously [27]. An example of an intensity autocorrelation is also shown in Figure 2.12. One can see from the figure that the intensity autocorrelation is a time average of the interferometric autocorrelation.

For the purpose of measuring few cycle pulses, an interferometric autocorrelation is preferred because of its ability to detect chirp and the possibility of using the interference fringes to calibrate the abscissa. For an autocorrelator interchangeable between intensity and interferometric operation, the latter mode can be achieved by reducing the scan rate of the retroreflector mounted on the audio loud speaker.

The first step in measuring the pulse duration is to calibrate the oscilloscope trace to display the autocorrelation in terms of time. One method is by moving the translation mirror in one arm of the interferometer a set amount and noting how far across the screen the autocorrelation has shifted. This gives the calibration in terms of distance per screen division. Dividing by the speed of light converts the calibration to time per screen division. A second method to calibrate the x-axis is to use the interference fringes produced by a HeNe laser that is directed through the interferometer. The distance between fringe maxima correspond to a time delay given by

$$\Delta\tau = \frac{\lambda_{HeNe}}{c} \tag{2.43}$$

where λ_{HeNe} = 632.8 nm and c is the speed of light. Once the time delay for each fringe is determined, the oscilloscope's internal abscissa can be calibrated to units of time. After calibration by either method, the time width of the autocorrelation can be measured directly from the trace.

The full-width half-maximum of an autocorrelation trace, τ_{ac}, is related to that of the original pulses, τ_p, by a constant κ, such that

$$\tau_p = \frac{\tau_{ac}}{\kappa} \tag{2.44}$$

The deconvolution factor κ depends on the initial pulse shape as well as the type of

autocorrelation. For example, pulses with a sech profile, commonly seen in passively modelocked lasers, have values of $\kappa = 1.897$ for interferometric autocorrelations and $\kappa = 1.543$ for intensity autocorrelations. Deconvolution factors for many common pulse shapes can be found in Ref. [28].

An additional advantage of interferometric autocorrelations is the ability to directly discern the pulse duration from the number of fringes in the autocorrelation trace. For an autocorrelation with good fringe visibility, the spacing between two successive fringe maxima corresponds to one optical period (at the carrier frequency) of the laser pulse. Therefore, the number of fringes counted on one side of the interferometric autocorrelation is directly related to the total optical period of the pulse. Note that an autocorrelation is symmetric about its center. This technique assumes that the pulses are transform-limited, due to the reliance on the carrier frequency to estimate pulse duration.

2.4.2 Photodiode-based Autocorrelator

Recently, it has been shown that an LED-based measurement system can provide a much simpler and more compact method of autocorrelating femtosecond pulses [29]. The nonlinear power-dependent response from an unbiased photodiode can be used to detect and characterize modelocked femtosecond pulses as part of an autocorrelator. Pulses as short as 6 fs were measured from a Ti:sapphire laser with a GaAsP photodiode [30]. The analytical expressions for the autocorrelation functions developed in the previous section are exactly the same for a photodiode-based autocorrelator. The only difference between the two autocorrelators is the mechanism by which the nonlinear response is generated. The use of a photodiode completely replaces the nonlinear crystal and photomultiplier tube needed for a second harmonic generation autocorrelator. A typical photodiode-based autocorrelator is shown in Figure 2.13.

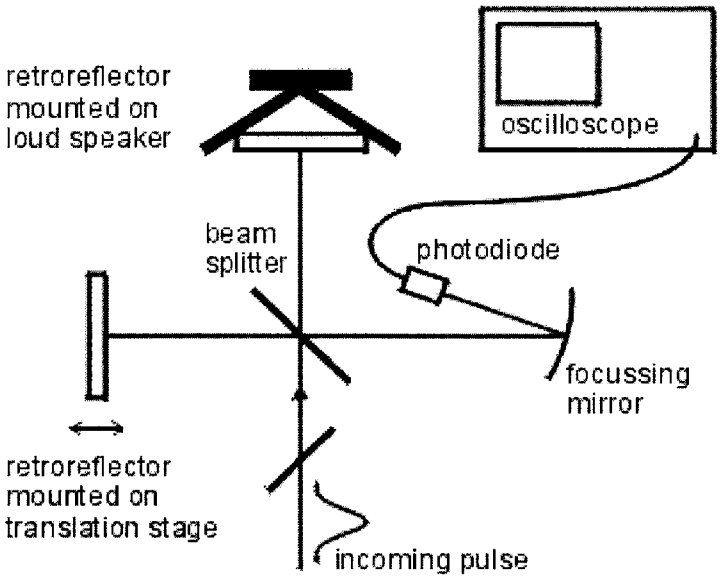

Figure 2.13 Schematic of a photodiode-based autocorrelator.

The mechanism for the nonlinear effect in photodiodes is two-photon absorption (TPA). Two-photon absorption works to convert the optical signal at the fundamental wavelength directly into a photocurrent. This process is a non-resonant nonlinear effect only seen at high intensities. An electron in the valence band of a semiconductor absorbs two photons, which give it enough energy for promotion to the conduction band. Hence, the photons must have a minimum energy of half the band gap, so that two photons could move an electron from the top of the valence band to the lowest level of the conduction band. Concurrently, the band gap must be sufficiently large to prevent direct absorption of the fundamental photons. Thus, the frequency requirement of the photodiode is

$$\frac{\omega_g}{2} \leq \omega_l \leq \omega_g \tag{2.45}$$

where ω_g is the band gap frequency of the photodiode and ω_l is any frequency within the spectrum of the fundamental laser pulse. The band gap is roughly equivalent to the peak emission wavelength of the diode. As an example, for Ti:sapphire pulses at 800 nm, an AlGaAs LED would be used since it has a peak emission at 660 nm. Having this band gap qualifies AlGaAs LEDs for use in correlating pulses from 660 nm to 1320 nm. For the Cr^{4+}:YAG laser, Si photodiodes and GaAs LEDs are particularly well-suited for measuring pulses at 1500 nm [31].

There are numerous advantages to using an LED or photodiode in an autocorrelator. For one, LEDs are cheap compared to the cost of a nonlinear crystal and photomultiplier tube. They are readily available and very robust and compact. The broad wavelength response makes the device applicable to many pulse sources, and the lack of phase matching means that tuning is not required for different sources. Thus, the alignment is far simpler. Finally, the small volume of material that the light must travel through minimizes dispersive pulse broadening, especially if the light is focused onto the diode with a curved metallic mirror instead of a lens.

Chapter 3

MODELOCKING

In this chapter, we discuss the theory of modelocking. We first consider the general mechanism of modelocking, continuing on to compare the two distinct types of modelocking – active and passive. It will be shown that passive modelocking is more effective in ultrashort pulse generation than active modelocking. We then discuss passive modelocking in its two limits – slow saturable absorber modelocking and fast saturable absorber modelocking. We follow that with a brief discussion about soliton modelocking. And finally, we finish with two examples of saturable absorber mechanisms, one real – a saturable Bragg reflector, and one artificial – Kerr lens modelocking.

3.1 GENERAL MODELOCKING PRINCIPLES

Over the past four decades, scientists have developed various techniques for generating pulsed laser light. These techniques include Q-switching, modelocking, and cavity-dumping [19]. In all of these cases, some kind of modulation mechanism is introduced into the laser resonator. For Q-switched pulses, the modulation rate is low compared to the cavity roundtrip time, and the results are long but powerful pulses. In contrast, for modelocking, the modulation period is synchronous with the cavity roundtrip time, and a train of pulses is emitted. Modelocking produces much shorter pulses than Q-switching.

Because of the uncertainty principle relating the time and frequency domains, the ultimate temporal resolution of a laser pulse is limited by its spectral bandwidth. Therefore, in an attempt to produce a pulse that is short in time, we must supply it with the broadest possible frequency spectrum. This is where the broadband gain of Cr^{4+}:YAG becomes advantageous. In contrast to normal cw lasers, an ultrafast laser simultaneously lases in many different modes, thereby producing a short pulse in the time domain whose duration is inversely proportional to the number of propagating modes. The photons in any given mode will certainly be in phase with each other as a result of stimulated emission. However, the

relationship between the phases of the radiation in different cavity modes will generally be uncorrelated. This produces random fluctuations in the intensity over time. Modelocking describes the set of techniques that are used to generate a known correlation between the phases and thereby make it possible to predict when the intensity maxima will occur. An illustration of modelocking is given in Figure 3.1.

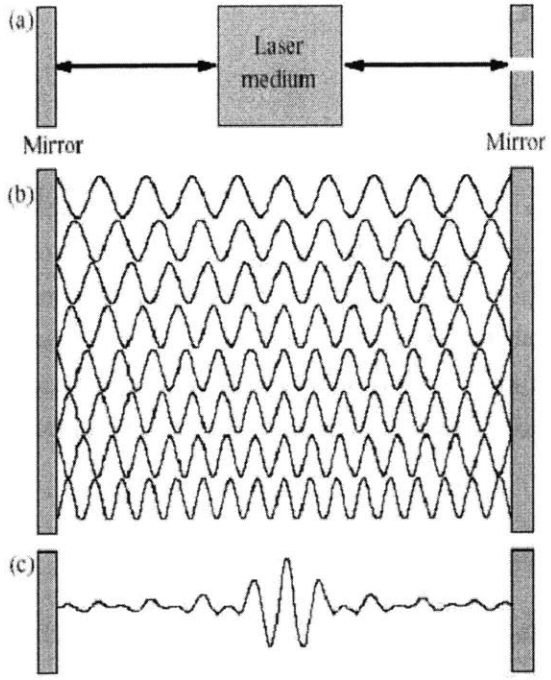

Figure 3.1 Principle of modelocked laser operation [32]. (a) A laser gain medium is positioned between two mirrors, one of them partly transmissive. (b) Different laser modes exist in a cavity under the condition that an integer number of half-periods of the wavelength equals the cavity length. (c) Constructive superposition of different modes at one point creates a high-intensity burst.

Let us examine resonant laser modes and modelocking in more detail. We first look at the result of modelocking and then investigate its mechanism.

A very fundamental concept in the context of modelocking is the existence of discrete axial, or longitudinal, laser frequencies in the optical resonator. A resonant mode is defined by the self-consistency requirement that a field distribution reproduce itself after one complete roundtrip inside the cavity. Therefore, different laser modes exist in a cavity under the condition that an integer number of wavelengths equal the cavity roundtrip length

$$n\lambda = 2L \tag{3.1}$$

where L is the length of the laser resonator; therefore $2L$ is the roundtrip transit. Therefore, any steady-state output of a laser consists of an (incoherent) superposition of modes separated by

$$\Delta f = \frac{c}{2L} \tag{3.2}$$

where c is the speed of light. Note that there should be an extra factor of the refractive index $n(\omega)$ in the denominator. This accounts for the dispersion where different wavelengths see different cavity lengths. In the following discussion, however, for simplicity of argument, we assume that dispersion is compensated and this factor can be neglected.

The spectral window where the frequency-dependent gain exceeds the intracavity loss limits the actual number of such modes oscillating in the laser. Figure 3.2 depicts this graphically.

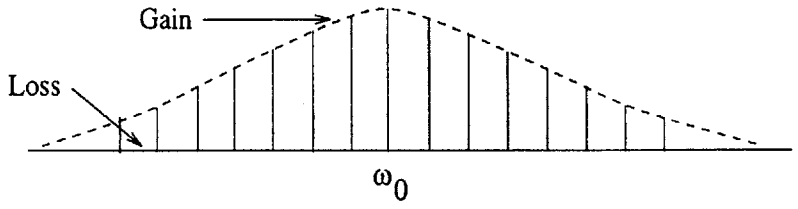

Figure 3.2 Longitudinal modes in a laser resonator.

In an ultrafast laser, there are thousands of such modes. For instance, in the Cr^{4+}:YAG laser, the output light typically spans 1200 to 1600 nm and has a repetition rate of 100 MHz; this translates into 625,000 possible axial modes to modelock. In general, for a cw laser, these longitudinal modes oscillate with no well-defined phase with respect to each other. The resultant temporal output is therefore randomly varying in time. This is demonstrated in Figure 3.3. These traces have been created by combining sine curves of equal amplitude but random phase relationships. In contrast, if the longitudinal modes are forced to oscillate with a fixed relationship with respect to each other, the output is a pulse of short temporal duration. To demonstrate this result, we look at the case where there are $2N+1$ axial frequency components oscillating with equal amplitude E_0 and constant relative phase between each

mode. We have

$$E(t) = \left(\sum_{-N}^{N} E_0 \exp i[(\omega_0 + n\Delta\omega)t + n\varphi] \right) \tag{3.3}$$

where ω_0 is the central frequency and $\Delta\omega$ is the frequency separation as given by Equation (3.2). Separating the field into a slowly varying part $A(t)$ and then expanding the sum, we get

$$E(t) = A(t)\exp(i\omega_0 t) \tag{3.4}$$

$$A(t) = \sum_{-N}^{N} E_0 \exp[in(\Delta\omega t + \varphi)] = E_0 \frac{\sin\left[\frac{(2N+1)(\Delta\omega t + \varphi)}{2}\right]}{\sin\left[\frac{(\Delta\omega t + \varphi)}{2}\right]} \tag{3.5}$$

Using a change of variable, the resulting output intensity is

$$I(t') \sim |E(t')|^2 = \left(E_0 \frac{\sin\left[\frac{(2N+1)(\Delta\omega t')}{2}\right]}{\sin\left[\frac{\Delta\omega t'}{2}\right]} \right)^2 \tag{3.6}$$

From this, the output of a modelocked laser is plotted in Figure 3.3, in comparison to that of a laser which is not modelocked. Evidently, the result of modelocking is that the longitudinal modes constructively interfere to produce a train of light pulses. Successive pulses in this train are separated by a time $\delta\tau$.

$$\delta\tau = \frac{2\pi}{\Delta\omega} = \frac{2L}{c} \tag{3.7}$$

Note that $\delta\tau$ is the cavity roundtrip time. This analytic result makes physical sense if one imagines the pulse to be bouncing back and forth inside the laser resonator. Each time the pulse encounters the output coupling mirror at one of the cavity, it leaks out a little light, producing the train of pulses that we see in the output. The distance between successive pulses is obviously the cavity roundtrip time.

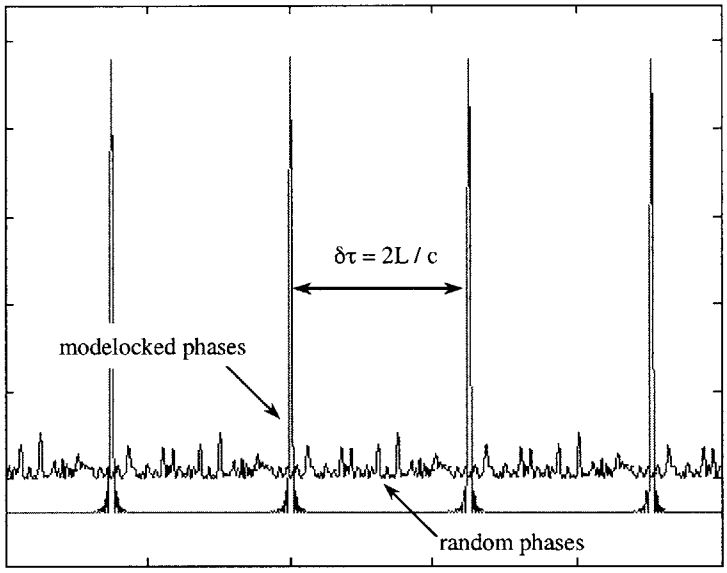

Figure 3.3 Random versus modelocked laser intensity output. Vertical axis has been altered for easier viewing.

Defining the pulse duration τ_p to be distance between the first two nulls, we get

$$\tau_p = \frac{4\pi}{(2N+1)\Delta\omega} \tag{3.8}$$

$$\tau_p = \frac{4\pi}{\Omega_g} \tag{3.9}$$

The second expression can be written because the total frequency span of the longitudinal modes equals the gain bandwidth Ω_g. This relationship between gain bandwidth and pulse duration is a fundamental property of all ultrafast lasers. The width of the pulse is inversely proportional to the number of contributing propagating modes, as illustrated in Figure 3.4 below.

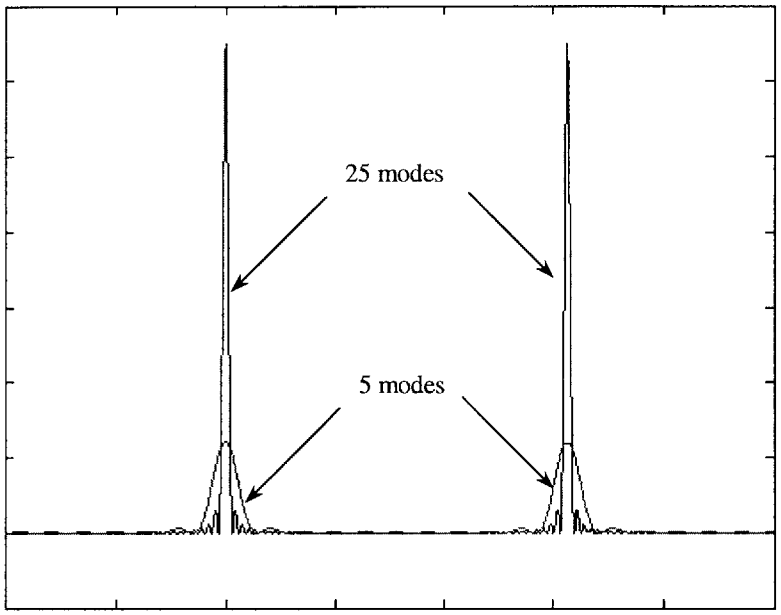

Figure 3.4 Dependence of pulse duration on the number of contributing resonator modes.

Modelocking is defined as a technique that forces the resonator longitudinal modes to oscillate with a certain phase relation relative to one another. Therefore, modelocking is inherently defined in the frequency domain. In fact, the term "modelocking" stems from early theoretical descriptions in the frequency domain [33]. It is easiest to describe modelocking in the frequency domain in terms of active modelocking. In active modelocking, a physical device, such as an acousto-optic modulator or an electro-optic modulator, is used to correlate the resonator modes. Consider placing a shutter at some fixed position in the cavity. At the instant the shutter is opened, a pulse of light passes through and all of the different longitudinal modes in that pulse are in phase. These modes must be in phase in order to constructively interfere to form the pulse. The shutter is then modulated at a frequency ω_0 exactly matching the spacing of the cavity modes $\Delta\omega$, as defined in Equation (3.2). Treating both the longitudinal modes and modulation as pure cosine waves, we see from Equation (3.10) below that modulating a mode of frequency ω in this manner will produce sidebands at $\omega \pm \omega_0$.

$$[1 + \cos\omega_0 t] \cdot \cos\omega t = \cos\omega t + \frac{1}{2}\cos(\omega - \omega_0)t + \frac{1}{2}\cos(\omega + \omega_0)t \tag{3.10}$$

These sidebands occur at frequencies that coincide with the frequencies of the neighboring resonant modes of the cavity. Therefore, those neighboring modes experience amplification of their field strengths, by coherent addition with the sidebands. Note that these coupled sidebands must be in phase with the parent mode. And through their coupling, the sidebands and the neighboring resonant modes become in phase. This, in turn, locks the phase of the adjacent resonant modes to the parent mode. Now imagine that all of the laser modes under the gain spectrum are modulated in this fashion, and that all of the sidebands couple with neighboring resonant modes. It becomes apparent that this technique must lock the phases of all of the resonant modes in the cavity, hence achieving modelocking. In reality, the number of resonant modes locked depends on the strength of the coupling, in other words the effectiveness of the modelocking.

We have pursued this discussion to illustrate the concept of modelocking in the frequency domain. In truth, however, active modelocking is not sufficient to produce the shortest possible pulse durations, and passive modelocking techniques are required. Although we have initially presented modelocking here in the frequency domain, time domain analysis provides a much simpler physical picture and theoretical model.

3.2 ACTIVE MODELOCKING

The method of modelocking falls under two basic categories – active and passive modelocking. In active modelocking, as discussed earlier, an external high-frequency signal, synchronized to the frequency of the mode spacing of the laser resonator, drives an intra-cavity modulator, a device typically employing an acousto-optic or electro-optic effect. The schematic of an actively modelocked laser is shown in Figure 3.5.

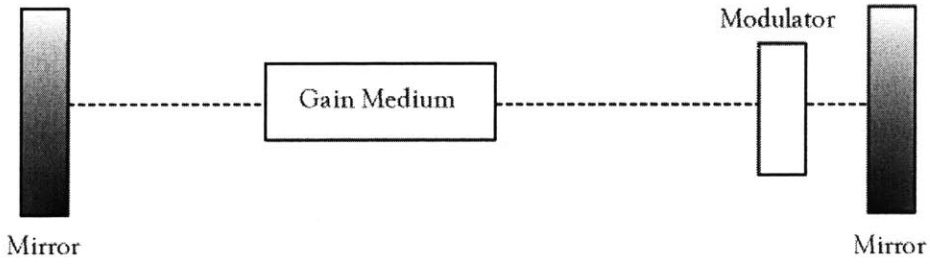

Figure 3.5 Schematic of an actively modelocked laser resonator.

Let us consider the effects of gain and loss in this resonator. The gain will have a frequency bandwidth Ω_g. If a short pulse is amplified with a bandwidth limitation, it will be broadened. This is the gain dispersion effect discussed in the previous chapter. The total gain, therefore, consists of a linear term along with this dispersion term.

$$g(\omega) = g\left(1 - \frac{(\omega - \omega_0)^2}{\Omega_g^2}\right) \tag{3.11}$$

Here, ω_0 is the center frequency of the gain spectrum. Converting this expression into a differential operator on the pulse shape *A(t)*, we get

$$\Delta A(t) = g\left(1 + \frac{1}{\Omega_g^2}\frac{d^2}{dt^2}\right) \tag{3.12}$$

Note that we are using the slowly-varying envelope approximation and only consider the pulse envelope *A(t)*, instead of the full electric field *E(t)*. The loss in this cavity consists of a constant nonsaturable loss L_0, along with an externally-driven loss from the optical modulator.

$$L = L_0 + L_m(1 - \cos\omega_m t) \tag{3.13}$$

where L_m is the modulation depth and ω_m is the modulation frequency, which is matched to the mode separation $\Delta\omega$. The laser generates pulses in the time window when the gain exceeds the cavity loss. This is illustrated below in Figure 3.6.

A differential equation governing the evolution of the pulse shape *E(t)* can now be written.

$$\left[g\left(1 + \frac{1}{\Omega_g^2}\frac{d^2}{dt^2}\right) - L_0 - L_m(1 - \cos\omega_m t)\right]A(t) = 0 \tag{3.14}$$

The expression is set to zero due to the self-consistency requirement that the optical pulse does not change after a round trip in the cavity. Equation (3.14) is called the master equation for actively modelocked lasers. For simplicity, we have neglected dispersion and self-phase modulation terms. The master equation is a form of the Mathieu equation and has periodic solutions called Hermite-Gaussians. The lowest-order solution is a Gaussian pulse envelope.

$$A(t) = A_0 \exp\left(-\frac{t^2}{2\tau_p^2}\right) \tag{3.15}$$

where the pulse duration τ_p is given by

$$\tau_p = \left[\frac{2g}{L_m \omega_m^2 \Omega_m^2}\right]^{1/4} \tag{3.16}$$

Therefore, in order to generate short pulses by active modelocking, broad gain bandwidths, high modulation depths, and high modulation frequencies (specifically short temporal modulation windows) are needed. The latter is one of the limiting factors of active modelocking. Referring to Figure 3.6, active modelocking will rapidly compress a long pulse whose τ_p is greater than the temporal modulation window. However, for pulses shorter than the window, modelocking action is greatly diminished. Consequently, we must rely on another modelocking technique – passive modelocking – to generate the shortest pulses.

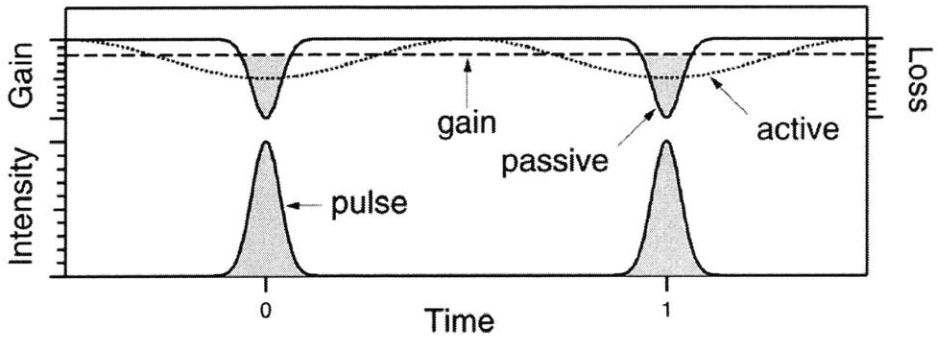

Figure 3.6 Active versus passive modelocking (with a fast saturable absorber).

3.3 COMPARISON OF ACTIVE AND PASSIVE MODELOCKING

The dynamics of active and passive modelocking are displayed in Figure 3.6. In passive modelocking, the modulation is created directly by the pulses. This is referred to as self-amplitude modulation (SAM). In both of these cases, the loss is smaller than the gain over the pulse duration, which opens a net gain window for the pulse. For active modelocking, the modulation of the loss is externally controlled; and, as a result, it cannot follow the fast changes of the pulse intensity profile. Ultimately, the external synchronization electronics place fundamental limitations on producible pulse durations. For passive modelocking, the modulation is determined by the pulse shape itself and consequently opens a much shorter gain window. Because the net gain window for the pulse determines the minimum achievable pulse duration, passive modelocking allows for much shorter pulses.

The pulse-shortening rate, or PSR, is a figure of merit that measures the strength of the modelocking. A detailed discussion of their derivations is given in Ref. [34]. We summarize the results here, in order to give a quantitative comparison of active and passive modelocking.

The PSR is defined as

$$PSR = \frac{\Delta\tau}{\tau} \tag{3.17}$$

where τ is the pulse duration and $\Delta\tau$ is the change in pulse duration per resonator roundtrip. For active modelocking, the PSR is

$$PSR_{active} = \frac{m\omega_m^2\tau^2}{4} \tag{3.18}$$

As mentioned earlier, the effectiveness of the external modulator decreases significantly as the pulse gets shorter. In comparison, the PSR for passive modelocking with a slow saturable absorber and a fast saturable absorber are

$$PSR_{slow,\,passive} = \text{constant} \tag{3.19}$$

$$PSR_{fast,\,passive} \propto \frac{1}{\tau} \tag{3.20}$$

Therefore, the PSR due to slow saturable absorber action does not lose its strength as the pulse gets shorter. In fact, for a fast saturable absorber, the modelocking action only gets stronger as the pulse duration decreases. As a result, passive modelocking is now the predominant technique for the generation of ultrashort pulses. A plot of the pulse-shortening rates for the different modelocking regimes is shown in Figure 3.7.

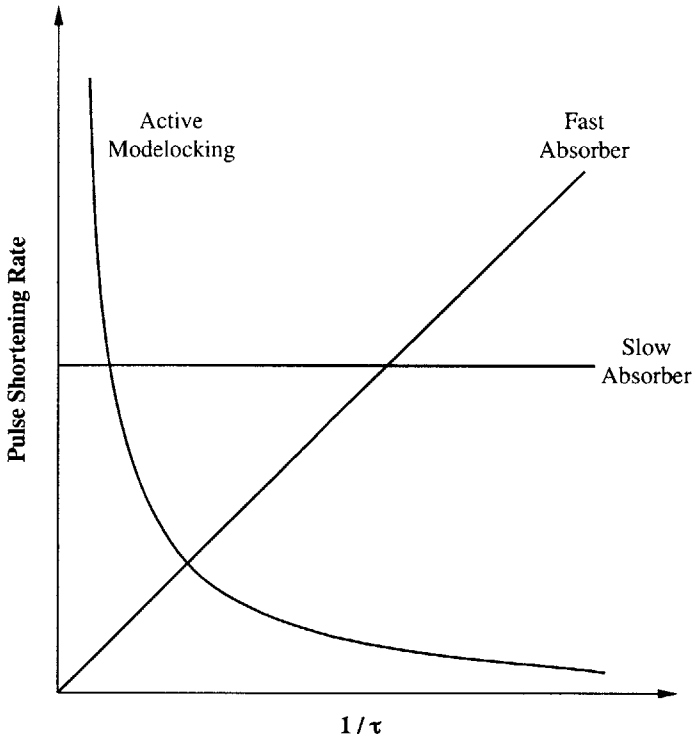

Figure 3.7 Pulse shortening rates for three different modelocking regimes.

3.4 PASSIVE MODELOCKING

In passive modelocking, an intracavity nonlinear element – a saturable absorber – is introduced to modulate the loss. Modelocking is achieved by self-amplitude modulation of the pulse in this element. In this sense, passive modelocking is similar in all systems – some mechanism induces self-amplitude modulation by the pulse, which in turn produces modelocking of its frequency components. However, the mechanism through which SAM occurs is different from one system to the next. In any case, the repeated action of the saturable absorber is to shorten the pulse with each passage through the absorber. This, however, cannot continue indefinitely. Equilibrium is reached when the spectral bandwidth of the pulse, which is inversely proportional to the pulse duration, is counteracted by the finite gain bandwidth, and by the interaction of GVD and SPM.

We look at the two limiting cases of passive modelocking – (1) slow saturable absorber modelocking - absorber recovery time is longer than the pulse duration [35], and (2) fast

saturable absorber modelocking - absorber recovery time is shorter than the pulse duration [36]. We begin with a qualitative discussion of the slow saturable absorber mechanism. We then review fast saturable absorber modelocking. Similar to what was done for active modelocking, we construct a master equation for fast saturable absorbers and analyze its results. We consider only the fast absorber mathematical model here because it is the most relevant to our experiment. Finally, we look at soliton modelocking, which falls into the passive modelocking category, but cannot be defined as a slow or fast absorber, in the traditional sense.

3.4.1 Passive Modelocking with a Slow Saturable Absorber

Passive modelocking was first demonstrated by Mocker and Collins in 1965 for a ruby laser [37] and later for a Nd:glass laser by DeMaria *et al.* in 1966 [38]. Said experiments involved fast saturable absorption. About seven years after Mocker and Collins' initial report, passive modelocking of a cw dye laser was demonstrated by Ippen and Shank [39]. This was a landmark result since the output was a stable, continuous train of picosecond pulses. The absorber recovery time was known to be on the order of several hundred picoseconds yet the pulse duration was on the order of one picosecond. Three years later in 1975, Haus was able to give a theoretical explanation of this slow saturable absorber modelocking [35]. In this section, we summarize these results.

A slow saturable absorber is a lossy element that becomes more transparent with increasing light intensity but cannot recover its absorption on the time scale of an ultrashort pulse [35]. It favors pulse generation but cannot do much shortening on a time scale less than its own recovery time, unless there exists dynamic gain saturation. Through absorber saturation, the laser pulse provides its own modulation. For this reason, modelocking by slow saturable absorbers can generate pulses much shorter than by active modelocking.

Consider the time evolution of a pulse travelling inside a resonator, which contains a saturable absorber and a gain medium. As the optical pulse passes through the saturable absorber, its leading edge is absorbed, saturating the absorber, which then allows the pulse peak to pass through unattenuated. The absorber, however, recovers fast enough to attenuate the trailing edge of the pulse, but not as much as the leading edge (for slow saturable absorbers). Upon passage through the gain medium, the trailing edge receives less amplification than the front edge because of gain saturation. The pulse shortening mechanism here relies on dynamic gain saturation to repetitively sharpen the trailing edge of a pulse, while a saturable absorber elsewhere in the cavity sharpens the leading edge. These dynamics are summarized in Figure 3.8. Finally, as the pulse comes in contact with a linear loss

element, the entire pulse is attenuated. With each roundtrip inside the cavity, the pulse is shaped and shortened until a steady state mode develops.

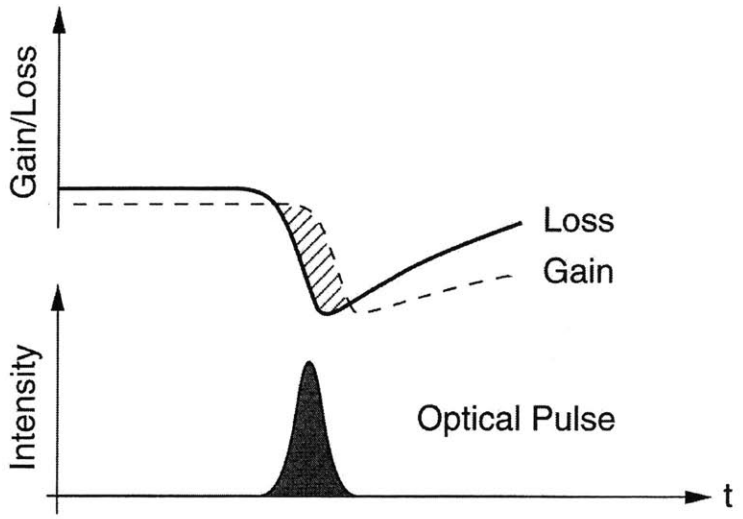

Figure 3.8 Pulse shaping gain and loss dynamics for slow saturable absorber passive modelocking. From Ref. [34].

There are three conditions that must be met to insure modelocking. First, the absorber cross section must be greater than the gain cross section. This first condition implies that the gain saturation energy must be greater than the absorber saturation energy. Since the peak energy is given by the time integral of the pulse intensity, it is crucial that the absorber saturates before the pulse peak and the gain saturates after the peak. This allows the center of the pulse to see a net gain. The second condition is that the gain recovery time must be greater than or equal to the cavity roundtrip time. This ensures sufficient but not complete gain recovery to amplify the pulse with each roundtrip. If the gain were to recover completely in a time shorter than the cavity roundtrip time, another pulse could form. To maximize the pulse energy, multiple pulsing should be avoided. Lastly, the saturated gain coefficient must be less than the sum of the linear loss coefficient and the saturated loss coefficient. This third criterion insures that the trailing edge has a net loss after each roundtrip. Meeting these three conditions allows the peak of the pulse to be amplified while attenuating both wings.

At steady state, a net gain time window as short as the pulse itself is necessary to stabilize ultrashort pulses. In a dye laser, which we have just described, the short net gain window is formed by both the saturation of a slow saturable absorber that opens the net gain window and the subsequent saturation of the gain that closes the window after passage of the pulse.

However, in solid state lasers, the upper-state lifetime is on the order of μs, which is much longer than the pulse repetition rate. This prevents dynamic pulse-to-pulse gain saturation, and the recovery time of the slow saturable absorber ultimately limits the shortest possible pulse duration. In this case, the classic slow absorber model with dynamic gain saturation no longer holds.

Typical recovery times of saturable absorbers are on the order of picoseconds. In this scenario, a fast saturable absorber is necessary to generate pulses on the order of femtoseconds. An alternative mechanism would be soliton modelocking, which relies on the interplay between group velocity dispersion and self-phase modulation to shape the pulse. We discuss this in Section 3.5.

3.4.2 Passive Modelocking with a Fast Saturable Absorber

A fast saturable absorber is an element that responds essentially instantaneously to changes in light intensity [36]. The laser can generate pulses without any aid from gain saturation dynamics since the saturable absorber can recover its initial absorption in a time shorter than the pulse duration. Fast saturable absorber dynamics were illustrated earlier in Figure 3.6.

As discussed previously, a fast saturable absorber can open a shorter net gain window than for a slow saturable absorber. Hence, the shortest optical pulses can be produced with fast saturable absorber passive modelocking. The fastest optical nonlinearities are reactive and nonresonant. This can be realized with artificial saturable absorber techniques, such as additive pulse modelocking (APM) and Kerr lens modelocking, which we will discuss in Section 3.6. These artificial absorbers have two clear advantages over real absorbers. First, they do not dissipate power, since they deflect power out of the laser instead of absorbing it. Secondly, the operational parameters of these fast saturable absorbers can be varied experimentally by optimizing the laser design [34]. We proceed now to the mathematics of fast saturable absorber modelocking.

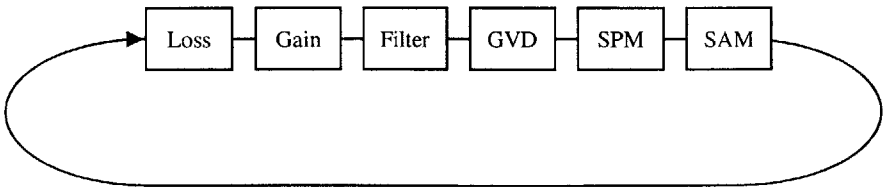

Figure 3.9 Elements in a passively modelocked laser resonator.

Figure 3.9 summarizes the basic elements in a passively modelocked laser resonator. As the pulse oscillates in the cavity, it encounters loss, gain, gain dispersion, group velocity dispersion, self-phase modulation, and self-amplitude modulation. The latter two effects have yet to be quantified, so we do that now. The self-phase modulation adds a phase factor to the pulse and is dependent on the instantaneous pulse intensity; therefore

$$\Delta A(t)_{SPM} = -j\delta|A(t)|^2 A(t) \tag{3.21}$$

Again, the slowly-varying envelope approximation has been used. Similarly, the self-amplitude modulation is dependent on the pulse intensity and provides a loss decrease for the pulse.

$$\Delta A(t)_{SAM} = \gamma|A(t)|^2 A(t) \tag{3.22}$$

where the coefficient γ is a measure of the SAM strength and varies from mechanism to mechanism. Putting all of these contributions together, we construct the master equation for passively modelocked lasers [40].

$$\left[g - L_0 + j\psi + \frac{g}{\Omega_g^2}\frac{d^2}{dt^2} + \tau_g\frac{d}{dt} + jD\frac{d^2}{dt^2} + (\gamma - j\delta)|A(t)|^2\right]A(t) = 0 \tag{3.23}$$

where g is the gain per pass, L_0 is the nonsaturable loss, ψ is the optical phase slip, Ω_g is the gain bandwidth, and T_g is the group delay, or the timing shift per roundtrip. The term with the dispersion parameter D is the total GDD accumulated per cavity roundtrip, multiplied by a factor of ½. Finally, the last two terms are associated with SAM and SPM, as defined earlier. The analytical solution to the master equation is

$$A(t) = A_0 \operatorname{sech}\left(\frac{t}{\tau}\right)^{1+i\beta} = A_0 \operatorname{sech}\left(\frac{t}{\tau}\right)\exp\left[i\beta \ln \operatorname{sech}\left(\frac{t}{\tau}\right)\right] \tag{3.24}$$

The pulse is completely characterized by amplitude A_0, pulse duration τ, and a chirp parameter β. In turn, these parameters are all functions of the self-amplitude modulation, self-phase modulation and dispersion present in the cavity. The hyperbolic secant pulse shape is indicative of passive modelocking in general. Even though the master equation above was based on a fast saturable absorber model, pulses modelocked by slow saturable absorbers also exhibit this hyperbolic secant pulse shape [35]. This is in contrast to the Gaussian pulse shape that is indicative of active modelocking. Substituting the solution back into the master equation, one arrives at four equations, which may be solved for four parameters – the phase shift ψ, the chirp β, the pulse duration τ, and the pulse energy. The important features of the

solutions are summarized in Figure 3.10 below. Here, the chirp β, the pulse duration τ, the spectral bandwidth of the pulse, and a stability parameter are plotted versus dispersion for a fixed SAM while varying the SPM. For the pulse to be stable, the stability parameter in Figure 3.9 (d) must be positive.

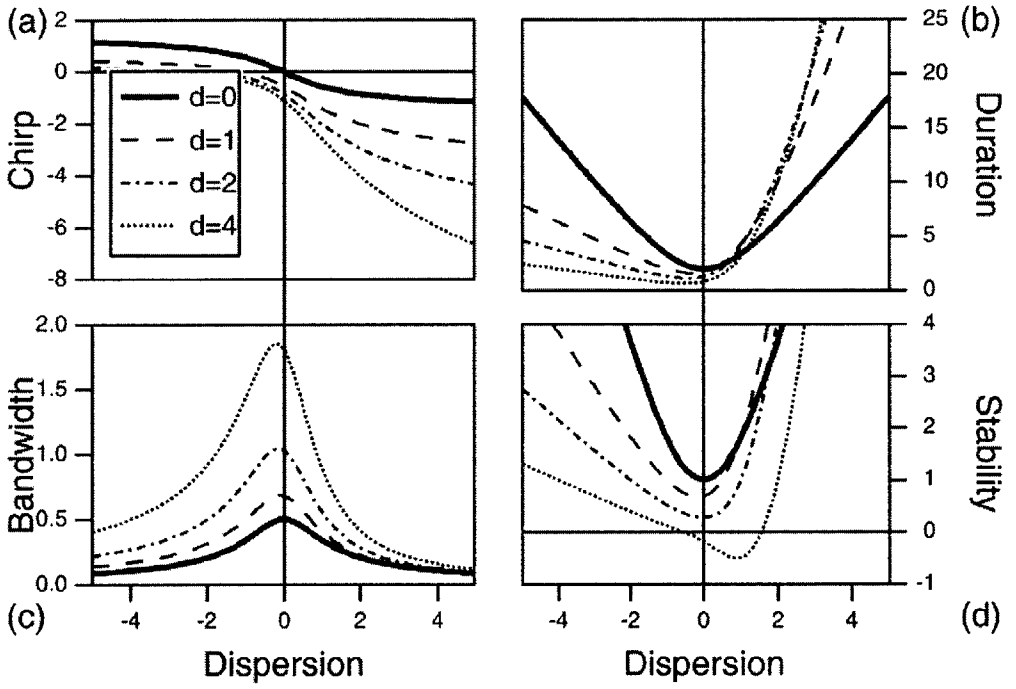

Figure 3.10 Pulse parameters versus dispersion for fixed self-amplitude modulation strength and varying SPM coefficients. From Ref. [41].

Two distinct regions of operation with qualitatively different pulse shaping mechanisms can be identified. For positive GVD, the chirp parameter β can become quite large and the resultant pulse durations are long. In this case, filtering due to the limited gain bandwidth actually acts as a pulse shortening process due to the chirped nature of the pulses. The pulse shortening is balanced by the positive GVD and the spectral narrowing is compensated for by SPM. The magnitude of SAM action (parameter γ) has a strong influence on the pulse duration here.

In the negative GVD regime, the situation is quite different. Negative dispersion is required to counteract SPM to attain short pulses with small amounts of chirp. Soliton effects dominate the pulse shaping. The minimum pulse duration can be achieved in this operating mode, with large SPM and a small amount of negative GVD. Saturable absorber action is

critical in stabilizing the pulse formation process by providing discrimination against perturbations and breakthrough of cw radiation.

The stability criterion states that the saturated gain seen by the wings of the pulse must be less than the loss in order to avoid breakthrough cw radiation before and after the pulse. SPM strongly affects the stability of the laser. A pure soliton laser, in the absence of saturable absorber action, is never stable because the finite bandwidth of the soliton will make it experience less gain than cw radiation. Likewise, too much SPM can drive a laser unstable even in the presence of saturable absorber action. This is because with too much SPM, in the presence of the spectral filtering of the gain, the pulse gradually begins to lose energy. Consequently, the saturated value of the gain rises and the stability condition is violated.

The results stated here hold true for any fast saturable absorber modelocked laser. The master equation approach is valid as long as the changes of the pulse in the nonlinear elements per roundtrip are small. Pulses with duration of several ten femtoseconds can normally be described in this framework. Extremely short pulses in the sub-10 femtosecond regime, however, change their shape significantly within the individual resonator components. For example, even for a thin laser crystal, its linear dispersion may well stretch the pulse by one order of magnitude. The results of the master equation given above do not strictly apply anymore for such short pulses, but still helps for intuitive understanding of the modelocking dynamics. One consequence of this is that the ordering of the intracavity elements becomes important. We will briefly touch on this effect next.

3.4.3 Soliton Modelocking

Soliton modelocking relies on the interaction between anomalous group velocity dispersion and self-phase modulation. As described earlier, the two effects counteract each other to produce a chirp-free pulse. Soliton modelocking dynamics are illustrated in Figure 3.11 below. As discussed previously, the traditional concept of pulse generation relies either on the interplay between a slow saturable absorber and gain saturation or a fast saturable absorber to open a net gain window in which to shape the pulse. The gain window closes immediately before and after the passage of the pulse. Review Figures 3.6 and 3.8 for reference. This, however, is not the case for soliton modelocking. Even a saturable absorber with recovery time greater than the pulse duration can stabilize the pulse. In such a system, any low intensity noise or instabilities spread in time due to linear dispersion, since they are not intense enough to experience the necessary SPM to counteract the GVD. Upon dispersing, these instabilities expose themselves to the higher absorption from the slowly-recovering saturable absorber after passage of the main soliton pulse. Consequently, these

perturbations see less gain than the soliton per cavity roundtrip and decay away in time.

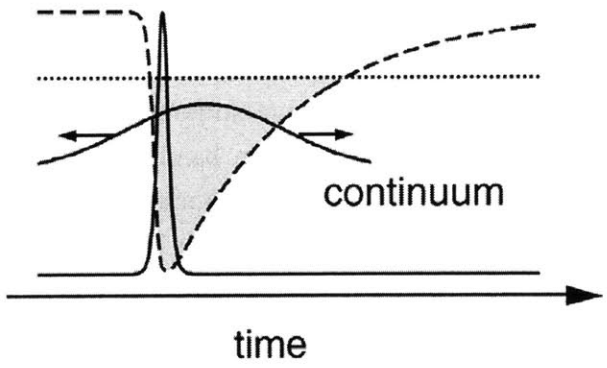

Figure 3.11 Net gain window for soliton modelocking. Low-intensity background continuum spreads in time and experience higher losses from the absorber. Adapted from Ref. [42].

A laser operating in the soliton modelocking regime can produce pulses two to four times shorter than that achievable by self-amplitude modulation alone [41]. In this manner, soliton modelocking may be identified as a slow absorber mechanism, since pulses shorter than the absorber recovery time are produced. However, keep in mind that pulse shaping is dominated by soliton effects, and not by SAM. Therefore, the slow saturable absorber model [35] no longer applies and we need to develop another.

Let us consider pure soliton effects, in the absence of self-amplitude modulation. By doing so, we can gain some insight into the basic dependencies of the pulse shaping. Soliton pulse shaping in fiber relies solely on GVD and SPM. Evolution of the pulse shape is governed by the nonlinear Schroedinger (NLS) equation, which is derived in detail in Ref. [18].

$$\frac{\partial}{\partial z}A(z,t) = \left[-\frac{\alpha}{2} - \frac{i\beta_2}{2}\frac{\partial^2}{\partial T^2} + i\delta|A(t)|^2\right]A(z,t) \tag{3.25}$$

where $A(z,t)$ is the pulse envelope, α is a measure of the fiber loss, β_2 is the GVD and δ is the SPM coefficient. By using the inverse scattering method, one can obtain the lowest-order solution to the NLS equation, or the fundamental soliton.

$$A(z,t) = A_0 \operatorname{sech}\left(\frac{t}{\tau}\right)\exp\left[-i\,\frac{\beta_2}{2\tau^2}\,z\right] \tag{3.26}$$

where τ is the pulse duration. For the fundamental soliton, the pulse duration τ and the envelope amplitude A_0 obey the area theorem.

$$A_0\tau = \sqrt{\frac{|\beta_2|}{\delta}} \tag{3.27}$$

Therefore, the pulse width is shortest for near-zero GVD and high peak powers. This result is in agreement with our earlier analysis of fast saturable absorber modelocking. Referring to Figure 3.10, the shortest pulse durations were achieved with high SPM, attributed to high peak powers, and a slightly negative GVD. Recall that GVD must be negative in order to observe these soliton effects.

Note that Equation (3.26) is very similar to that found earlier for the fast saturable absorber model in Equation (3.24). Both have a hyperbolic secant pulse shape, as expected for passive modelocking. However, bear in mind that the chirp parameter β in Equation (3.24) is artificial, in the sense that it comes from an initial ansatz and is really a function of the self-amplitude modulation, as well as GVD and SPM. In the model considered here, the effects of SAM were neglected and the solution in Equation (3.26) is only a function of GVD and SPM.

Experimentally, soliton modelocking can easily be identified by the power dependence of the pulse duration, from Equation (3.27). Another clue is the existence of cw sidebands in the pulse spectrum, or so-called Kelly sidebands [43]. These are generated by the coupling of light from the soliton to background radiation, through phase matching. As an example, in the case of a soliton coupling to continuum propagating through a medium with second-order dispersion, the spectral offsets of the Kelly sidebands from the center frequency of the pulse spectrum are

$$\Delta\omega = \frac{1}{\tau}\sqrt{\frac{4\pi m\tau^2}{\beta_2 z_c} - 1} \tag{3.28}$$

where m is an integer and Z_c is the cavity length. This phase matching phenomenon also occurs for higher-order disperison. Kelly sidebands, generated from second- and third-order dispersion phase matching, are illustrated in Figure 3.12. Note that for TOD, the sidebands are not symmetric, as one clearly dominates.

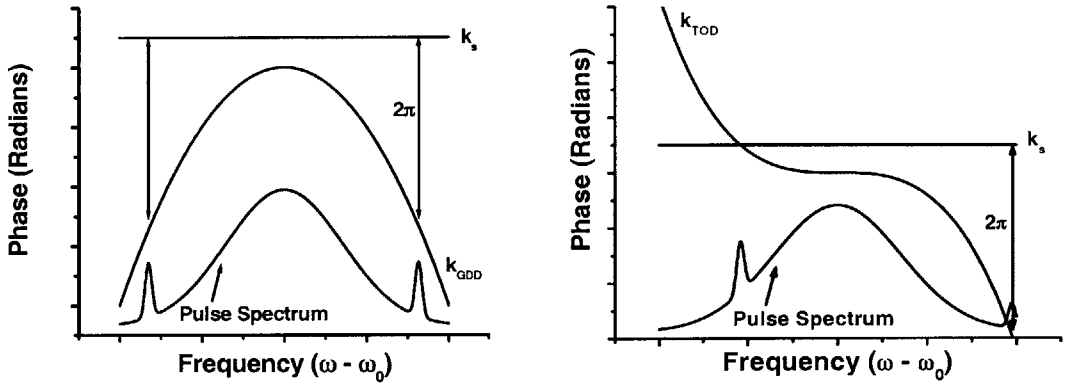

Figure 3.12 Schematic of Kelly sidebands for GDD and TOD phase matching.

The nonlinear Schroedinger equation relies on the slowly-varying envelope approximation, which assumes that the pulse does not undergo dramatic changes over the course of a roundtrip. In addition, analysis using the NLS equation assumes a constant dispersion map. Therefore, in modeling an ultrafast laser cavity, we must assume that the GVD is averaged over the entire cavity, instead of regarding it in discrete segments. Unfortunately, this analysis fails for extremely short pulses on the order of a few optical cycles. In order to study these scenarios, we must turn to a new model, termed dispersion-managed modelocking [44]. Here, the generation of ultrashort pulses is modeled after dispersion-managed long-distance nonlinear optical pulse propagation in fibers. Using numerical techniques, such as the split-step Fourier method, one can study the dependence of pulse shaping on the dispersion map [18]. In such laser systems, the ordering of the intracavity elements becomes analogous to the dispersion maps present in a fiber, and, consequently, is a very important design parameter. The principal difference from the soliton modelocking model we have just discussed to dispersion-managed modelocking is that the optical pulse stretches and compresses, or breathes, appreciably over the course of one resonator roundtrip. Hence, a pulse can have significantly different durations at different positions inside the resonator. This effect must be taken into consideration in the design of a laser resonator, in order to produce the shortest possible pulses.

3.5 TWO EXAMPLES OF SATURABLE ABSORBERS

3.5.1 Saturable Bragg Reflector

An important issue for real-world applications of modelocked lasers is operational simplicity. An ultrafast laser needs to be able to self-start, and pulsed operation must be stable. Artificial fast saturable absorber mechanisms, such as Kerr lens modelocking, are typically not self-starting. Recall the pulse shortening rates discussed earlier. The PSR for fast absorbers is inversely proportional to the pulse duration. As a result, initially, when the pulses are long, modelocking strength is very weak. Nonlinear effects in the cw-operation regime are typically insufficient to initiate modelocking. Therefore, in order to start pulse formation, a significant perturbation of cw operation is required. KLM is often started by slightly tapping an end mirror in the resonator. This creates a noise spike which acts as a seed for starting KLM action. No such action is required for many real saturable absorbers. For those absorbers classified as slow, the PSR is constant. Consequently, modelocking is readily initiated by such absorbers. For fast absorbers and those absorbers without gain saturation, one has to consider another figure of merit, the modelocking build-up time T_{MBT}, to determine self-starting conditions. The shorter the build-up time, the easier it is to self-start the laser system. For an absorber recovery time τ_A that is short compared to the cavity rountrip time τ_R, the approximate modelocking build-up time is found to be [45]

$$\frac{1}{T_{MBT}} \approx \left(\frac{2q_0}{E_A} \tau_A - \frac{2g_0}{(2m\pi)^2 T_L^2 P_L} \right) P \tag{3.29}$$

where P is the intracavity laser power, $2q_0$ is the modulation depth of the saturable absorber, E_A is the saturation energy of the absorber, g_0 is the small-signal amplitude gain coefficient, T_L is the normalized upper-state lifetime, and P_L is the saturation power of the laser gain. As expected, modelocking build-up time is short for large intracavity powers. The second term on the right determines the threshold condition for self-starting as a function of the laser parameters. Most importantly, the first term shows that a small saturation energy and a long absorber recovery time support the self-starting of modelocking. Therefore, the fast response of the artificial absorption due to KLM is a hindrance to self-starting.

A saturable Bragg reflector (SBR) is an ideal absorber that satisfies the aforementioned self-starting conditions. It has a low saturation energy and long recovery time. Regarding the latter property, saturable Bragg reflectors typically exhibit bitemopral behaviour. Pump-probe studies of broadband SBRs show a short time constant resulting from intraband thermalization, but also a long time constant on the order of picoseconds resulting from carrier

trapping and recombination. We benefit from this long time constant according to Equation (3.29) because it is responsible for the self-starting. In addition to starting pulse formation, an SBR, acting in conjunction with soliton modelocking or Kerr lens modelocking, can also help to stabilize pulses by suppressing cw instabilities. The first solid state laser to be modelocked with an intracavity saturable Bragg mirror was a color-center laser in 1989, producing pulses of 275 fs duration [46]. Since then, they have been used to self-start modelock many other solid state lasers, including Nd:YAG, Nd:YVO_4, Ti:sapphire, Cr:forsterite, and Cr^{4+}:YAG [45].

A saturable Bragg reflector is a nonlinear mirror device for laser modelocking that provides saturable absorption while maintaining low nonsaturable insertion loss. An SBR consists of a high-reflectance distributed Bragg reflector (DBR), on top of which a saturable absorber region is grown together with a transparent spacer layer. The saturable absorption is provided by either bulk material or semiconductor quantum well(s). Light at a designed wavelength is absorbed and excites carriers from the valence band to the conduction band. As the intensity of the incident light increases, more and more carriers are excited from the valence band, until all the states in the conduction band are filled. At this point, the absorber is saturated, or "bleached"; and light passes through the absorber unattenuated and gets fully reflected by the DBR. Figure 3.13 illustrates this intensity-dependent reflectivity.

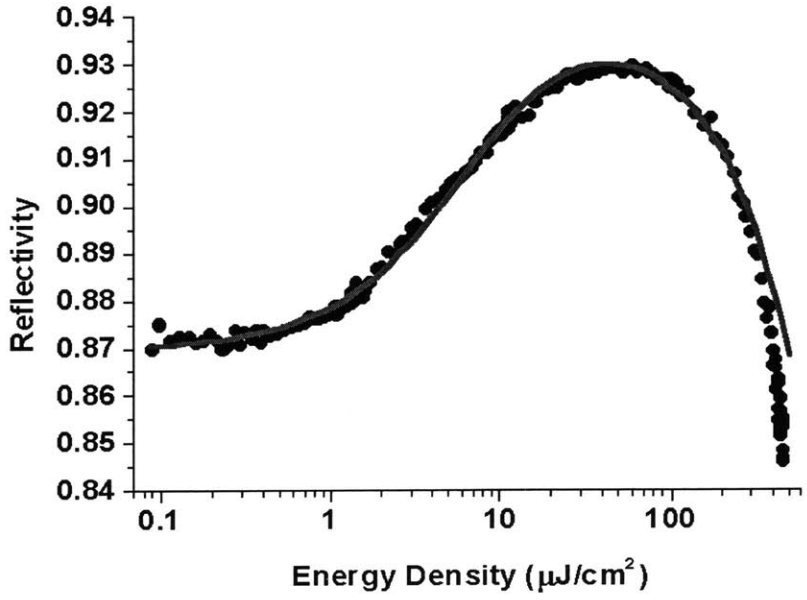

Figure 3.13 Measured reflectivity as a function of fluence in a sample saturable Bragg reflector [47].

Here, a single beam measurement of the reflectivity of a sample SBR is measured as a function of incident fluence. Initially, the reflectivity increases with fluence, as expected from the "bleaching" process discussed previously. Therefore, at low incident energy densities, the SBR functions as an intensity-dependent loss element, discriminating against low intensity light and favoring high intensities, like any saturable absorber. At high energy densities, however, the reflectivity levels off and eventually decreases, due to the additional losses contributed by two-photon absorption and subsequent free carrier absorption. Consequently, if the incident fluence is too high, the SBR loses much of its modelocking effectiveness. This must be taken into consideration in the design and use of the SBRs.

The key design characteristics of an SBR are reflectivity, insertion loss or nonsaturable loss, saturable loss, saturation intensity, dispersion, and the field distribution inside the device. An ideal SBR would have high reflectivity, low insertion loss, high modulation depth, no dispersion, a high damage threshold, and be simple and cheap to fabricate. Adjustable design parameters include the choice of semiconductor materials in the Bragg mirror, the number of semiconductor layers, the choice of an absorber, and the position of the absorber within the device. There are several constraints imposed on said parameters that are largely due to the epitaxial fabrication techniques used to grow SBRs. These constraints include lattice matching of successive semiconductor layers and the limited choice of semiconductor materials that can be used in a given fabrication system.

The reflectivity and dispersion of the SBR are mainly determined by the DBR underneath the absorber. Just like the Bragg mirrors described in Chapter 2, the high-reflectance bandwidth of DBRs increases with layer index contrast and the number of semiconductor layers. The reflectivity and dispersion of such structures can be calculated using transfer matrix methods [48]. In order to be used in a laser cavity, the reflectivity should be greater than 99% over the operating laser bandwidth. Therefore, nonsaturable loss must be kept to a minimum. As discussed earlier, dispersion inside the laser resonator is a crucial factor in ultrashort pulse generation. The dispersion of DBRs is relatively flat and close to zero over the high-reflectance spectral range, with strong oscillations at the edges.

Knowledge of the electric field distribution inside an SBR is required in order to adjust the effective saturation properties of the absorber. The incident intensity that the quantum wells are exposed to is dependent upon the location of the quantum well within the SBR structure. The standing wave condition created as the light reflects from each index discontinuity has maxima at the surface of every high-to-low index discontinuity (as seen from the surface of the SBR). Field nulls exist at the index discontinuities between the peaks. Furthermore, the magnitudes of the maxima decrease exponentially with depth into the mirror. An example of this can be seen in Figure 3.14. Consequently, the effective intensity

incident on the quantum wells can be engineered by proper selection of their location. If large saturation intensities are desired, the quantum wells can be placed either near a null or deep within the SBR structure. Likewise, for small saturation intensities, the wells should be placed near an intensity maximum.

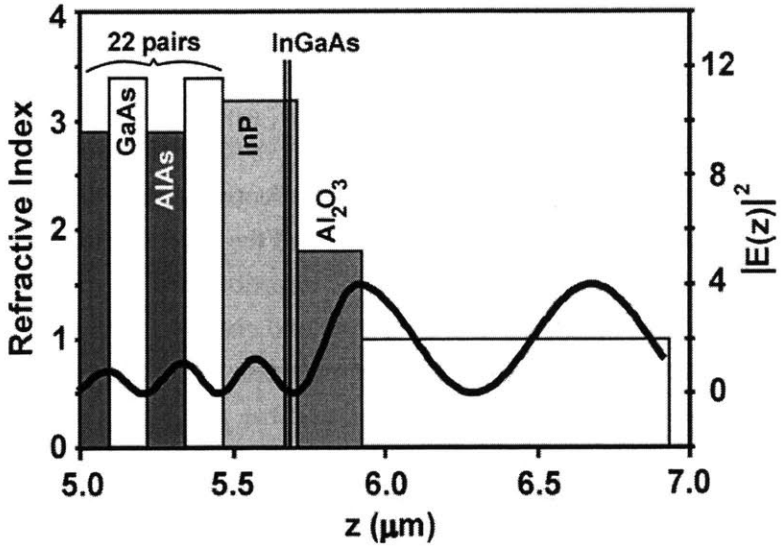

Figure 3.14 Schematic of a sample saturable Bragg reflector containing 2 quantum wells [47]. The refractive index of each layer and the magnitude squared of the electric field are plotted as a function of depth into the structure.

We have summarized here the main design parameters of a saturable Bragg reflector. In Chapter 4, we present an SBR structure used to self-start modelock the Cr^{4+}:YAG laser. The saturable absorber by itself can only generate pulses on the order of its recovery time, picoseconds. Such seed pulses can then enable the alignment of the laser resonator for Kerr lens modelocking, which in turn further shapes and shortens the pulse. At that point, the SBR effectively becomes a Bragg mirror, and the saturable absorber structure only functions to stabilize the pulse by discriminating against cw perturbations.

3.5.2 Kerr Lens Modelocking

Kerr lens modelocking (KLM) is one form of an artificial saturable absorber. This technique achieves fast saturable absorber action using self-focusing and aperturing. KLM was first proposed for ultrashort pulse generation as early as 1975 [49], however it wasn't until 1991 that it was first achieved in a Ti:sapphire laser [50]. Incidentally, this group from the University of St. Andrews in Scotland was not trying to build a KLM laser; but, serendipitously, the resonator was tuned just right and someone noticed. At the time, it was

believed that Ti:sapphire could not self modelock, so puzzled researchers termed this phenomenon "magic" modelocking. Six months passed before Salin *et al.* [51] from the University of Michigan were able to identify the origin of the modelocking to be self-induced Kerr lensing. Since then, there has been an explosion in the research of KLM in Ti:sapphire and other solid-state laser systems, such as Cr^{4+}:YAG. Today, KLM is the dominant laser design for achieving the shortest possible pulse durations.

KLM relies on intracavity nonlinear self-focusing effects, which are produced by the nonlinear index of refraction n_2 of the solid-state gain medium. Recall that for high laser intensities, the Kerr effect is

$$n = n_0 + n_2 I \tag{3.30}$$

The nonlinear addition n_2 is a result of the third-order optical susceptibility χ_3, as discussed in the previous chapter.

The phenomena of self-focusing is the most important consequence of the Kerr effect in the context of modelocking. Consider a pulse propagating through a nonlinear material. The pulse will typically have a Gaussian transverse spatial profile (TEM). Hence, the center of the beam will have a higher intensity than its wings. In the presence of the Kerr effect, the center of the pulse is subject to a greater index of refraction within the Kerr medium than the wings. Consequently, the phase velocity of the wave front will be less at the center of the pulse than at the wings. Thus, in effect, a lens is induced within the medium and the beam becomes focused. This is illustrated schematically in Figure 3.15. This self-focusing or induced lens effect is known as a Kerr lens.

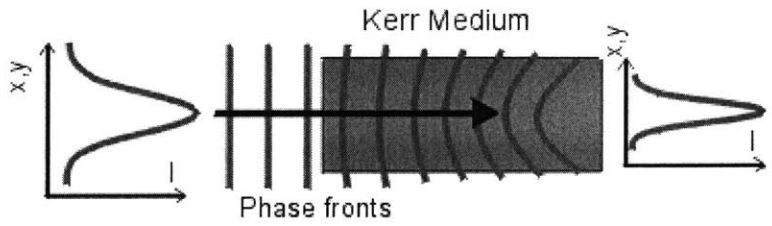

Figure 3.15 The Kerr lens effect on a transverse spatial beam profile.

Stated very simply, Kerr-induced self-focusing in nonlinear media results in the modification of intracavity beam profiles for high intensities in comparison with low intensity

profiles. As a result, at certain locations in the laser resonator, light of higher intensity may produce a narrower transverse spatial profile than light of lower intensity. If a spatial aperture is placed at such a point to selectively transmit the high intensity profile, the result is precisely an intensity-dependent loss mechanism, or saturable absorber. This is demonstrated below in Figure 3.16. A real physical aperture is placed inside the resonator at a location where the intensity-dependent change in the spatial beam profile is greatest. The reduction in loss during the net gain window for the pulse is proportional to the decrease in beam radius at the aperture with increasing power. This technique is referred to as "hard aperture KLM".

Alternatively, the cavity can be designed such that the Kerr lens allows the pulsed mode to experience greater overlap with the pump beam in the gain medium. Gain is constrained to a finite spatial region, due to optical pumping by a second laser beam (in the case of the Cr^{4+}:YAG). Consequently, a beam of diameter greater than the gain region receives less amplification than a beam of a slightly narrower diameter, because there is greater overlap between the narrower beam and the gain region. The increase in gain is proportional to the reduction of the laser mode area due to self-focussing. This phenomenon is termed "soft aperture KLM". Since an increase in gain is equivalent to a reduction in loss, hard and soft apertures are effectively the same.

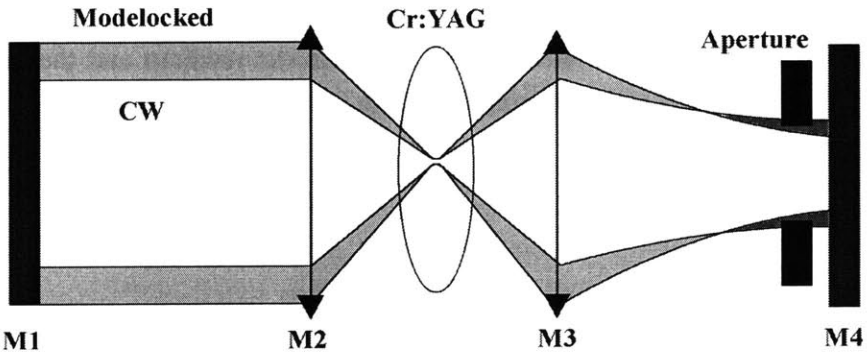

Figure 3.16 Transverse beam size variation in Kerr lens modelocking. M1 and M2 are the resonator end mirrors and M3 and M4 are the center focusing mirrors. The additional Kerr lens in the crystal decreases the beam radius and therefore the loss at the intracavity aperture.

There are several advantages in using Kerr lens modelocking. For one, there is no additional intracavity element that needs to be added, in contrast to real saturable absorbers. As a result, there are no additional dispersion or nonsaturable loss factors to consider. Secondly, the artificial fast saturable absorber in KLM is as fast as the Kerr nonlinearity,

which is estimated to be on the order of a few femtoseconds [52]. In addition, the Kerr effect is a non-resonant effect, in contrast to excitation in real saturable absorbers; therefore, KLM can be employed for ultrashort pulse generation over a wide range of wavelengths. This permits the production of wavelength tunable femtosecond light sources. Finally, the performance of artificial absorbers, such as KLM, can be varied experimentally much more easily than real absorbers. The only drawback to Kerr lens modelocking, which is inherent in all fast saturable absorber mechanisms, is that self-starting is difficult. For this, we turn to devices such as SBRs, as discussed previously.

Chapter 4

THE ULTRAFAST Cr^{4+}:YAG LASER

We have designed and built a prismless Cr^{4+}:YAG laser that generates pulses as short as 20 fs with 400 mW average power at a repetition rate of 110 MHz. The corresponding pulse spectrum extends from 1310 to 1500 nm FWHM and peaks at 1450 nm. In this chapter, we present various aspects of the resonator design and summarize the experimental results of said laser. In addition, we present the performance of novel broadband saturable absorber Bragg mirrors, which have been designed, fabricated, and used to self-start modelocking in the Cr^{4+}:YAG laser. These absorbers are designed to operate in the slow saturable absorber regime, generating picosecond seed pulses, which then act as catalysts for Kerr lens modelocking. The mirrors, consisting of high-index-contrast GaAs/Al_xO_y Bragg stacks, have broad enough bandwidths to support ultrafast Cr^{4+}:YAG pulses. Using these saturable Bragg reflectors, we were able to generate 35 fs pulses, with spectrum centered at 1490 nm and a FWHM of 68 nm.

4.1 THE PRISMLESS Cr^{4+}:YAG LASER

In previous work, Tong *et al.* [53] generated pulses as short as 43 fs from a Kerr lens modelocked Cr^{4+}:YAG laser using only fused silica prisms for group velocity dispersion compensation. The minimum pulse duration in this laser was reportedly limited by third-order dispersion. For the work presented here, double-chirped mirrors were used for broadband higher-order dispersion compensation. Pulses as short as 20 fs were generated directly from a prismless Cr^{4+}:YAG [54]. In this section, we review all components of the cavity design and discuss the results of our experiments.

4.1.1 Dispersion Compensation

For this work, as an alternative to prisms, we have used double-chirped mirrors (DCMs) to compensate group velocity dispersion, as well as higher-order dispersion. In addition, these DCMs provide a large mirror bandwidth, a necessity in supporting ultrashort pulses. The design of DCMs is very complicated and requires the use of complex numerical optimization techniques. Typical chirped mirrors consist of about 50 layers, so a computer program would have to search a parameter space of 50 dimensions for a good minimum of a merit function. In addition, DCMs are difficult to fabricate, due to the typically large number of layers and the precise control of the layer thickness required. The work described in this thesis was enabled by the design of mirrors in the Cr^{4+}:YAG spectral range by Prof. Franz Kärtner and by the fabrication of these mirrors by Scheuer *et al* [23,54].

The DCMs used in our Cr^{4+}:YAG laser consist of 48 layers of SiO_2 and TiO_2, and were grown by a state-of-the-art ion-beam sputtering technique. The refractive indices of SiO_2 and TiO_2 are 1.5 and 2.0, respectively. A schematic of the DCM structure is shown in Figure 4.1.

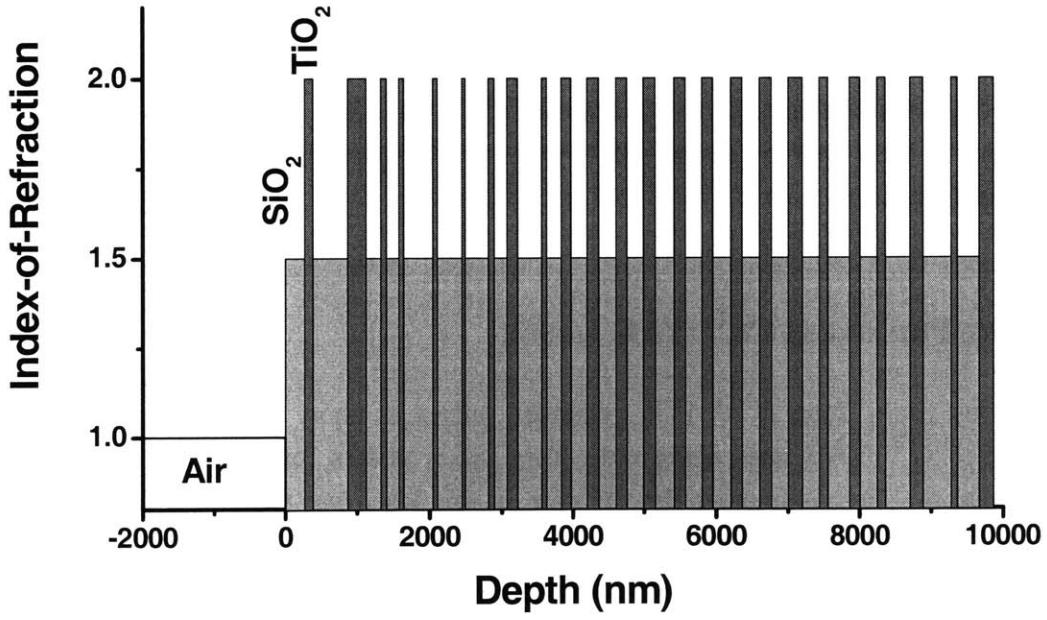

Figure 4.1 Schematic of double-chirped mirror structure designed for use in the Cr^{4+}:YAG. The index of refraction is plotted as a function of depth into the mirror.

The DCMs are designed to have broadband reflection coinciding with the Cr^{4+}:YAG gain spectrum, as well as high transmission at 1064 nm for the Nd:YVO_4 pump light. The mirror reflectivity was measured using a CARY spectrophotometer and is shown in Figure 4.2. The DCM is highly reflective in the spectral range from 1200 to 1700 nm, and is highly transmissive from 1000 to 1120 nm.

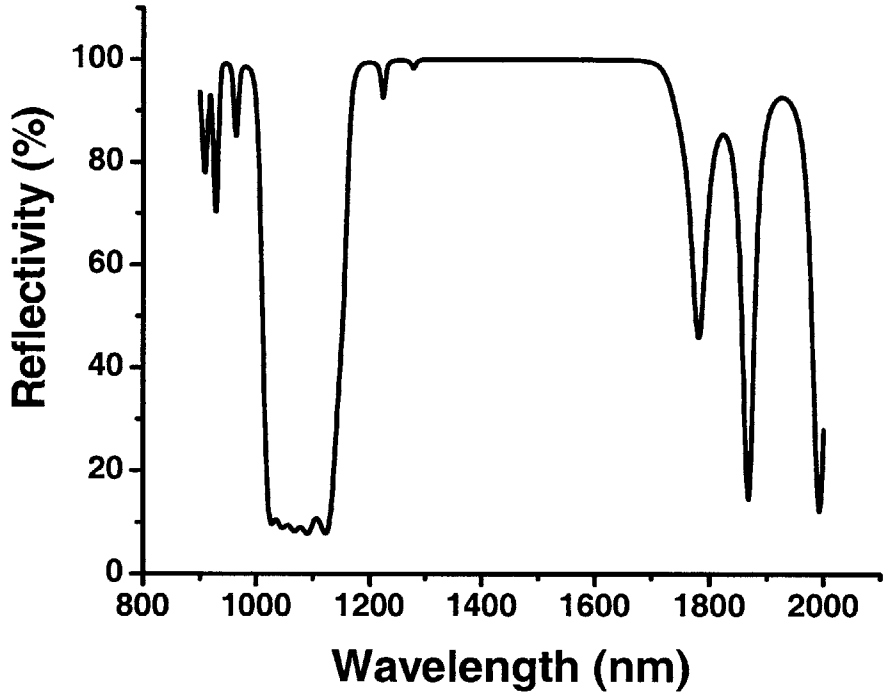

Figure 4.2 Measured reflectivity of double-chirped mirrors designed for use in the Cr^{4+}:YAG laser.

The group delay dispersion of the DCM is measured in a white light Michelson interferometer [55]. This technique uses the fast Fourier transformation of a white light interferometric cross-correlation to measure the group delay. The GDD of the DCM is shown in Figure 4.3. The DCM has an approximately linear anomalous dispersion from 1325 to 1575 nm; and the GDD and TOD per reflection at 1500 nm are roughly 125 fs^2 and 1000 fs^3, respectively. The measured GDD agrees quite well with the intended design and exhibits a relatively smooth profile from 1350 to 1600 nm, in contrast to the dramatic oscillations seen in simple-chirped mirrors. Consequently, the third-order dispersion of the DCM in this range is roughly constant and is of opposite sign to the TOD of the Cr^{4+}:YAG material.

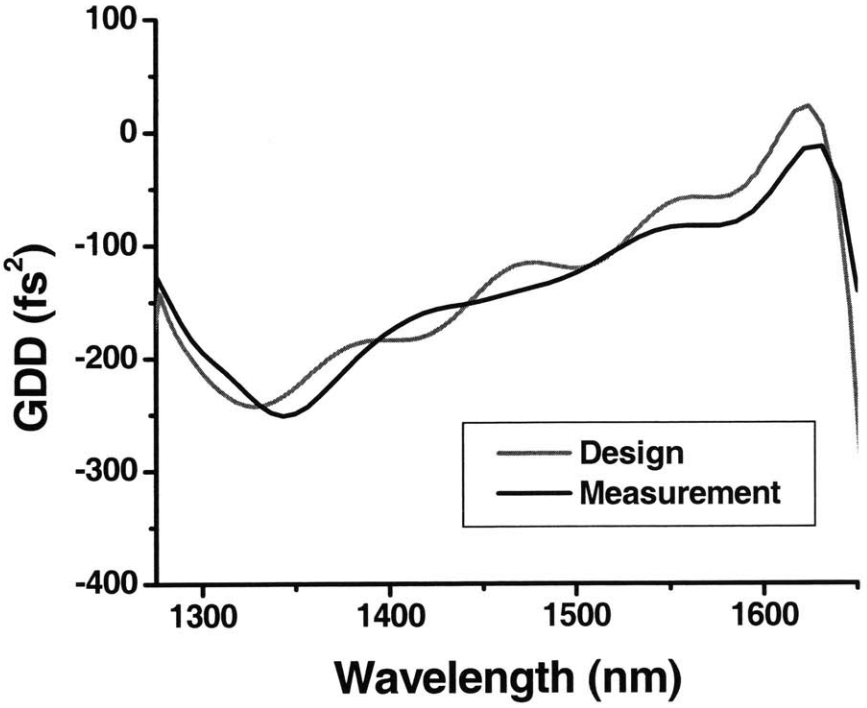

Figure 4.3 Designed and measured group delay dispersion of the double-chirped mirrors used in the Cr^{4+}:YAG laser.

Originally, these DCMs were designed for use with a 1 cm Cr^{4+}:YAG laser crystal; however, after the mirrors had already been fabricated, it was determined that a 2 cm crystal of higher gain was more suitable for the experiment. Despite this, the DCMs were still compatible for use with the 2 cm crystal in the generation of ultrashort pulses. The net intracavity GDDs of a resonator containing a 2 cm long Cr^{4+}:YAG crystal and various numbers of DCM reflections are plotted in Figure 4.4. The Cr^{4+}:YAG crystal contributes a GDD of 450 fs^2 and a TOD of 6000 fs^3 at 1500 nm. From Figure 4.4, the combination of a 2 cm long Cr^{4+}:YAG crystal and 6 DCM reflections seems to be the best choice for a dispersion-compensated KLM laser resonator.

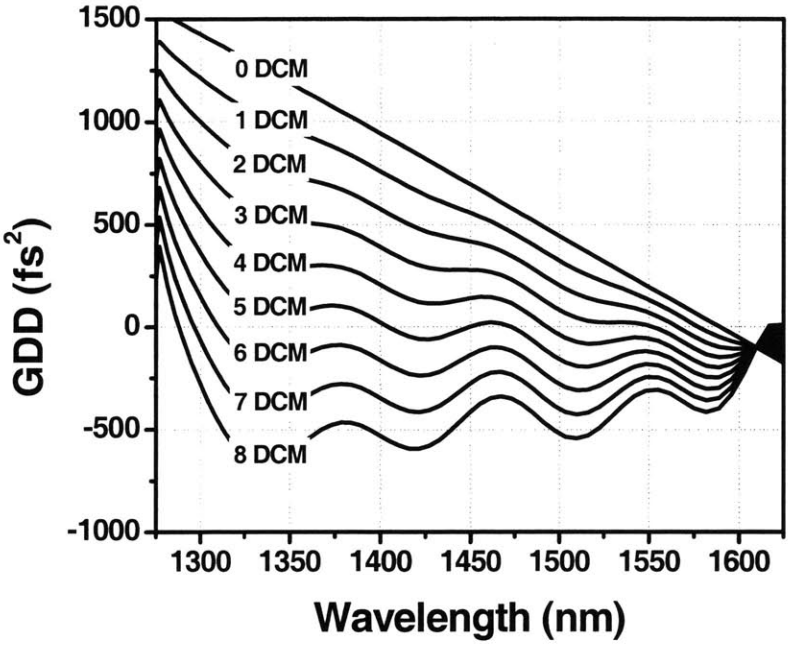

Figure 4.4 Net group delay dispersion of laser resonators containing a 2 cm Cr^{4+}:YAG laser crystal and varying number of double-chirped mirror reflections.

All of the plots shown in Figures 4.2 and 4.3 have been made under the assumption that light hits the DCMs at normal incidence. However, within the Z-fold laser cavity used in our experiment, some DCMs must be placed at angles, for the purposes of astigmatism compensation. Under these conditions, stronger oscillations in the GDD profile appear, due to the imperfect anti-reflection properties of the mirror. A plot of the GDD of the DCMs for several angles of incidence is shown in Figure 4.5. There is hardly any appreciable difference between the GDD for normal incidence and that for 5 degrees oblique incidence. However, at 16 degrees from normal incidence, which is the particular angle needed to compensate astigmatism in our resonator, the oscillations are quite significant. This poses a problem for modelocking, which requires a smooth continuous dispersion profile, so that all the colors in an ultrashort pulse experience the same group delay. Ideally, a revised mirror design accounting for specific angles of incidence would be desired; or, alternatively, a smaller astigmatism compensation angle would accomplish the same goal.

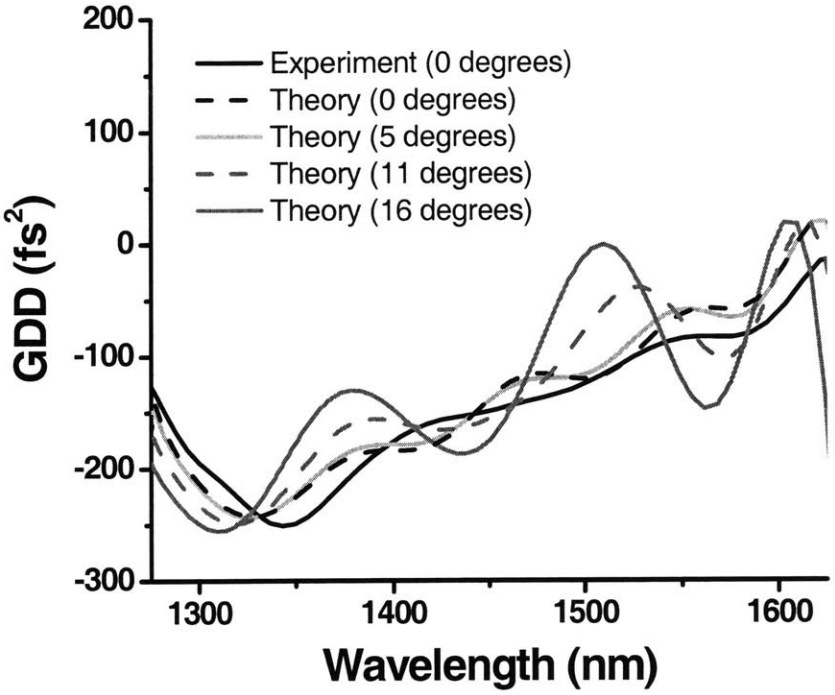

Figure 4.5 The group delay dispersion of double-chirped mirrors at various angles of incidence.

4.1.2 Astigmatism Compensation

When a material body is placed in the path of a ray and is tilted in the manner shown in Figure 4.6, one must account for the difference in optical path length that the two orthogonal directions of the transverse spatial profile travels. This effect is called astigmatism. Two planes of light are considered – the sagittal (*xz*) and the tangential (*yz*). The effect of astigmatism in a laser resonator is to separate the stability regions for these two planes, causing the beam to lose circular geometry, making the transverse mode elliptical. Because the alignment of Kerr lens modelocking is highly sensitive to the spatial beam profile in the cavity, astigmatism and compensation thereof are important factors in the design of a KLM laser.

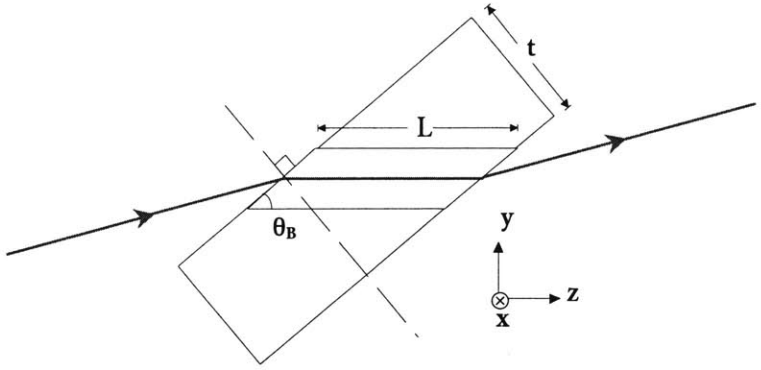

Figure 4.6 Brewster-angle cell geometry, with an inset of a Brewster-Brewster-cut laser rod. Coordinates and geometry used in the analysis below are shown.

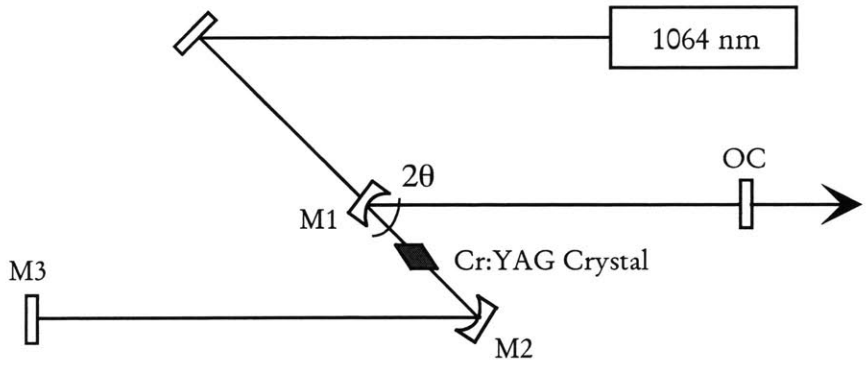

Figure 4.7 Schematic of a standard Z-fold laser resonator.

In a Z-fold cavity of the type shown in Figure 4.7, there are three optical elements that introduce astigmatic distortions, the two curved center mirrors *M1* and *M2* and the Brewster-Brewster-cut laser crystal. We analyze here the effect of astigmatism in these elements. The paraxial ray approximation can be used to characterize these elements and can also give us

their respective ray matrices, which can then be used to determine the properties of the resonator modes using the *ABCD* transfer matrix formalism [56].

Light reflecting off a curved mirror at oblique incidence focuses differently in the sagittal and tangential planes [20]. This results in two different effective focal lengths f_x and f_y, given by

$$f_s = \frac{f}{\cos\theta} \tag{4.1}$$

$$f_t = f\cos\theta \tag{4.2}$$

where f is the real focal length of the mirror and θ is the angle of incidence as shown in Figure 4.7. Similarly, a Brewster-cut cell also focuses sagittal and tangential ray bundles differently. This action can be expressed by two different effective distances d_x and d_y, through which the rays must traverse. Referring to the geometry shown in Figure 4.6, the effective distances are

$$d_s = \frac{\sqrt{n^2+1}}{n^2}\,t \tag{4.3}$$

$$d_t = \frac{\sqrt{n^2+1}}{n^4}\,t \tag{4.4}$$

where n is the index of refraction of the Brewster-cut material. However, the thickness of the cell t is not commonly used in the specification of a Brewster-Brewster-cut laser crystal; instead the physical path length L is quoted more often. From the geometry shown in Figure 4.6, we see that

$$\sin\theta_B = \frac{t}{L} \tag{4.5}$$

where the Brewster angle θ_B is given by

$$\tan\theta_B = n \tag{4.6}$$

Therefore, we can relate t to L by

$$t = \frac{n}{\sqrt{n^2+1}}\,L \tag{4.7}$$

Thankfully, for the resonator configuration shown in Figure 4.7, there is a common plane of incidence for both the center mirrors and the laser crystal, and the mirror astigmatism can counteract the Brewster cell astigmatism. Otherwise, astigmatic effects from all three elements add and compensation is impossible.

The purpose of astigmatic compensation is to create a circularly-symmetric transverse beam profile. Effectively, this is equivalent to maximizing the overlap of the sagittal and tangential stability ranges. The condition for this is [57]

$$d_s - d_t = 2\,(f_s - f_t) \tag{4.8}$$

or

$$\left(\frac{\sqrt{n^2+1}}{n^2} - \frac{\sqrt{n^2+1}}{n^4}\right) t = 2\left(\frac{f}{\cos\theta} - f\cos\theta\right) \tag{4.9}$$

$$\frac{n^2-1}{n^3} L = R\left(\frac{1}{\cos\theta} - \cos\theta\right)$$

where R is the radius-of-curvature (ROC) of the mirror and is equal to $2f$. We see that this expression is quadratic in $\cos\theta$. Solving this with the root formula, we get the astigmatism compensation angle θ_{ast}.

$$\theta_{ast} = \arccos\left(\frac{-b + \sqrt{b^2 + 4R^2}}{2R}\right) \tag{4.10}$$

where

$$b = \frac{n^2-1}{n^3} L \tag{4.11}$$

For a 2-cm-long Brewster-Brewster-cut laser crystal, the angle of incidence θ_{ast} on the two 10 cm ROC center mirrors must be 15.8 degrees in order to compensate astigmatism.

Using the Gaussian beam approximation (*ABCD* matrices), we can directly compute the stability regions of laser modes in the sagittal and tangential planes in the resonator described above in Figure 4.7, and verify the result above. Plots of the beam waist in the laser crystal for two different angles of incidence are shown in Figure 4.8 below. The sagittal and tangential stability regions are plotted (with the tangential beam waist artificially negative for ease of viewing). The x-axis is the separation distance between *M1* and *M2*. The resonator

dimensions used to make these plots are the same as those in our experiment, described in Section 4.1.4. In (a), the angle of incidence is 13 degrees; and, obviously, the overlap of the two stability regions has not been optimized. In (b), the angle of incidence is 15.8 degrees, as calculated above; and, indeed, the stability regions are well overlapped and astigmatism is compensated.

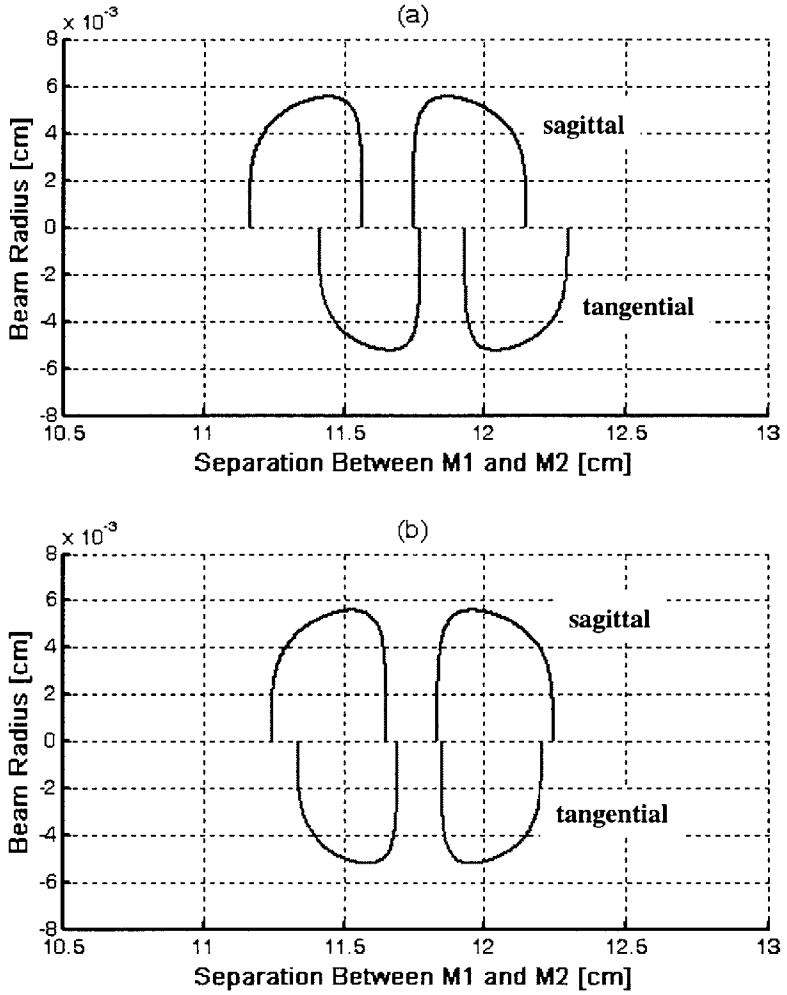

Figure 4.8 Schematic of astigmatism compensation. In (a), the angle of incidence is 13 degrees and astigmatism is not compensated. In (b), the angle of incidence is 15.8 degrees and maximum overlap of the stability regions is attained.

4.1.3 Water Absorption

Intracavity water vapor absorption is an extremely critical impediment to ultrashort pulse generation in the Cr^{4+}:YAG laser. Strong water absorption lines appear from 1300 to 1500 nm, coinciding with the Cr^{4+}:YAG gain spectrum. These lines are shown below in Figure 4.9. In addition to introducing costly intracavity loss, water impurities also give rise to abrupt variations in the intracavity dispersion map. In a femtosecond laser, the cavity dispersion not only needs to be compensated, but should also change smoothly in a broad wavelength range. A plot of the group delay dispersion introduced by water vapor in the air is shown below in Figure 4.10 [58]. Notice in this figure the scale of the GDD from water impurities; it is much larger in comparison to those from material dispersion, prism geometric dispersion, and the dispersion introduced by DCMs. The abrupt variation in dispersion will cause different wavelength components, which form a femtosecond pulse, to travel at different speeds. Therefore, the generation of femtosecond pulses is ultimately limited by the amount of smooth bandwidth available.

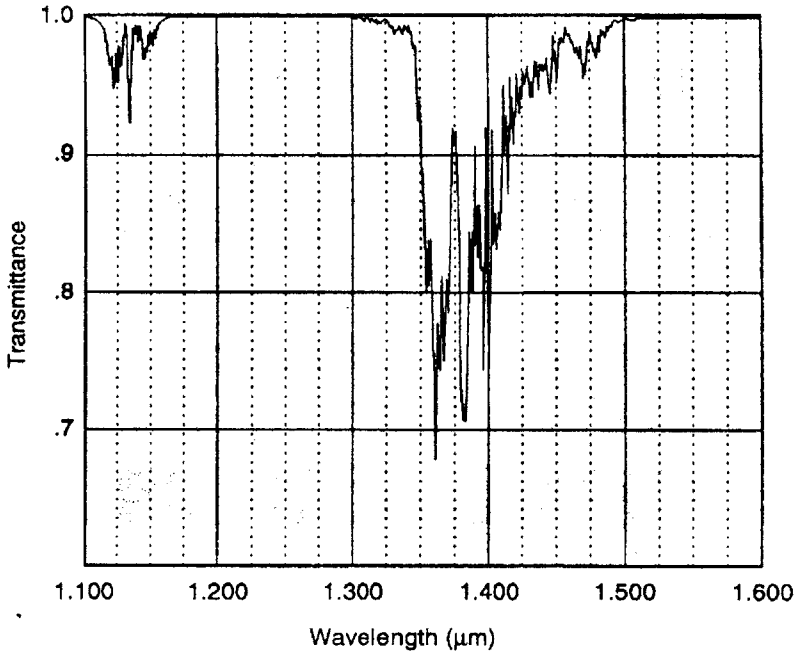

Figure 4.9 Transmission spectrum through air, exhibiting strong water vapor absorption from 1300 to 1500 nm. From Ref. [59].

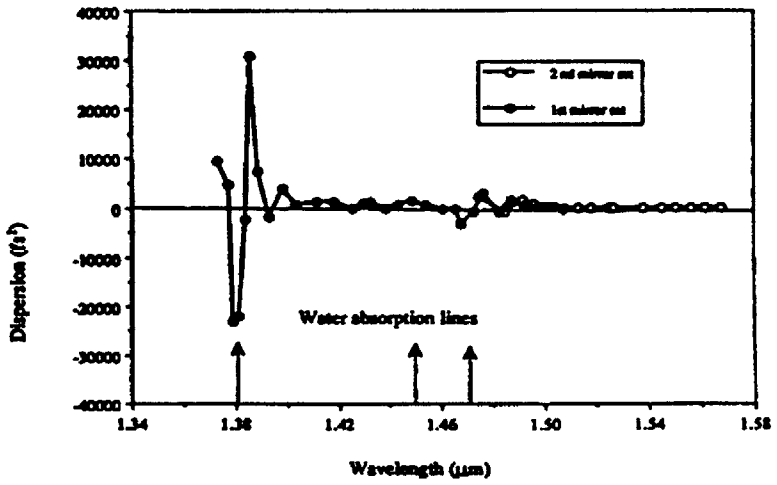

Figure 4.10 The group delay dispersion introduced by water vapor in air in a Cr^{4+}:YAG laser. From Ref. [58].

A large portion of the Cr^{4+}:YAG gain spectrum exists below 1500 nm. Therefore, in order to utilize the full gain spectrum, thereby providing the maximum spectral bandwidth to support ultrashort pulses, resonant water absorption lines from 1300 to 1500 nm must be removed. Even in a prismless resonator, there is a significant amount of water vapor, from the surrounding ambient air. Consequently, we must enclose the entire resonator and flush out the ambient air. A picture of our purging system is shown below in Figure 4.11. The resonator is enclosed in polycarbonate tubes and purged with dry nitrogen gas. Care must be taken so that the intracavity pulse does not experience any turbulence from the incoming nitrogen gas and does not get clipped by the enclosing plastic.

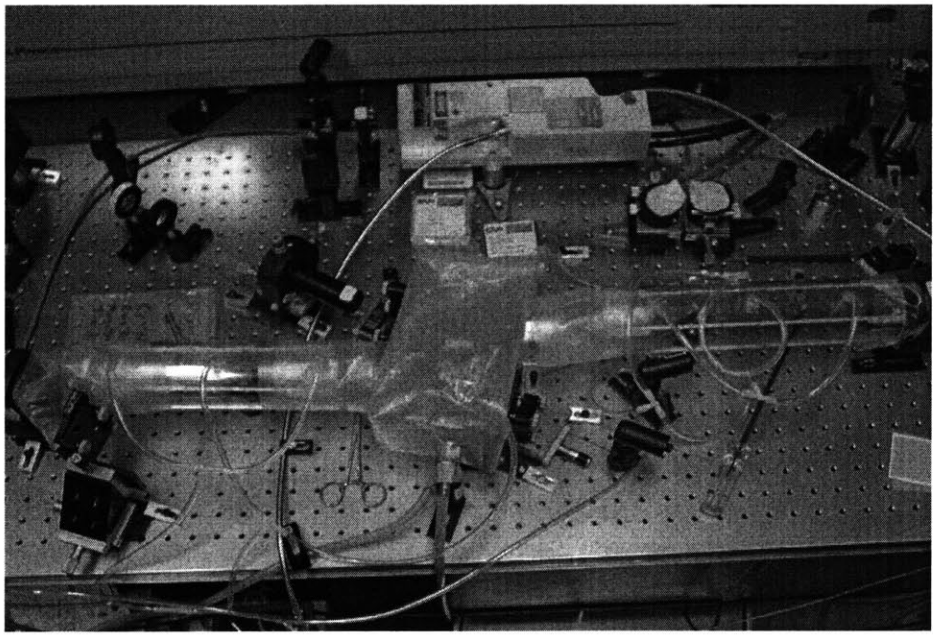

Figure 4.11 Image of the Cr^{4+}:YAG purging system, an essential requirement for removing deleterious water absorption effects.

To demonstrate the effect of intracavity loss due to water absorption, the Cr^{4+}:YAG laser, operating in cw mode, was tuned to 1405.6 nm, where there is strong water absorption. The resonator was then fully enclosed in plastic and the system was slowly purged with dry nitrogen over the course of 45 minutes. The output power of the cw laser was measured as a function of time and is plotted in Figure 4.12. Initially, with the resonator open to the ambient air, the cw output power of the Cr^{4+}:YAG laser was 2 mW; at the 45 minute mark, the power had increased to over 30 mW. Removing the intracavity loss due to water absorption greatly enhances the output power.

The effect of purging the system on the output spectrum of a modelocked laser was also investigated. In a resonator exposed to air, modelocking was initiated by a saturable Bragg reflector, which will be discussed in Section 4.2. A plot of the purged and unpurged spectrum of a saturable absorber modelocked Cr^{4+}:YAG laser is shown in Figure 4.13. Generally, without purging, the modelocked spectrum is quite unstable and "jagged". However, after purging the resonator for a time and removing the water vapor, the spectrum stabilizes and becomes more smooth and uniform.

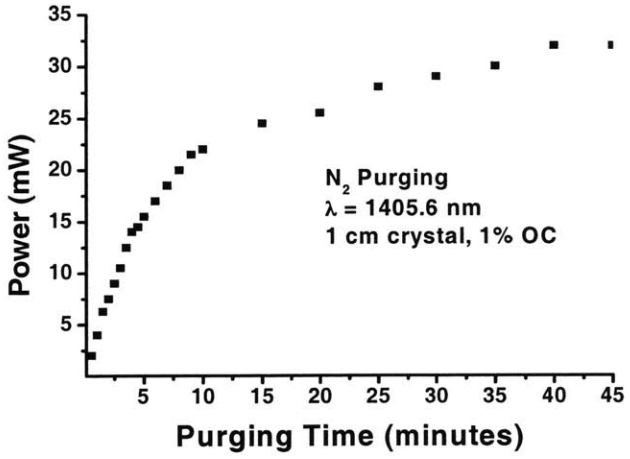

Figure 4.12 The effect of purging the resonator. Output power increases as a function of time, when the resonator is initially un-purged. From Ref. [16].

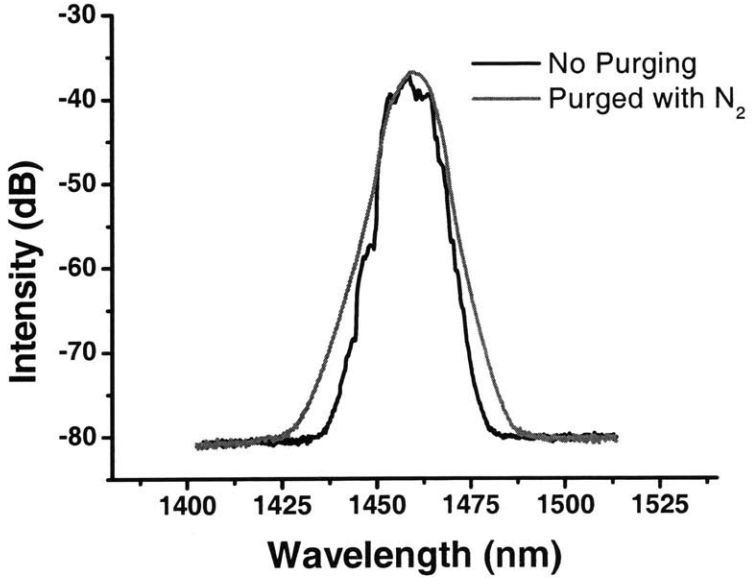

Figure 4.13 The effect of purging the resonator on the modelocked spectrum. After purging, the spectrum becomes more uniform and smooth. From Ref. [16].

4.1.4 Laser Resonator Configuration

A Z-fold cavity, similar to the one shown previously in Figure 4.7, was chosen for its relative ease of alignment and tight focusing in the laser crystal, essential for Kerr lens modelocking. The fact that the resonator relies only on double-chirped mirrors for dispersion compensation, not prisms, also simplifies the alignment. The reason behind the prismless resonator is that, at the time, there was a lack of available prism materials with both low water content and the proper dispersion characteristics. Therefore, a prismless laser cavity with dispersion compensating DCMs was the best option.

The stability and performance of a Z-fold resonator can be studied using the *ABCD* transfer matrix formalism [56]. By assigning a matrix to each optical element in the resonator, we can trace the entire transverse spatial profile of the intracavity beam, as well as study the effect of various parameters on the beam waist. A thorough discussion of the *ABCD* matrices will not be given here, only the results of the computation. The former can be found in Ref. [60]. The stability ranges of a symmetric and asymmetric laser resonator are shown below in Figure 4.17. The stability range is defined as those resonator dimensions that can produce a finite beam waist; and a symmetric resonator is one in which the two arms on either side of the laser crystal exactly mirror each other. The plots give the beam waist in the laser crystal as a function of the separation distance d between *M1* and *M2*. As you can see, there is only one stability region for a symmetric resonator, and two for an asymmetric resonator.

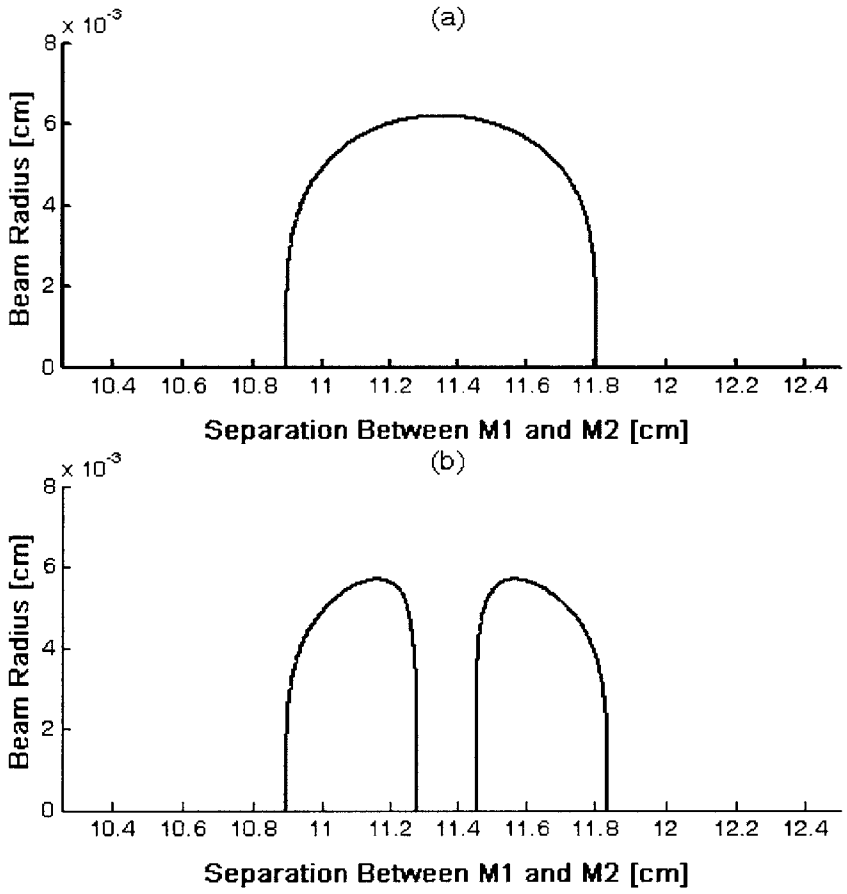

Figure 4.14 The stability regions of (a) symmetric and (b) asymmetric resonators.

Optimum resonator design for either hard- or soft-apertured KLM can be found by calculation of the mode size at the aperture or at the pump beam waist in the gain medium. The goal is to design the laser resonator in such a way that self-amplitude modulation action is optimized. This can be quantified by a merit function η, which measures the fractional change in beam waist with intracavity power variation.

$$\eta = \frac{1}{w}\frac{dw}{dP} \tag{4.12}$$

where w is the beam waist and P is the intracavity power. Obviously, η must be negative in order to achieve self-amplitude modulation. Effectively, η is a measure of the strength of the

SAM; and it can be entirely determined from the resonator parameters using the *ABCD* matrix formalism. Through an optimized resonator design, Cerullo *et al.* [57] demonstrated that η could be maximized such that the intensity fluctuations of a cw laser could initiate Kerr lens modelocking. The maximum absolute value of η is given by

$$|\eta|_{max} = \frac{1}{4[AD(1-AD)]^{1/2}} \tag{4.13}$$

where A and D are the *ABCD* matrix elements of the effective roundtrip propagation through the resonator. For a stable resonator, one can easily show that

$$0 < AD < 1 \tag{4.14}$$

Therefore, $|\eta|_{max}$ can grow to infinity at the edges of the stability regions, and it is there that KLM can be initiated most readily.

Indeed, this is what we observe in the laboratory. We find that KLM can be initiated in asymmetric resonators much more readily than in symmetric ones; and it is at the longer inner edge of the stability regions in the asymmetric resonators that KLM is most strong. We clarify the meaning of "longer inner edge of the stability region" below. Modelocking is also observed at the shorter outer edge of the stability regions, however, this is typically weaker and longer pulses are generated, in comparison to the former.

In order to understand these results, we study our experimental observations with a numerical simulation program using *ABCD* matrices to model the resonator. Plots of the stability ranges for low intensity and high intensity light are shown in Figure 4.15. In our program, we model the gain (Kerr) medium as a power-dependent lens, with varying focal lengths for different intracavity powers. The higher the intracavity power, the shorter the focal length, according to the Kerr effect. As Cerullo had predicted, η is largest at the edges of the stability regions. However, only at two out of the four edges, is η negative, which is the requirement for SAM. It is at what we have termed the "shorter outer edge" and the "longer inner edge" of the stability regions that SAM, and hence modelocking, can be achieved. These regions have been circled in Figure 4.15. The longer inner edge is where the strongest KLM action can be found.

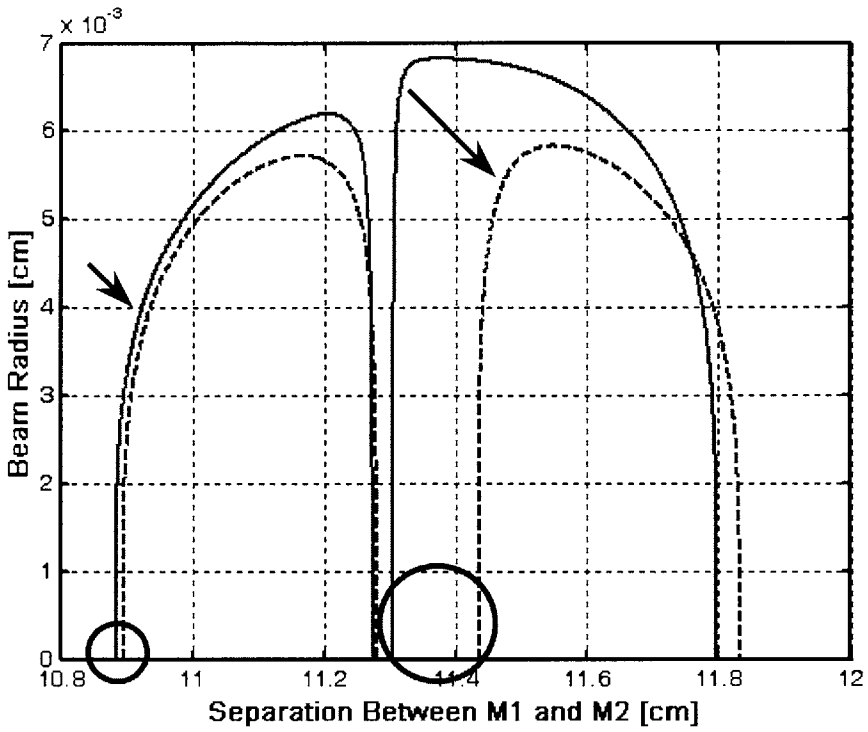

Figure 4.15 The effect of a Kerr lens in the resonator. At certain resonator positions, higher intracavity intensities lead to smaller beam waists.

4.1.5 Experimental Results

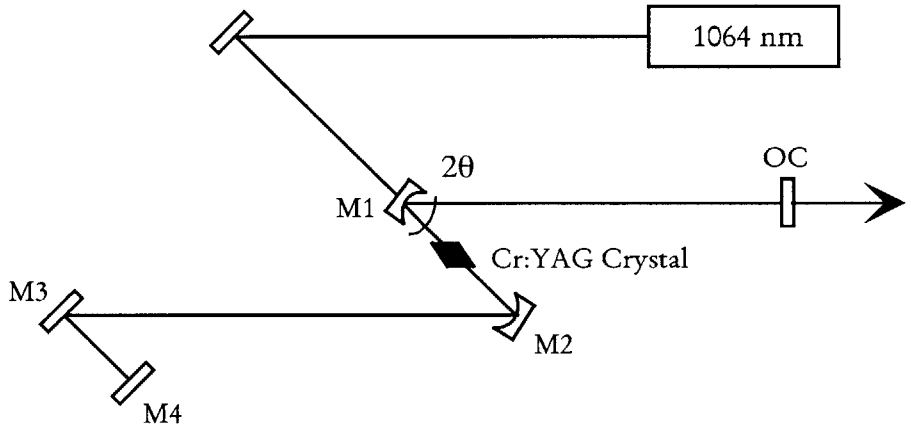

Figure 4.16 Schematic of the prismless Cr^{4+}:YAG laser resonator.

A schematic of the prismless Cr^{4+}:YAG laser resonator is shown in Figure 4.16. The Brewster-Brewster-cut Cr^{4+}:YAG rod, supplied by A. V. Shestakov of E.L.S company, has dimensions of 2 cm in length and 3 mm in diameter, and is pumped at 1064 nm by a Spectra-Physics 11 W Nd:YVO_4 laser. The pump beam is focused into the crystal through a 10 cm focal length lens. The laser crystal has a linear absorption of 1.5 cm^{-1} and is cooled to 13 °C during operation. Approximately 5 cm from both sides of the laser crystal are 10 cm radius-of-curvature (ROC) double-chirped mirrors, *M1* and *M2*, rotated 15.8 degrees from normal incidence to compensate for the astigmatism introduced by the Brewster-Brewster-cut laser crystal. One arm of the resonator is 70 cm long, containing both a flat DCM (*M3*) and an unchirped quarter-wave-stack high reflector (*M4*). And the other arm, about 50 cm in length, contains a broadband output coupler (*OC*), with a peak transmission of 0.7 % at 1515 nm and <1.4 % from 1420 to 1630 nm. The measured reflectivities of the high reflector *M4* and output coupler *OC* are shown in Figure 4.17.

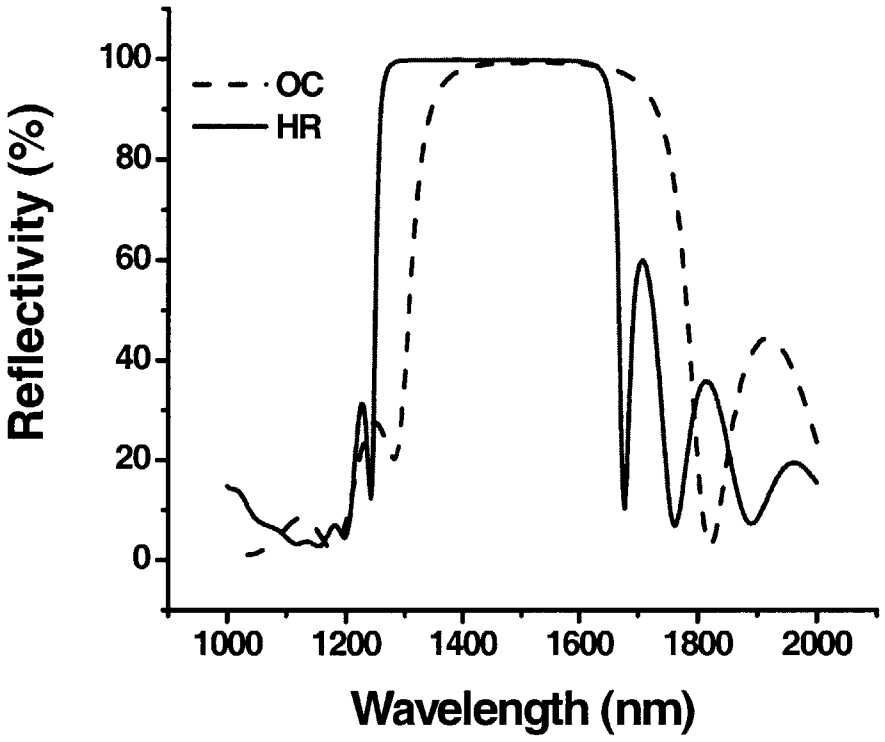

Figure 4.17 Measured reflectivities of the high reflector *M4* and the output coupler *OC*.

In our experiment, we use the 2-cm-long gain crystal in a standing wave laser configuration; therefore, over the course of a cavity roundtrip, the pulse effectively traverses 4 cm of Cr^{4+}:YAG material. In order to compensate for the positive chromatic dispersion introduced by the Cr^{4+}:YAG, we must use 6 DCM reflections per cavity roundtrip to supply the necessary negative dispersion, as discussed earlier. This is summarized again in Figure 4.18. As mentioned before, we have not taken into account the discreet ordering of intracavity elements in our resonator design, as required for dispersion-managed modelocking; we considered only the net sum of the GDD of all the elements. However, modeling such effects is necessary to achieve optimum performance, and it will be done in the future. The major contributors to the dispersion map in the laser cavity are the DCMs and the Cr^{4+}:YAG; we also take into account the air in the beam path, as well as the dispersion of non-DCM mirrors.

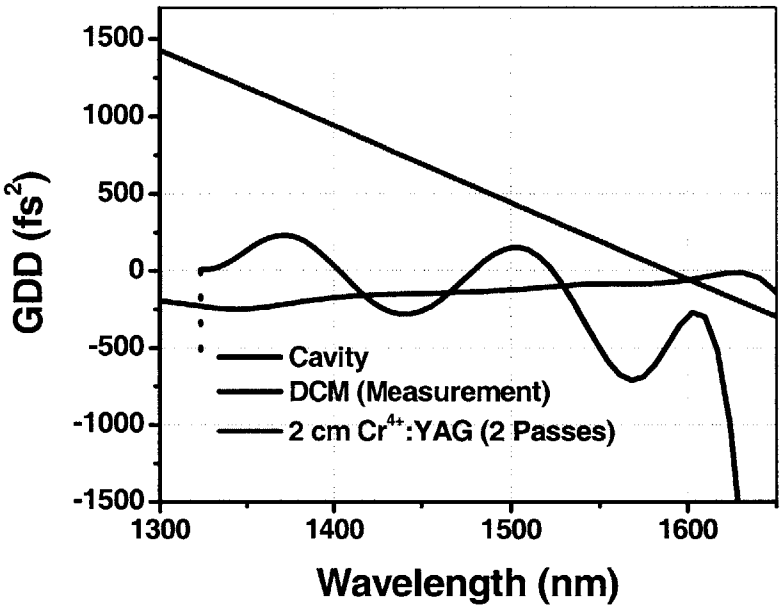

Figure 4.18 Group delay dispersion of two passes through a Cr^{4+}:YAG crystal, one double-chirped mirror reflection, and the net sum of all optical elements in the laser resonator.

Finally, the whole of the resonator is enclosed in plastic tubes and purged with dry nitrogen gas to prevent water absorption.

The laser is initially aligned for cw operation and the output power is optimized. The lasing threshold power was 0.7 W of absorbed pump, and the cw output power was 1 W with 9 W of absorbed pump. After optimizing the output power, the resonator is then adjusted to the approximate positions shown in Figure 4.15 by observing the variation in output power. The most relevant resonator parameters adjusted are the folding mirror separation distance between *M1* and *M2* and the laser crystal position between those folding mirrors. KLM is initiated by a slight tilting or light tapping of the end mirrors. However, this process is much easier said than done. For one, the growth process of Cr^{4+}:YAG crystals has yet to be perfected; consequently, the crystal composition is fairly inhomogeneous. The result is that performance varies, in some cases quite drastically, depending on the position of the pump laser beam in the gain crystal. When adjusting the resonator for KLM, we need to raster scan across the face of the Cr^{4+}:YAG crystal in order to maximize the intracavity power. Secondly, and perhaps most importantly, KLM requires critical alignment of the laser cavity. Small adjustments can affect quite considerable changes in performance. When tapping end

mirrors is required to initiate modelocking, it is especially difficult and frustrating to find a resonator configuration that can support stable KLM operation.

The average power of the modelocked pulse was 200 to 400 mW, depending on the resonator alignment, for 9 W of absorbed pump. An example of the modelocked pulse spectrum, measured by a calibrated optical spectrum analyzer (OSA), is shown in Figure 4.19. The spectrum peaks at 1450 nm and has a FWHM of 190 nm, from 1310 to 1500 nm. Significant spectrum is visible on the log scale from 1140 nm to >1700 nm, which is the long wavelength limit of our OSA. It also exhibits a relatively flat top from 1340 to 1470 nm. The shorter wavelengths in the spectrum are enhanced by light leaking out of the output coupler, which rolls off considerably at wavelengths below 1350 nm. We believe that because this light is not part of the main pulse bouncing back and forth inside the resonator, it is not experiencing as much self-amplitude modulation. This translates into less modelocking action and lower phase correlation with the main pulse. It is possible that this low-wavelength bandwidth may not be contributing effectively to the production of short pulse durations. Long wavelength spikes seen in the spectrum can be attributed to Raman-amplified Kelly sidebands and have been previously reported [62].

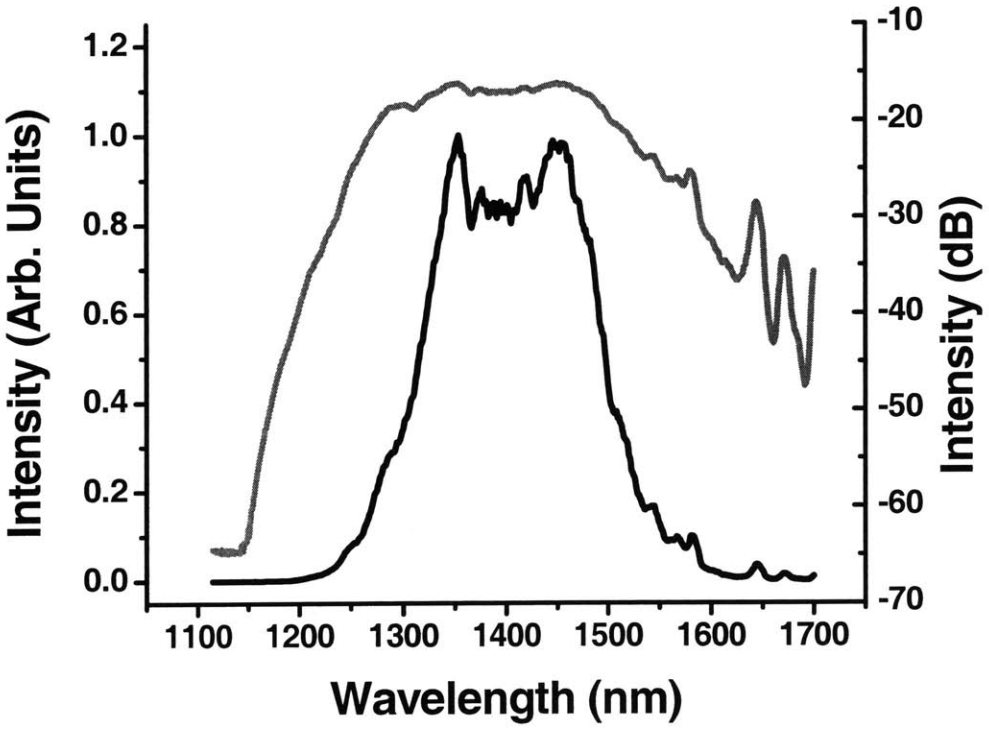

Figure 4.19 Modelocked pulse spectrum from the Cr^{4+}:YAG, in log (gray) and linear (black) scales. The full-width at half maximum is 190 nm, with a peak at 1450 nm.

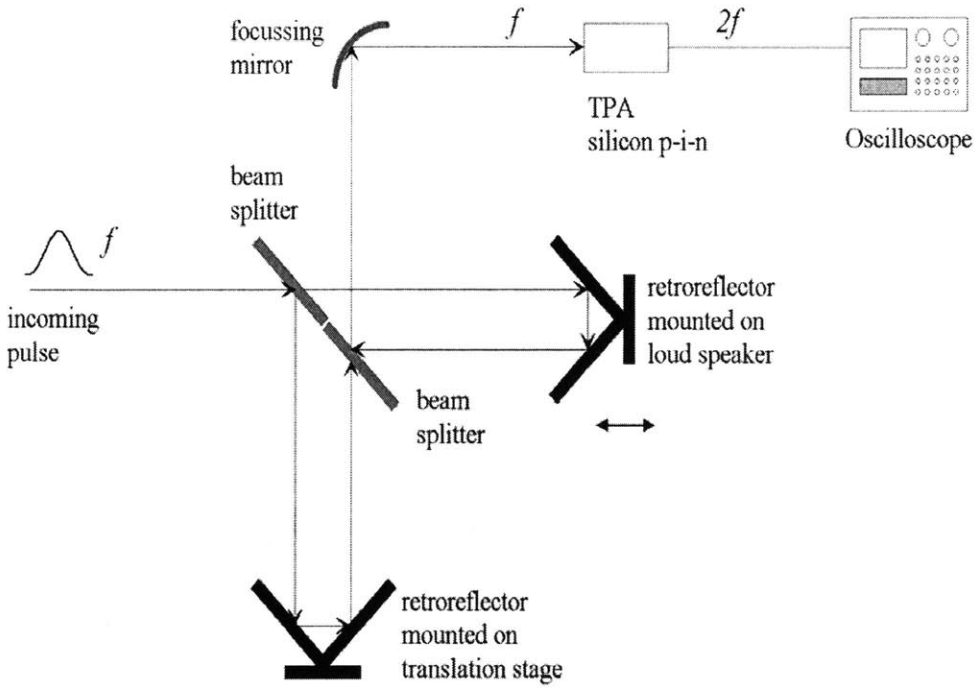

Figure 4.20 Schematic of the interferometric autocorrelator based on two-photon absorption used in our experiment.

The pulse duration was measured by fringe-resolved, or interferometric, autocorrelation. The experimental setup is shown in Figure 4.20. The beam was split and recombined by broadband metallic beamsplitters and focused by an off-axis parabolic mirror onto a silicon p-i-n photodiode, where the autocorrelation function $g_2(\tau)$ was measured by two-photon absorption. An autocorrelation trace is shown in Figure 4.21. The abscissa was calibrated by the interference fringes of a HeNe laser, as described in Chapter 2. Several pulse shapes were used to determine the best fit. The pulse duration was estimated to be 18.3 fs for sech-shaped pulses and 17.0 fs for Gaussian pulses. A Fourier transform of the optical spectrum, assuming a flat phase profile, yields a transform-limited duration of 17.5 fs. In addition, a pulse-retrieval algorithm, provided to us by Uwe Morgner, was used to reconstruct the pulse profile from the measured interferometric autocorrelation and spectrum [63]. The algorithm guesses an initial phase profile; and by matching it with the measured spectrum, generates a temporal pulse shape. The autocorrelation trace is then calculated for this pulse shape and compared to the measured trace. Depending on this comparison, the phase profile is then adjusted, and the whole process is iterated until the calculated autocorrelation trace matches the measured. The

retrieved pulse shape has a duration of 19.5 fs.

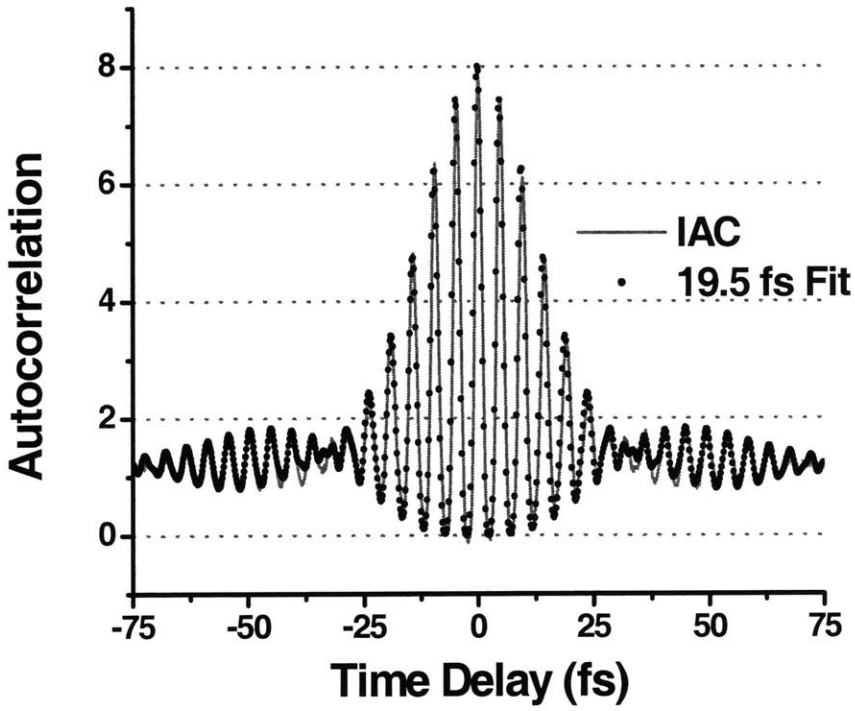

Figure 4.21 Measured autocorrelation from an interferometric two-photon absorption autocorrelator (line) and fit by a pulse-retrieval algorithm (dots). A pulse duration of 18.3 fs is calculated by assuming a sech-shaped pulse, 17.0 fs by assuming Gaussian-shaped pulses, and 19.5 fs by the pulse-retrieval algorithm.

Upon leaving the resonator, the pulse passes through several optical elements before reaching the autocorrelator. The additional chirp from the dispersion of these extracavity elements was compensated by the insertion of two BaF_2 prisms and one DCM reflection. As described in Chapter 2, the interferometric autocorrelation trace can readily reveal the existence of chirp in the pulse. For pulses with large chirps, the wings of the autocorrelation trace appear to slope upwards towards the center of the pulse. By reducing the chirp, one also reduces the pulse width. The BaF_2 prisms supply variable material dispersion. Examples of interferometric autocorrelation traces for different BaF_2 prism insertions are shown in Figure 4.22. Without any extracavity dispersion compensation, the pulse duration was 20.5 fs. With compensation, a minimum pulse duration of 18.3 fs was measured, with 9 mm of BaF_2 material inserted in the beam path. This corresponds to a GDD of 127 fs^2 at 1500 nm.

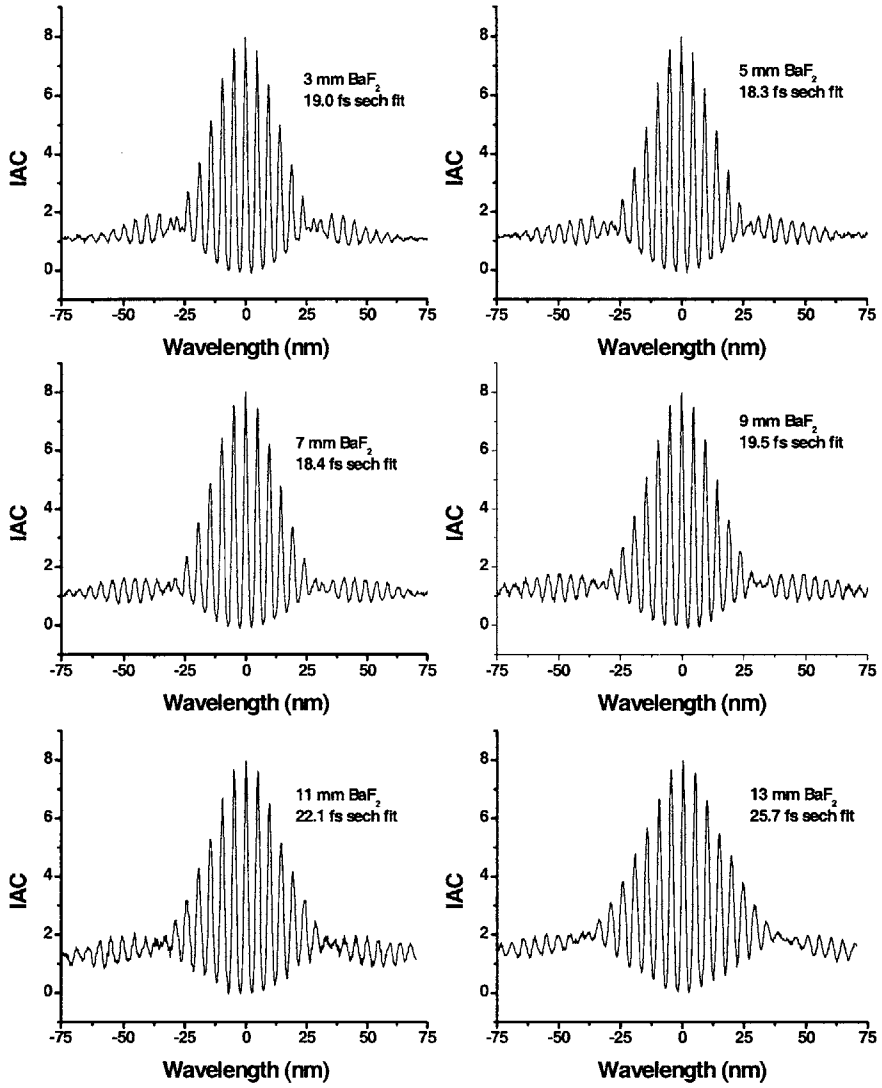

Figure 4.22 Interferometric autocorrelations taken with different amounts of extracavity BaF_2 dispersion compensation. As the pulse chirp becomes compensated, the wings of the autocorrelation become flat.

4.2 THE SELF-STARTING Cr^{4+}:YAG LASER WITH BROADBAND SBR

Operational simplicity is essential for real-world applications of modelocked lasers. An ultrafast laser needs to be able to self-start modelocking and pulsed operation must be stable. The prismless Cr^{4+}:YAG laser described in the previous section relies on Kerr lens modelocking alone and is typically not self-starting. Modelocking must be initiated by tapping the end mirrors, which is inconvenient. Saturable Bragg reflectors (SBRs) can solve this problem. By using an SBR to self-start modelocking, the simultaneous actions of tapping an end mirror and adjusting resonator parameters to find KLM are no longer required. If the laser is already modelocked with a picosecond seed pulse, one can search for KLM by only changing the resonator dimensions. This greatly simplifies alignment of the laser for KLM operation.

In Cr^{4+}:YAG lasers, modelocking has been achieved with semiconductor saturable absorber mirrors consisting of InGaAs/InP, InGaAs/GaAs, and InGaAs/InAlAs quantum wells absorbing near 1550 nm grown upon a highly-reflecting mirror [64,65,66]. In each case, GaAs/AlAs Bragg stacks were used as the mirror substrates and the mirrors had a maximum useful bandwidth of ~150 nm. Since this is less than the spectral range of the Cr^{4+}:YAG gain, the generation of ultrashort pulses was obviously limited. Zhang *et al.* overcame this difficulty by using an InGaAs/InAlAs quantum well absorber bonded onto a broadband gold mirror and was able to generate pulse durations of 44 fs from a self-starting Kerr lens modelocked Cr^{4+}:YAG laser [67,68]. Because the intrinsic loss of the gold mirrors was too large for the loss-sensitive Cr^{4+}:YAG laser, the gold mirror reflectivity was enhanced by adding three layers of $SiO_2/TiO_2/SiO_2$. Higher-order dispersion, rather than the SBR bandwidth, was believed to be the limiting factor in generating the shortest possible pulse. For the work presented here, double-chirped mirrors were used for broadband higher-order dispersion compensation, and a saturable absorber structure made of InGaAs/InP quantum wells grown on top of a $GaAs/Al_xO_y$ Bragg mirror was used to initiate modelocking. Pulses as short as 35 fs were generated directly from a prismless Cr^{4+}:YAG.

4.2.1 The Broadband Saturable Bragg Reflector

The basic structure of a saturable Bragg reflector consists of a saturable absorber element, in this case an InGaAs/InP quantum well, epitaxially grown on top of a broadband high-reflectance dielectric Bragg mirror. A schematic of the SBR used for this work is shown in Figure 4.23, along with the standing wave pattern of the electric field. The SBR structure consists of 7 pairs of $GaAs/Al_xO_y$ layers, with each dielectric layer designed for a Bragg wavelength of 1440 nm. The saturable absorber, an InGaAs/InP quantum well, is made of a

10 nm $In_{0.52}Ga_{0.48}As$ layer centered in a $\lambda/2$-thick InP layer. The InGaAs layer, effectively the quantum well, is placed at a maximum of the electric field profile in order to increase the local energy density.

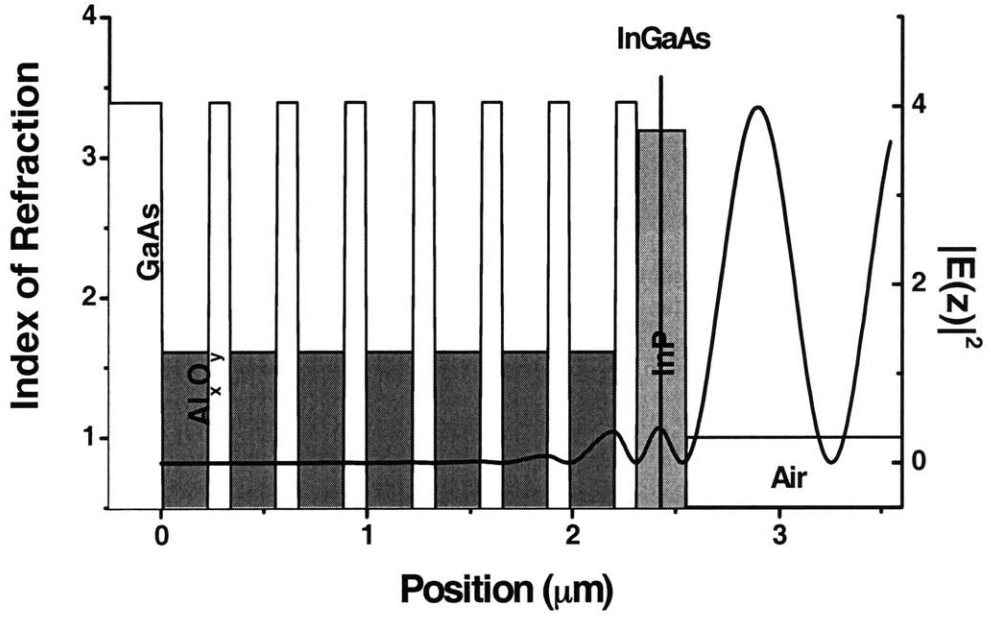

Figure 4.23 Schematic of the saturable Bragg absorber structure used in the Cr^{4+}:YAG, consisting of a GaAs/AlxOy high-index-contrast mirror and an InGaAs/InP quantum well.

This SBR was grown using III-V semiconductor growth techniques [69,70,71]. Growth and oxidation of these structures were done by Alexei Erchak [72]. First, the InGaAs/InP quantum well is grown on top of a GaAs/AlAs dielectric stack using gas-source molecular beam epitaxy (GSMBE). Following growth of the entire structure, the SBR is placed in a wet oxidation furnace at 400 C, where the AlAs layers are converted to Al_xO_y. The final layers are designed to be a quarter-wave stack at 1440 nm. Side-view scanning electron microscope images of an unoxidized and oxidized SBR structure are shown in Figure 4.24. Sometimes, not all the layers in the SBR oxidize, resulting in non-uniform performance over the entire "usable" mirror surface. An example of this is shown in Figure 4.25.

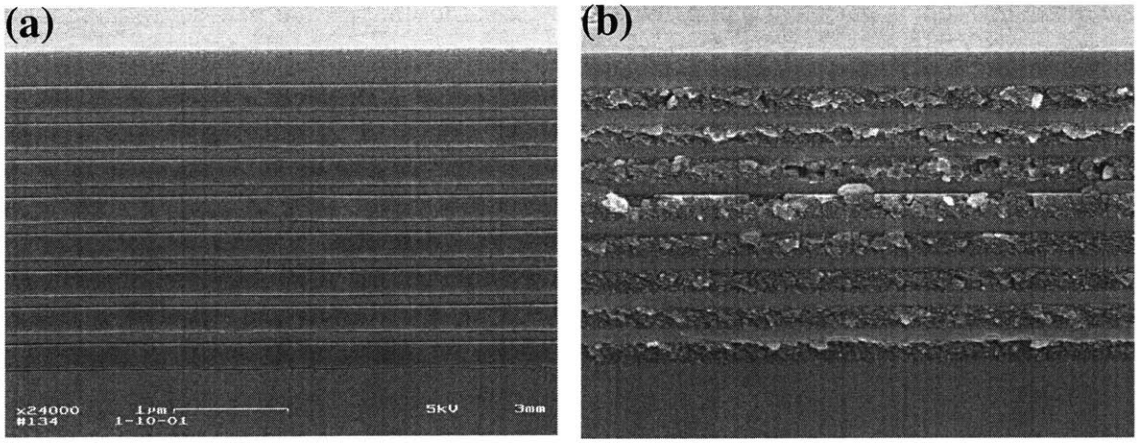

Figure 4.24 Side-view scanning electron microscope image of an (a) unoxidized and (b) oxidized saturable Bragg reflector structure. The polycrystalline Al_xO_y appear granular in comparison with the AlAs, after oxidation.

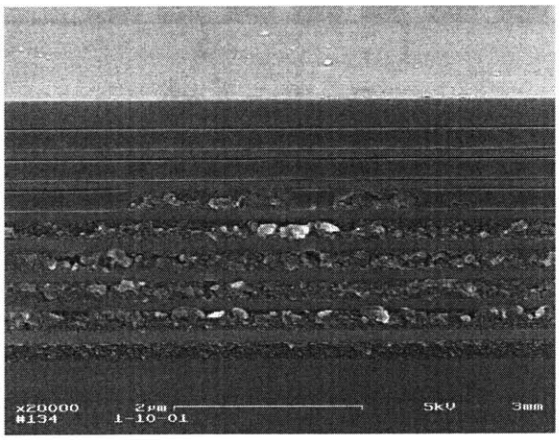

Figure 4.25 Scanning electron microscope image of a saturable Bragg reflector that has oxidized halfway.

Because the oxidation process converts high-index AlAs to low-index Al_xO_y laterally from the edge of the structure, only material near an exposed edge will oxidize. After 9.5 hours of oxidation, SBRs with Al_xO_y layers of width ~200 μm on a side are produced. This is illustrated in Figure 4.26. As a result, only a relatively small fraction of the SBR sample is usable in the Cr^{4+}:YAG laser resonator. Unoxidized regions have far too much loss to allow modelocking.

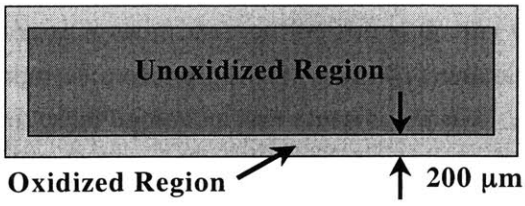

Figure 4.26 Top-view of the saturable Bragg reflector illustrating the usable oxidized surface on the mirror.

The dielectric mirror consists of GaAs and Al_xO_y layers, with refractive indices of 3.39 and 1.61 at 1.5 μm, respectively. This high index contrast makes it possible to design mirrors with broadband reflectivity of >99.5% from 1200 to 1800 nm with only 7 pairs of GaAs and Al_xO_y layers. In contrast, previous mirrors grown for use in Cr^{4+}:YAG lasers used GaAs and AlAs layers, typically with 30 pairs. The index of refraction of AlAs is 2.87. The comparatively lower index contrast results in a much smaller useful spectral range; the reflectivity of GaAs/AlAs mirrors is >99.5% from 1400 to 1550 nm. This disparity in high-reflectance bandwidth is demonstrated in Figure 4.27, with GaAs/Al_xO_y and GaAs/AlAs mirrors. The high index contrast of the GaAs/Al_xO_y system offers the additional advantages of a smaller number of periods, short epitaxial growth times, and a relaxed requirement on the thickness control. Even a ±10% thickness error can be tolerated with the bandwidth of the mirror still covering the entire Cr^{4+}:YAG gain spectrum [72].

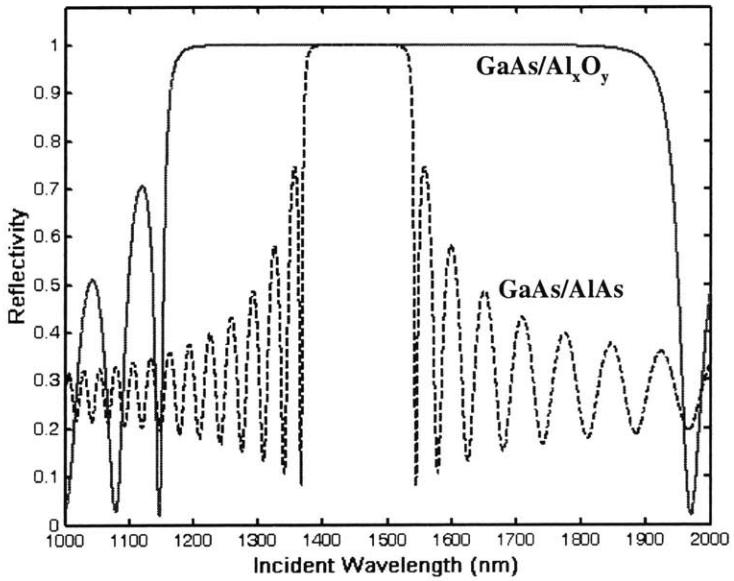

Figure 4.27 Reflectivity comparison of a 7-pair GaAs/Al_xO_y mirror and a 30-pair GaAs/AlAs mirror.

The reflectivity of the SBR structure was measured together with Juliet Gopinath using Fourier transform infrared spectroscopy (FTIR), and is shown in Figure 4.28. The SBR has a stopband from 1300 to 1800 nm. It is difficult to determine an exact reflectivity value from FTIR due to the small sample size (200 μm width), therefore an indirect method using laser threshold values is necessary. We will discuss this technique later. In addition, we have also calculated the group delay dispersion of the 7-pair GaAs/Al_xO_y mirror, and it is shown in Figure 4.29. The GDD is close to zero from 1200 to 1800 nm, coinciding with the high-reflectance range of the SBR, and therefore should not change the resonator dispersion significantly. Because of this, high-index-contrast dielectric mirrors could be ideal candidates for use in ultrafast lasers as unchirped high reflectors or broadband output couplers.

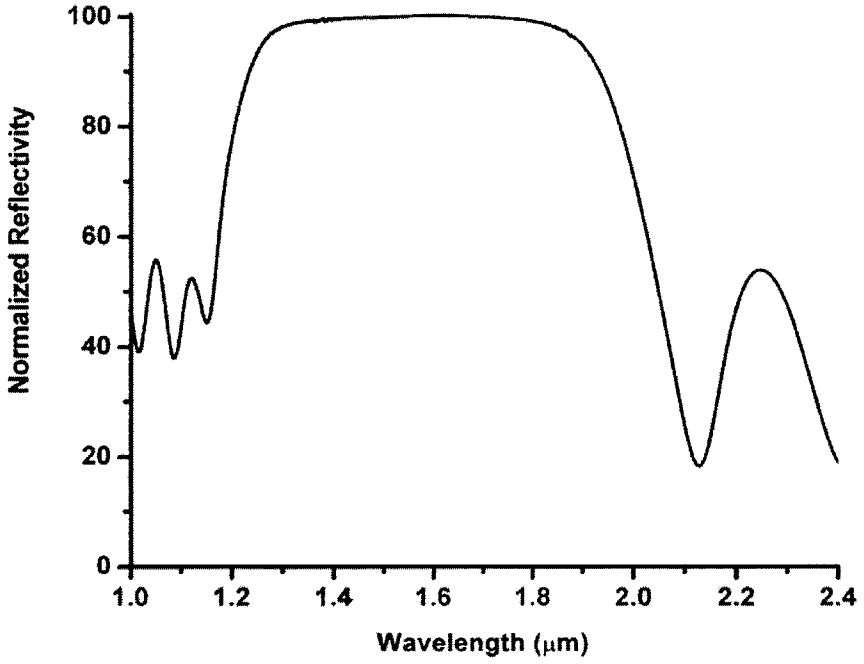

Figure 4.28 Measured reflectivity of the saturable Bragg reflector using Fourier transform infrared spectroscopy.

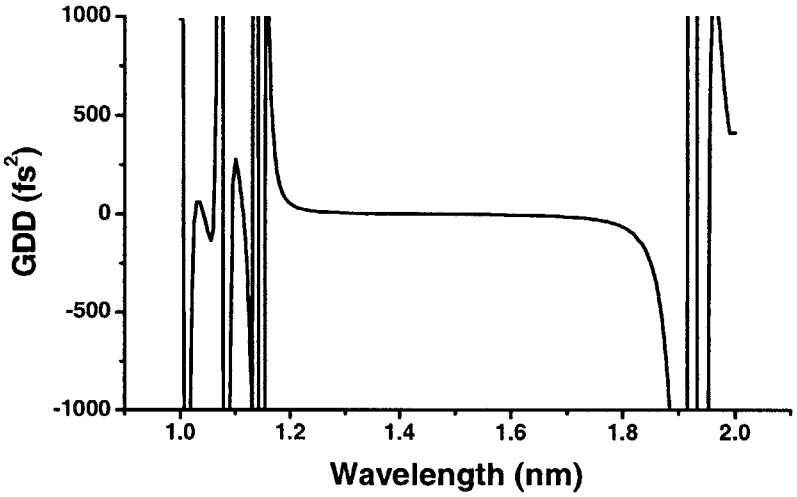

Figure 4.29 Calculated group delay dispersion of a high-index contrast dielectric mirror consisting of a 7 pair GaAs/Al_xO_y quarter-wave stack.

Photoluminescence (PL) was used to observe emission from the InGaAs/InP quantum well, and is shown in Figure 4.30. An argon ion laser excites the SBR at 488 nm and PL is then collected with lenses and measured with a spectrophotometer. The PL is centered at 1540 nm and has a FWHM of 110 nm. The center wavelength is slightly lower than designed, so the SBR may be unable to initiate modelocking for wavelengths below the band gap energy.

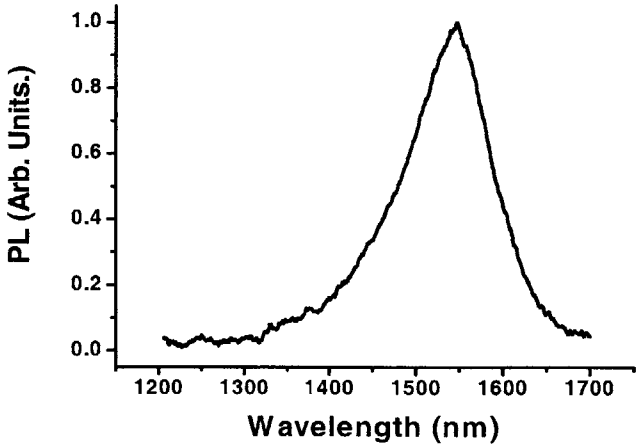

Figure 4.30 Measured photoluminescence from the broadband saturable Bragg reflector.

To measure the saturation response of the SBR, time-resolved spectroscopy, or pump-probe, was used. Pump-probe experiments can measure the change in reflectivity of the SBR due to saturation, as well as the relaxation time scales of the system. The pump-probe technique uses one pulse (pump) to excite the system; after which, the response of the system is investigated with a second pulse (probe) of considerably less power such that its presence does not alter the system. The system, however, does change the probe pulse, which is then what is measured to evaluate the response of the system to the pump pulse. The pump-probe technique reveals time-dependent responses of the system with a temporal resolution equal to the cross-correlation width of the pump and probe pulses. A schematic of the pump-probe experiment is shown in Figure 4.31. The SBR saturation characteristics at 1540 nm were studied using 150 fs pulses from an optical parametric oscillator by Juliet Gopinath.

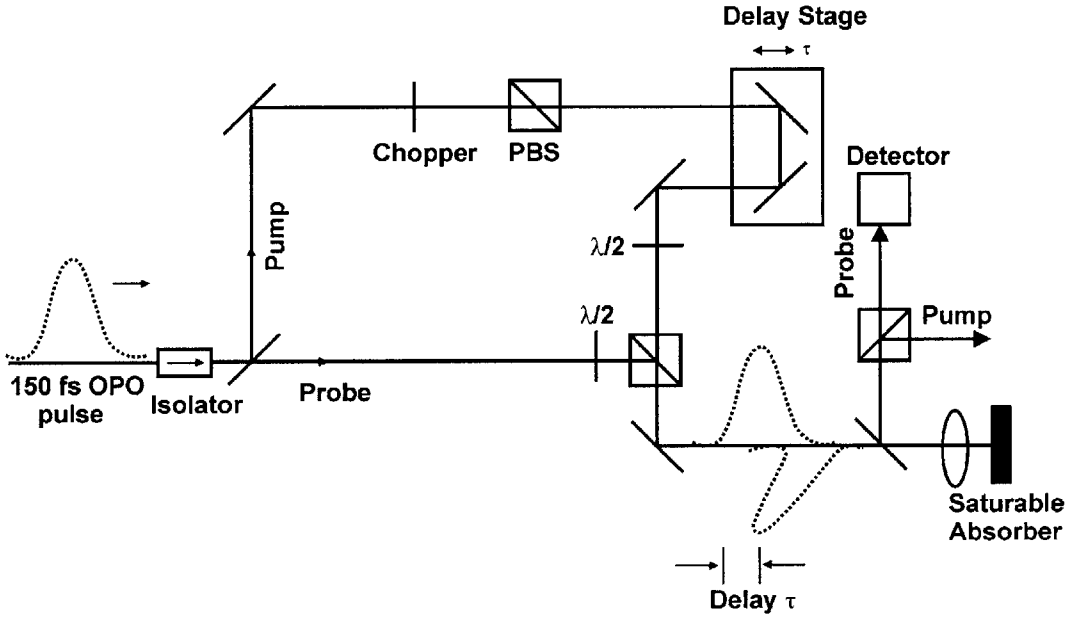

Figure 4.31 Schematic of the pump-probe setup used to study the saturation dynamics of the saturable Bragg reflector [47].

Several pump-probe measurements for varying pump powers are shown in Figure 4.32. At low fluences, the SBR response shows a fast saturation due to intraband thermalization and a long recovery time of about 40 ps due to recombination. The saturation fluence is estimated to be on the order of ~10 $\mu J/cm^2$, and the maximum saturable loss is 0.3%. As the pump fluence is increased, significant two-photon absorption increases the total loss of the SBR, making it an inverse saturable absorber. At high peak intensities, the loss from TPA limits the power of the laser pulses and may adversely affect KLM action.

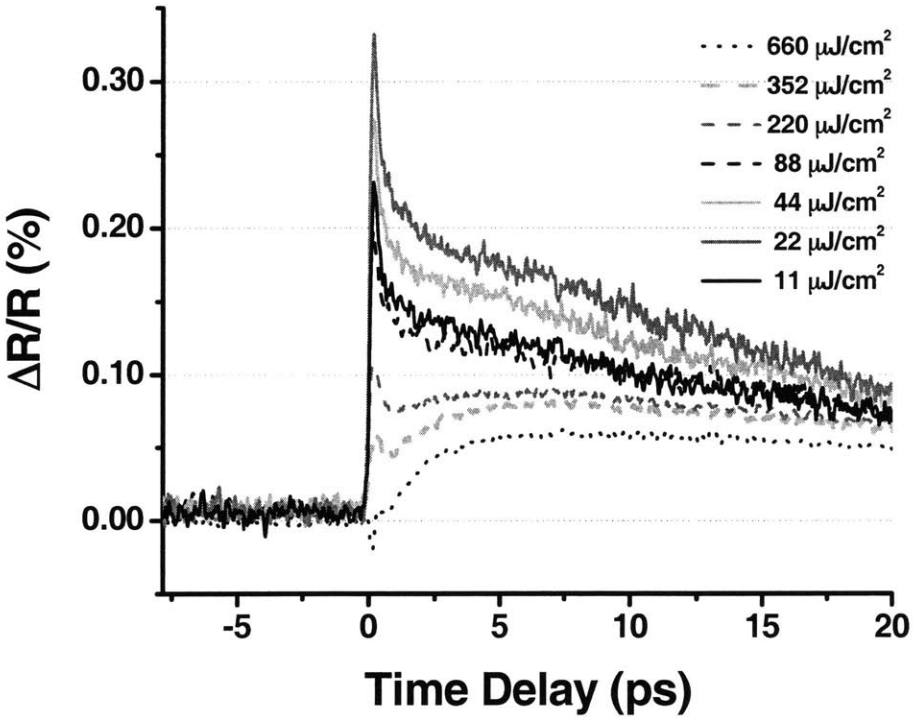

Figure 4.32 Pump-probe traces of the broadband saturable Bragg reflector at 1540 nm.

As mentioned earlier, an exact reflectivity figure cannot be determined from FTIR for these SBRs. We can only infer that the absolute SBR reflectivity is >99% from the successful use of the mirror in the low gain Cr^{4+}:YAG laser itself. Using the so-called Findlay-Clay analysis, we can indirectly determine a conservative estimate of the SBR loss. This technique relies on measuring the laser threshold powers for several resonators, which are exactly the same with the exception of a single optical element, such as an output coupler. The laser threshold condition can be written as

$$P_{th} = (L - \ln R)\frac{Ah\nu_p}{2\sigma\tau_f\eta_{pe}} \tag{4.15}$$

where P_{th} is the threshold power, R is the reflectivity of the output coupler, A is the cross-section of the laser rod, ω_p is the frequency of the pump light, σ is the stimulated emission cross-section, τ_f is the fluorescence lifetime, and η_{pe} is the overall pump efficiency. The variable L accounts for all the optical loss in the cavity, except for the output coupler. When

different resonators, as described above, are used, only R, L, and η_{pe} are changed; all others are either constant material properties or constant resonator properties. We can even argue that the pump efficiency η_{pe} remains constant as well, since the resonator dimensions should stay exactly the same and slightly different end mirrors (output coupler or SBR) would not distort the cavity mode significantly. In this context, we can rewrite Equation (4.15) as

$$P_{th} = c(L + T) \tag{4.16}$$

where T is the transmission of the output coupler and c is a constant. Here, we have used the relation

$$\ln R = R - 1 = -T \tag{4.17}$$

Using Equation (4.16), we can essentially determine the absolute loss of the SBR from the threshold power of three *L-L* curves. An *L-L* curve plots the output power of a laser as a function of the input power. From this, one can determine the laser threshold, which is the input power at which cw lasing is initiated. Two of the resonators (*1* and *2*) have an end mirror *HR* of known reflectivity in place of the SBR, and they have different output couplers *OC1* and *OC2*. Two of the resonators (*1* and *3*) have the same output coupler *OC1* and different end mirrors – the SBR and *HR*. For the first two resonators, the loss term L in Equation (4.16) is unchanged since the end mirror is the same and all other factors, such as the resonator dimensions, are held constant. From this, we can determine c.

$$P_{th,1} - P_{th,2} = c(L_1 - L_2) + c(T_1 - T_2) = c(T_1 - T_2) \tag{4.18}$$

$$c = \frac{P_{th,1} - P_{th,2}}{T_{OC1} - T_{OC2}} \tag{4.19}$$

Now, using c, we can use the threshold power of resonator *3* to determine the absolute loss of the SBR. Recall that resonator *1* and *3* use the same output coupler.

$$\frac{P_{th,3} - P_{th,1}}{c} = L_3 - L_1 = (L_c + L_{SBR}) - (L_c + L_{EM}) \tag{4.20}$$

where L_c accounts for the cavity losses, excluding the output coupler and end mirror, L_{EM} is the absolute loss of the end mirror, and L_{SBR} is the absolute loss of the saturable Bragg reflector. Therefore,

$$L_{SBR} = L_{EM} + \frac{P_{th,3} - P_{th,1}}{c} \tag{4.21}$$

In our experiment, we measured four *L-L* curves, with three different output couplers, shown in Figure 4.33. The analysis is essentially the same as above. When the SBR was inserted into the resonator, the laser modelocked. Therefore, the calculated value is the loss when the laser is modelocked. From the power thresholds of the *L-L* curves, we can quote a conservative estimate of the SBR loss to be 0.8%, at most.

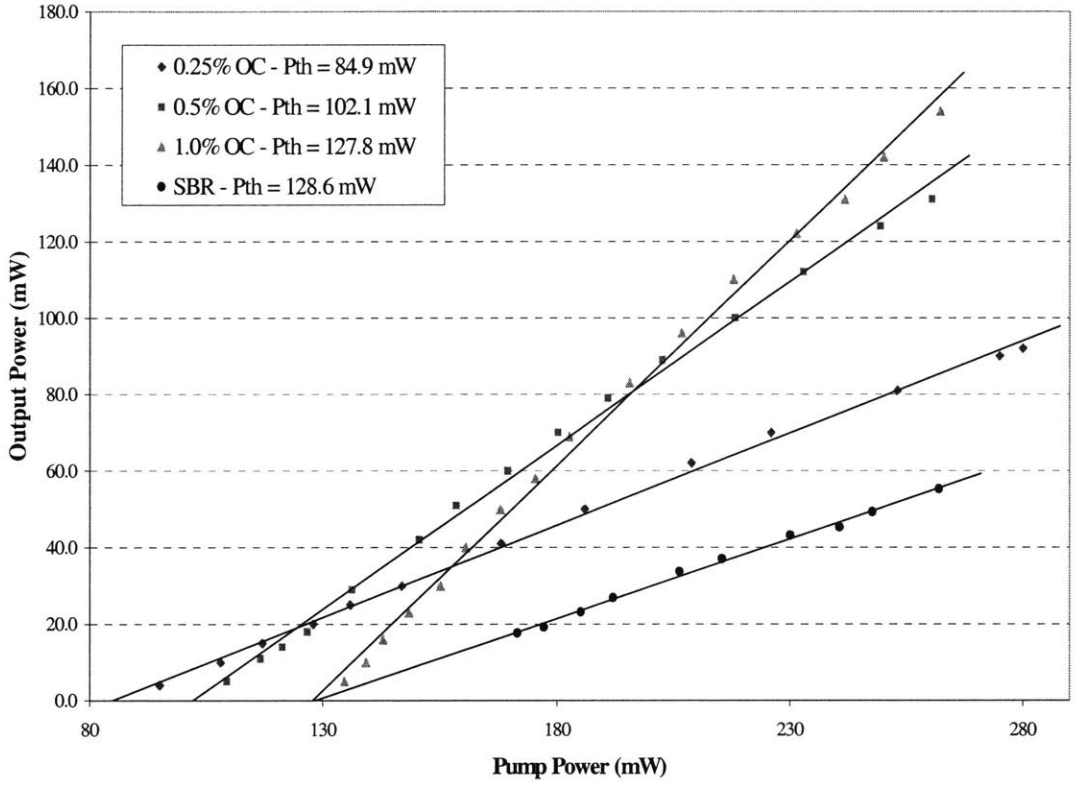

Figure 4.33 L-L curves for four similar Z-fold Cr^{4+}:YAG laser resonator configurations, used to determine the absolute loss of the saturable Bragg reflector.

4.2.2 Experimental Setup

A schematic of the self-starting Cr^{4+}:YAG laser resonator is shown in Figure 4.34. The resonator is the same as that described in Section 4.1 and shown in Figure 4.16, except for two changes. The flat DCM previously at *M3* is replaced by a curved 10 cm radius-of-curvature DCM, which focuses light onto the SBR at *M4*, where previously there was a quarter-wave-stack high reflector. Using *ABCD* matrices, a rough estimate of the spot size on the SBR – 50 μm – was determined. Again, the Brewster-Brewster-cut Cr^{4+}:YAG rod, supplied by A. V.

Shestakov of E.L.S company, has dimensions of 2 cm in length and 3 mm in diameter, and is pumped at 1064 nm by a Spectra-Physics 11 W Nd:YVO_4 laser. The pump beam is focused into the crystal through a 10 cm focal length lens. The laser crystal has a linear absorption of 1.5 cm^{-1} and is cooled to 13 °C during operation. Approximately 5 cm to both sides of the Cr^{4+}:YAG crystal are 10-cm-ROC DCMs, *M1* and *M2*, rotated 15.8 degrees from normal incidence to compensate for the astigmatism introduced by the Brewster-Brewster-cut laser crystal. The arm of the resonator containing the output coupler *OC* is 50 cm long, and the other arm is 70 cm long. The output coupler is the same as that used previously and its reflection properties were previously shown in Figure 4.17. The dispersion compensation of this laser has already been described. Finally, the resonator in its entirety is enclosed in plastic tubes and purged with dry nitrogen gas to remove water impurities.

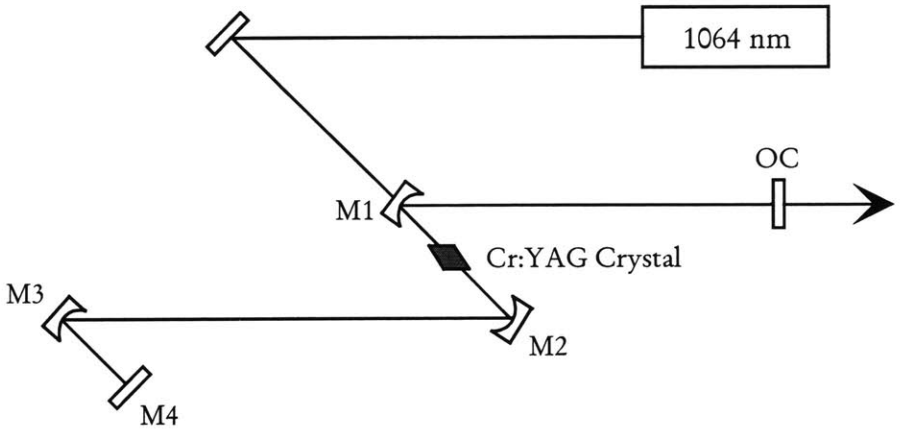

Figure 4.34 Schematic of the self-starting prismless Cr^{4+}:YAG laser resonator.

The laser is initially aligned in cw mode with a flat DCM in place of the SBR at position *M4*, and the output power is optimized. In this configuration, the cw output power was 600 mW for 9 W of absorbed pump. The DCM is then removed from *M4* and replaced with the SBR. The SBR must then be carefully positioned so that light is incident on the low-loss oxidized region of the mirror. Otherwise, lasing is not possible due to the high loss of the unoxidized regions. The usable mirror surface is only 200 μm on each side and the spot size on the SBR is roughly 50 μm. Since the SBR growth in not entirely homogeneous, the beam focus must be raster-scanned across the entire usable mirror surface to find a "sweet spot" for optimum modelocked operation. In order to align the resonator for KLM, the folding mirror separation distance between *M1* and *M2* and the laser crystal position between those folding mirrors must be adjusted simultaneously, as described before. However, regardless of

alignment, after finding the "sweet spot" on the SBR, the laser modelocked.

4.2.3 Experimental Results

The SBR was then used to self-start Kerr lens modelocking in the Cr^{4+}:YAG laser. Modelocked pulses as short as 35 fs were generated directly from the laser resonator. The average output power was roughly 300 mW for 9 W of absorbed pump. A sample pulse spectrum, measured with an optical spectrum analyzer, is shown in Figure 4.35. The spectrum peaks at 1500 nm and has a FWHM of 68 nm. Significant spectrum is observable from 1200 nm to >1700 nm, which is the long wavelength limit of our OSA.

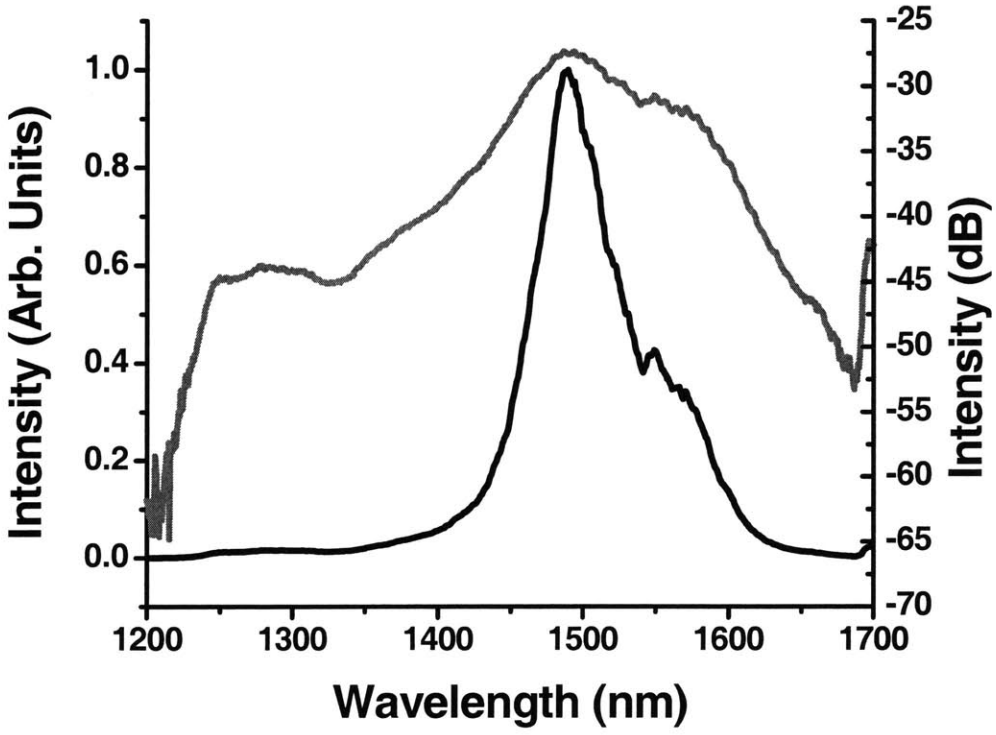

Figure 4.35 Modelocked pulse spectrum from the self-starting prismless Cr^{4+}:YAG laser.

The pulse duration was measured by interferometric autocorrelation. The layout of the autocorrelator was shown earlier in Figure 4.20. An autocorrelation trace is plotted in Figure 4.36. Assuming a sech-shaped temporal profile, the pulse width was estimated to be 32 fs. A Fourier transform of the optical spectrum, assuming a flat phase profile, yielded an unchirped

pulse duration of 35 fs. Since a sech-shaped pulse fit would underestimate the true pulse duration for non-sech-shaped pulses, we quote the 35 fs pulse width result.

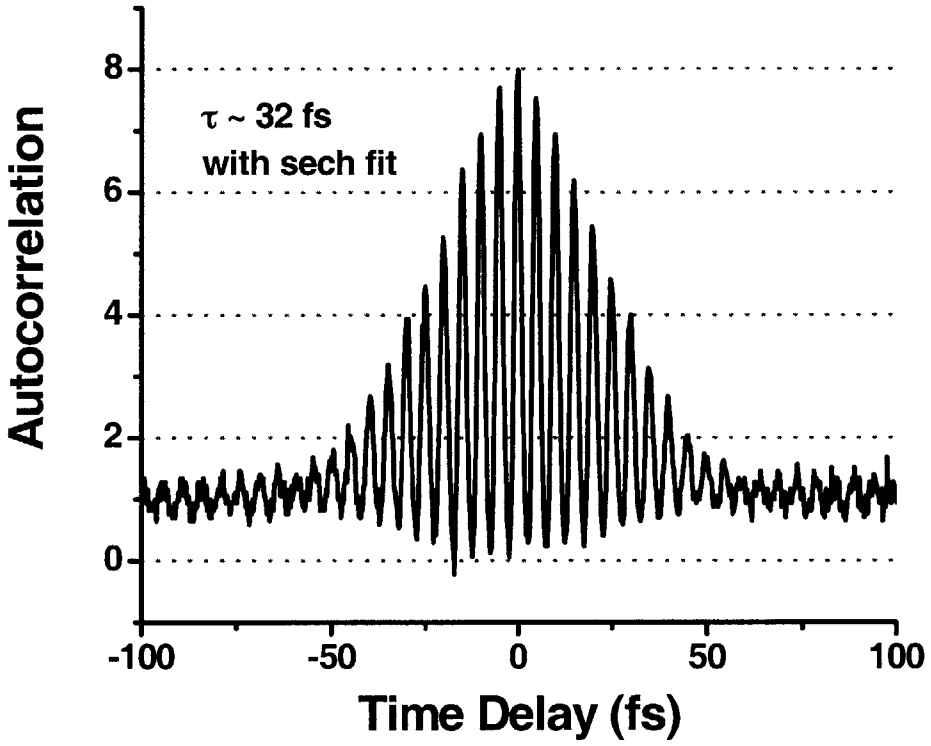

Figure 4.36 Interferometric autocorrelation of the self-starting Cr^{4+}:YAG laser.

Ideally, the self-starting Cr^{4+}:YAG laser should achieve or even beat the pulse duration (20 fs) generated by the laser described previously in Section 4.1. There is no fundamental reason why this cannot be reached, because the SBR should start KLM and then behave just as any normal high reflector, such as the one in Section 4.1. In fact, the SBR should better that mirror because the SBR also stabilizes modelocking by attenuating cw perturbations. We believe that two-photon absorption (TPA) in the SBR is limiting the pulse duration in this laser, when it is Kerr lens modelocked. TPA increases the loss in the absorber and consequently the reflectivity of the SBR, which in turn decreases KLM strength due to the lower-intensity light circulating in the resonator. In order to avoid TPA, we must decrease the fluence incident on the SBR. One way to do this experimentally is by increasing the spot size on the SBR. We replaced the 10-cm-ROC DCM at *M3* with a 20-cm-ROC DCM, and

attempted modelocking. However, the resulting spot size was larger than the dimensions of the oxidized region on the SBR (200 μm), and subsequently the pulse experienced too much loss to initiate KLM.

In addition to self-starting KLM in the Cr^{4+}:YAG laser, we were able to generate ~1 ps pulses, tunable from 1400 to 1525 nm, by inserting a birefringent filter into the resonator [73]. The pulse spectrum and tuning range are shown in Figure 4.37.

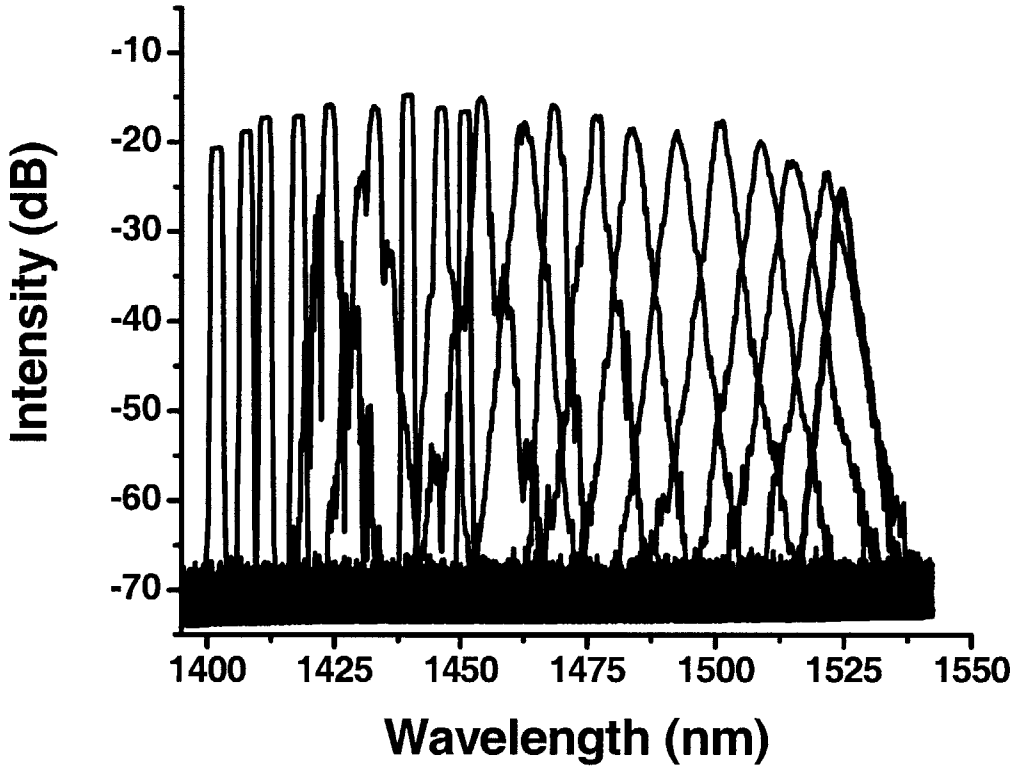

Figure 4.37 Spectra of the saturable absorber modelocked Cr^{4+}:YAG laser tuned from 1400 to 1525 nm with a birefringent tuning plate.

Chapter 5

CONCLUSION

5.1 SUMMARY

This thesis has reported on the design and construction of an ultrafast Cr^{4+}:YAG laser source in the near-infrared. Pulses as short as 20 fs have been generated directly from a prismless Cr^{4+}:YAG laser, using only double-chirped mirrors for dispersion compensation. The modelocked pulse spectrum peaked at 1450 nm and has a FWHM of 190 nm. Significant spectrum was observed extending from 1140 to >1700 nm. In addition, broadband saturable absorber mirrors were developed to self-start modelocking in the Cr^{4+}:YAG laser. These broadband saturable Bragg reflectors consisted of a 7-pair GaAs/Al_xO_y quarter-wave dielectric stack and an InGaAs/InP quantum well saturable absorber. The SBR had a high-reflectance bandwidth extending from 1300 to 1800 nm and a loss figure of roughly 8% when modelocked. Self-starting pulses of 35 fs duration were generated directly from the prismless laser. The corresponding pulse spectrum peaks at 1490 nm, with a FWHM bandwidth of 68 nm. By adding a birefringent filter to the resonator, we were able to produce picosecond self-starting pulses, tunable from 1400 to 1525 nm.

5.2 FUTURE WORK

5.2.1 Resonator Modifications

There are several modifications to the resonator to be attempted, so that shorter pulses can be produced. One of which is the addition of low-water-content prisms. While prismless lasers are convenient to align, they do not necessarily generate the shortest possible pulses. With the addition of intracavity prisms, fine tuning of the net dispersion in the resonator can be achieved. BaF_2 prisms have been determined to work well, together with double-chirped mirrors, in the Cr^{4+}:YAG laser resonator.

Currently, a 2 cm Cr^{4+}:YAG laser crystal is used in the resonator. However, a shorter crystal would be preferred. The reason for this is twofold – (1) a shorter crystal would mean less dispersion to compensate and would perhaps be a better match for the current double-chirped mirror design; and (2) a shorter crystal would require a smaller astigmatism compensation angle. By reflecting off the DCMs at oblique angles, disruptive oscillations are introduced to their dispersion profile. The oscillations need to be reduced in order to produce shorter pulses. A smaller astigmatism compensation angle would reduce these oscillations.

Alternatively, new double-chirped mirrors could be designed and fabricated. These would be tailored to work with a 2-cm-long Cr^{4+}:YAG laser crystal, in conjunction with the aforementioned BaF_2 prisms. The new mirror design would also need to take into account oblique angles of incidence, so that spurious anti-reflections are avoided and the dispersion profile is smooth and uniform. Furthermore, π-phase-shifted DCM pairs could be used to lower the GDD oscillation amplitude [74].

And finally, efficient broadband saturable absorber mirrors should continue to be investigated and developed. Currently, the self-starting Cr^{4+}:YAG laser is limited by two-photon absorption. Therefore, one solution would be to grow a larger-area saturable Bragg reflector. This would allow for a larger spot size on the mirror and subsequently realize the lower fluence needed to avoid TPA. Alternatively, a new design could be made altogether – the position of the quantum well absorbers could be moved to a node in the electric field standing wave pattern in the SBR structure, so as to increase the saturation fluence.

5.2.2 Pump-Probe Spectroscopy

The temporal resolution of pump-probe spectroscopy is ultimately set by the duration of the pump and probe pulses. In the near-infrared, optical parametric oscillators producing ~100 fs pulses are the most common light source for pump-probe experiments. With this time resolution, pump-probe spectroscopy can observe carrier-lattice interactions, but not carrier-carrier interactions, which are believed to occur on the 10 – 100 fs time scale. These interactions, however, would be observable using the 20 fs pulses from the Cr^{4+}:YAG laser source. Using the Cr^{4+}:YAG, we could investigate fast carrier-carrier interactions at 1.5 μm in many materials.

5.2.3 Phaselocking Two Lasers

The shortest pulses generated, to date, are 5 fs, from a Ti:sapphire laser. These pulses are shorter than 2 optical cycles at their center wavelength of 840 nm. The ultimate limit is a

single cycle pulse. Any shorter and Maxwell's equations would prevent a propagating electromagnetic wave. In order to achieve a single cycle, a pulse must have a tremendous amount of spectral bandwidth. At the moment, no such material exists that can provide such bandwidth. One method to circumvent this, however, would be to combine the gain spectra of two lasers through phaselocking. By matching the phase and repetition rate of two lasers, one could interferometrically combine the two pulse trains. It has been recently demonstrated that two Ti:sapphire lasers could be phaselocked in such a manner [75]. The resulting pulses were shorter than the pulses either laser generated independently. More recently, a Cr:forsterite laser and a Ti:sapphire were synchronized [76]. In both cases, however, the phaselocked laser system was unable to generate single-cycle pulses. A plot of the spectra from Cr^{4+}:YAG and Ti:sapphire lasers is shown in Figure 5.1. Together, these lasers span at least three octaves of spectrum in wavelength and have a Fourier transform pulse duration of 3.1 fs. Additional spectrum could be generated through continuum generation [77]. Therefore, once phaselocked, these lasers have the potential to generate single-cycle pulses. For this reason, multi-laser phaselocking is currently becoming a particularly exciting area of research.

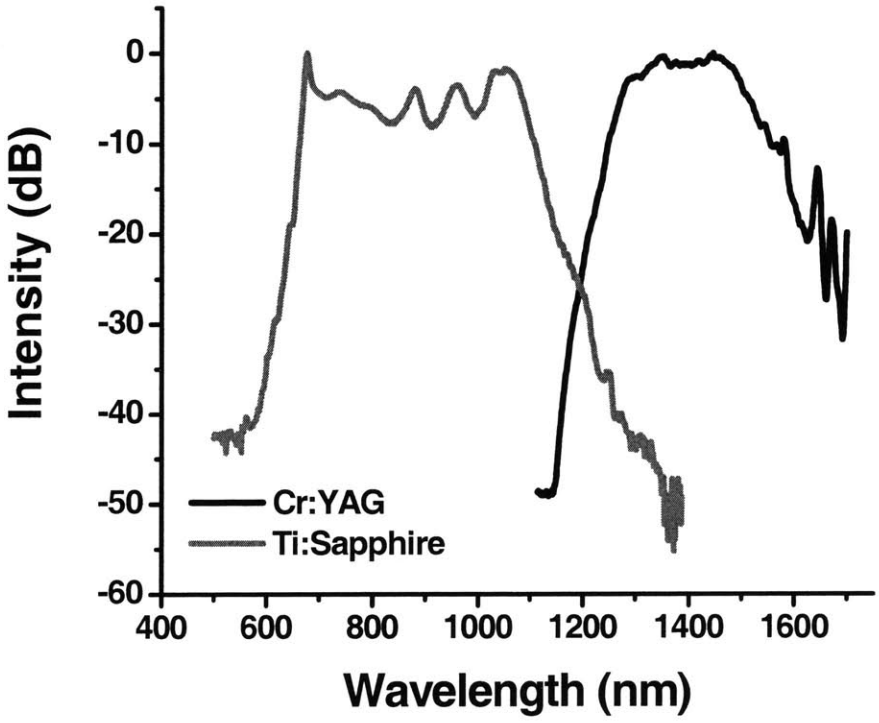

Figure 5.1 Spectra from the Cr^{4+}:YAG and Ti:Sapphire lasers. Together, the spectra span two octaves in wavelength.

References

1. T. H. Maiman, Nature **187**, 493 (1960).
2. R. Ell, U. Morgner, F. X. Kärtner, J. G. Fujimoto, E. P. Ippen, V. Scheuer, G. Angelow, T. Tschudi, M. J. Lederer, A. Boiko, and B. Luther-Davies, Optics Letters **26**, 373 (2001).
3. A. H. Zewail, Science **242**, 1645 (1988).
4. E. P. Ippen, Femtosecond Pulse Generation Notes (1999).
5. L. Boivin, M. C. Nuss, W. H. Knox and J. B. Stark, Electronics Letters **33**, 827 (1997).
6. P. M. W. French, Reports on Progress in Physics **58**, 169 (1995).
7. J. C. Walling, H. P. Benson, R. C. Morris, E. W. O'Dell and O. G. Peterson, Optics Letters **4**, 182 (1979).
8. M. L. Shand and S. T. Lai, IEEE Journal of Quantum Electronics **20**, 105 (1984).
9. S. A. Payne, L. L. Chase, H. W. Newkirk, L. K. Smith and W. F. Krupke, IEEE Journal of Quantum Electronics **24**, 2243 (1989).
10. S. A. Payne, L. L. Chase, L. K. Smith, W. L. Kway and H. W. Newkirk, IEEE Journal of Quantum Electronics **66**, 1051 (1989).
11. L. I. Krutova, N. A. Kulagin, V. A. Sandulenko and A. V. Sandulenko, Soviet Physics Solid State **31**, 1193 (1989).
12. G. M. Zverev and A. V. Shestakov, OSA Proceedings on Tunable Solid State Lasers **5**, 66 (1989).
13. W. Jia, B. Tissue, L. Lu, K. R. Hoffman and W. M. Yen, OSA Proceedings on Tunable Solid State Lasers **10**, 87 (1991).
14. S. Kuck, K. Petermann and G. Huber, OSA Proceedings on Tunable Solid State Lasers **10**, 92 (1991).
15. N. I. Borodin, A. G. Okhrimchuk and A. V. Shestakov, OSA Proceedings on Tunable Solid State Lasers **13**, 42 (1992).
16. D. J. Ripin, *A Few-Cycle Cr^{4+}:YAG Laser and Optical Studies of Photonic Crystals*, MIT Doctoral Thesis (2002).
17. A. G. Okhrimchuk and A. V. Shestakov, Optical Materials **3**, 1 (1994).

18. G. P. Agrawal, *Nonlinear Fiber Optics*, Academic Press (1995).

19. A. E. Siegman, *Lasers*, University Science Books (1986).

20. E. Hecht, *Optics*, Addison-Wesley (1998).

21. R. L. Fork, O. E. Martinez and J. P. Gordon, Optics Letters **9**, 150 (1984).

22. R. Szipocs, K. Ferencz, C. Spielmann, F. Krausz, Optics Letters **19**, 201 (1994).

23. J. C. Diels, J. J. Fontaine, I. C. McMichael and F. Simoni, Applied Optics **24**, 1270 (1985).

24. F. X. Kärtner, N. Matuschek, T. Schibli, U. Keller, H. A. Haus, C. Heine, R. Morf, V. Scheuer, M. Tilsch, T. Tschudi, Optics Letters **22**, 831 (1997).

25. N. Matuschek, F. X. Kärtner, U. Keller, IEEE Journal of Selected Topics in Quantum Electronics **4**, 197 (1998).

26. F. Hache, T. J. Driscoll, M. Cavallari and G. M. Gale, Applied Optics **35**, 3230 (1996).

27. R. H. Picard and P. Schweitzer, Physics Letters **29A**, 415 (1969).

28. J. C. Diels and W. Rudolph, *Ultrashort Laser Pulse Phenomena*, Academic Press (1996).

29. D.T. Reid, M. Pidgett, C. McGowan, W. Sleat and W. Sibbett, Optics Letters **22**, 233 (1997).

30. J. K. Ranka, A. L. Gaeta, A. Baltuska, M. S. Pshenichnikov and D. A. Wiersma, Optics Letters **22**, 1344 (1997).

31. L. P. Barry, P. G. Bollond, J. M. Dudley, J. D. Harvey and R. Leonhardt, Electronics Letters **32**, 1922 (1996).

32. T. Norris, Ultrafast Optics Notes (2000).

33. A. Yariv, Journal of Applied Physics **36**, 388 (1964).

34. E. P. Ippen, Applied Physics B **58**, 159 (1994).

35. H. A. Haus, IEEE Journal of Quantum Electronics **11**, 736 (1975).

36. H. Haus, IEEE Journal of Quantum Electronics **46**, 3049 (1975).

37. H. Mocker and R. Collins, Applied Physics Letters **7**, 270 (1965).

38. A. DeMaria, D. Stetser, and H. Heynau, Applied Physics Letters **8**, 174 (1966).

39. E. P. Ippen, C. V. Shank, and A. Dienes, Applied Physics Letters **21**, 348 (1972).

40. O. E. Martinez, R. L. Fork, and J. P. Gordon, Journal of Optical Society of America **B** 2, 753 (1985).

41. H. A. Haus, J. G. Fujimoto, and E. P. Ippen, Journal of Optical Society of America **B** 8, 2068 (1991).

42. F. X. Kärtner and U. Keller, Optics Letters **16**, 1674 (1991).

43. S. M. J. Kelly, Electronics Letters **28**, 806 (1992).

44. Y. Chen, F. X. Kärtner, U. Morgner, S. H. Cho, H. A. Haus, E. P. Ippen, and J. G. Fujimoto, Journal of Optical Society of America B **16**, 1999-2004 (1999).

45. I. D. Jung, F. X. Kärtner, N. Matuschek, D. H. Sutter, F. Morier-Genoud, G. Zhang, U. Keller, V. Scheuer, M. Tilsch and T. Tschudi, Applied Physics B **65**, 137 (1997).

46. M. N. Islam, E. R. Sunderman, C. E. Soccolich, I. B. Joseph, N. Sauer, T. Y. Chang, and B. I. Miller, IEEE Journal of Quantum Electronics **25**, 2454 (1989).

47. J. T. Gopinath, *The Effect of Proton Bombardment on Semiconductor Saturable Absorber Structures*, MIT SM Thesis (2000).

48. J. A. Kong, *Electromagnetic Wave Theory*, EMW Publishing (2000).

49. E. Lariontsev and V. Serkin, Soviet Journal of Quantum Electronics **5**, 796 (1975).

50. D. E. Spence, P. N. Kean, and W. Sibbett, Optics Letters **16**, 42 (1991).

51. Salin, J. Squier and M. Piche, Optics Letters **16**, 1674 (1991).

52. A. Owyoung, R. W. Hellwarth, and N. George, Physical Review **B**5, 628 (1972).

53. Y. P. Tong, P. M. W. French, J. R. Taylor and J. G. Fujimoto, Optics Communications **136**, 235 (1997).

54. D. J. Ripin, C. Chudoba, J. T. Gopinath, J. G. Fujimoto, E. P. Ippen, U. Morgner, F. X. Kärtner, V. Scheuer, G. Angelow, and T. Tschudi, Optics Letters **27**, 61 (2002).

55. K. Naganuma, K. Mogi and H. Yamada, Optics Letters **15**, 393 (1990).

56. H. A. Haus, *Waves and Fields in Optoelectronics*, Prentice-Hall (1984).

57. W. Kogelnik, E. P. Ippen, A. Dienes and C. V. Shank, IEEE Journal of Quantum Electronics **8**, 373 (1972).

58. P. J. Conlon, Y. P. Tong, P. M. W. French, J. R. Taylor and A. V. Shestakov, Optics Letters **19**, 1468 (1994).

59. *OPAL User's Manual*, Spectra-Physics Lasers (1996).

60. A. Penzkofer, M. Wittmann, M. Lorenz, E. Siegert and S. Macnamara, Optics and Quantum Electronics **28**, 423 (1996).

61. G. Cerullo, S. de Silvestri and V. Magni, Optics Letters **19**, 1040 (1994).

62. Y. Ishida, K. Naganuma and H. Kamada, Optics Review **6**, 37 (1999).

63. A. Baltuska, A. Pugzlys, M. Pshenichnikov, D. Wiersma, B. Hoenders and H. Ferwerda, Ultrafast Optics Meeting at Ascona, Sweden (1999).

64. B. C. Collings, J. B. Stark, S. Tsuda, W. H. Knox, J. E. Cunningham, W. Y. Jan, R.

Pathak and K. Bergman, Optics Letters **21**, 1171 (1996).

65. M. J. Hayduk, S. T. Johns, M. F. Krol, C. R. Pollock and R. P. Leavitt, Optics Communications **137**, 55 (1997).

66. S. Spälter, M. Bohm, M. Burk, B. Mikulla, R. Fluck, I. D. Jung, G. Zhang, U. Keller, A. Sizmann and G. Leuchs, Applied Physics B **65**, 335 (1997).

67. Z. Zhang, T. Nakagawa, K. Torizuka, T. Sugaya and K. Kobayashi, Optics Letters **24**, 1768 (1999).

68. Z. Zhang, T. Nakagawa, K. Torizuka, T. Sugaya and K. Kobayashi, Applied Physics B **70**, S56 (2000).

69. K. D. Choquette, K. M. Geib, C. I. H. Ashby, R. D. Twesten, O. Blum, H. Q. Hou, D. M. Follstaedt, B. E. Hammons, D. Mathes and R. Hull, IEEE Journal of Selected Topics in Quantum Electronics **3**, 916 (1997).

70. M. H. MacDougal, P. D. Dapkus, V. Pudikov, H. Zhao, G. M. Yang, IEEE Photonics Technology Letters **7**, 229 (1995).

71. J. H. Kim, D. H. Lim, K. S. Kim, G. M. Yang, K. Y. Lim, H. J. Lee, Applied Physics Letters **69**, 3357 (1996).

72. A. Erchak, *Enhanced Performance of Optical Sources in III-V Materials Using Photonic Crystals*, MIT Doctoral Thesis (2002).

73. K. Naganuma, G. Lenz and E. P. Ippen, IEEE Journal of Quantum Electronics **28**, 2142 (1992).

74. F. X. Kärtner, U. Morgner, R. Ell, T. Schibli, J. G. Fujimoto, E. P. Ippen, V. Scheuer, G. Angelow and T. Tschudi, Journal of Optical Society of America B **18**, 882 (2001).

75. R. K. Shelton, L. S. Ma, H. C. Kapteyn, M. M. Murnane and J. Ye, Science **293**, 1286 (2001).

76. Z. Wei, Y. Kobayashi, Z. Zhang and K. Torizuka, Optics Letters **26**, 1806 (2001).

77. J. K. Ranka, R. S. Windeler and A. J. Stentz, Optics Letters **25**, 25 (2000).